**FACULTY
OF MATHEMATICS
AND PHYSICS**
Charles University

DOCTORAL THESIS

Ján Mašek

Broadband radiation scheme fully interacting with clouds

Atmospheric Physics

Supervisor of the doctoral thesis: Radmila Brožková, Ph.D.

Study programme: Physics

Study branch: Meteorology and Climatology

Prague 2017

I declare that I carried out this doctoral thesis independently, and only with the cited sources, literature and other professional sources.

I understand that my work relates to the rights and obligations under the Act No. 121/2000 Sb., the Copyright Act, as amended, in particular the fact that the Charles University has the right to conclude a license agreement on the use of this work as a school work pursuant to Section 60 subsection 1 of the Copyright Act.

In Prague, 9th September 2017.   Ján Mašek

Title: Broadband radiation scheme fully interacting with clouds

Author: Ján Mašek

Department: Atmospheric Physics

Supervisor: Radmila Brožková, Ph.D., Department of Meteorology and Climatology, Czech Hydrometeorological Institute

Abstract: The parameterization of radiative transfer is a part of numerical weather prediction and general circulation models that is both essential and computationally very expensive, and is therefore subject to never-ending compromises between accuracy and computational cost. The present thesis offers an improvement to the existing broadband radiation scheme by revising its critical components – gaseous transmissions, cloud optical properties, and calculation of internal longwave exchanges. The accuracy of the full-spectrum broadband approach is thus raised to the level required for the short range numerical weather forecast. The intermittent update of broadband gaseous transmissions is introduced as a new component, reducing computational cost while preserving the full cloud-radiation interaction. The scalability of longwave computations is ensured by adopting the net exchanged rate decomposition with bracketing, improved by an intermittently applied self-learning algorithm determining the interpolation weights. It has been demonstrated that under conditions of operational weather forecasting, this developed scheme is fully competitive with the mainstream approach, due to the improved error balance between the stand-alone radiation scheme and the intermittency strategy.

Keywords: atmospheric radiative transfer, cost versus accuracy, broadband approach, intermittent update, error balance

Contents

Introduction

It is unquestionable that radiative forcing is one of the key factors determining the Earth's weather and climate. As noted e.g. by Fouquart et al. [1991], a change in radiative forcing of only few $W\,m^{-2}$ can affect the climate substantially. This imposes strict demands on the accuracy of the radiative transfer schemes employed in GCMs (General Circulation Models), without which the reliability of climate simulations would be compromised. However, the computational cost of highly accurate line-by-line radiation codes restricts their use to delivering reliable reference solutions for a limited set of benchmark cases. Oreopoulos et al. [2012] explain that such results are used as a basis for the development of the much faster codes used to perform efficient radiative transfer in GCMs. The question of computational cost is especially critical in NWP (Numerical Weather Prediction), where real computational time must not amount to more than a few per cent of the forecast length. This constitutes a severe limitation on the complexity of the schemes used, such that a proper balance between cost and accuracy must be sought.

The short range NWP, characterized by a forecast length of up to three days as well as high spatial and temporal resolutions, shifts its primary focus within radiative transfer from the unbiased radiation budget to the full interaction of radiation with clouds. The latter issue is crucial for the internal consistency of NWP model feedbacks, and is necessary for a realistic description of the local weather phenomena and of the diurnal cycle. Unlike in climate modelling, the eventual bias in the radiation budget is much less harmful to short range forecasting, where each forecast starts from an actual analysis and there is not enough time for a drift to develop.

The main goal of the work described in this thesis was to improve the accuracy of the radiative transfer scheme ACRANEB (Actif Calcul de RAyonnement et NÉBulosité), the first version of which was developed in the 1990s in Météo-France as part of the short range NWP model ALADIN (Aire Limitée Adaptation dynamique Développement InterNational). The efficiency of the ACRANEB scheme is achieved via a broadband approach with single shortwave and single longwave spectral intervals, and the relatively simple parameterization of gaseous transmissions. The scalability of the longwave calculations is ensured by the use of NER (Net Exchanged Rate) decomposition, further improved by the so-called bracketing technique with statistically fitted interpolation weights. The low computational cost of the ACRANEB scheme allows it to be called at every model grid-point and time-step, which is a highly desirable feature in high resolution NWP.

The strategy decided upon was to preserve the fundamental ACRANEB choices that ensure efficiency (broadband approach, delta-two-stream approximation, adding method, NER decomposition), and to redevelop the weakest components (gaseous transmissions, cloud optical properties, bracketing technique). The intermittent update of new gaseous transmissions was seen as a way to reduce their high anticipated cost. The update of cloud optical properties at every model grid-point and time-step together with the subsequent solving of the radiative transfer equation was retained as an absolute necessity. Work along these sketched lines re-

sulted in a substantially improved radiative transfer scheme dubbed ACRANEB2, which became a key component of the so-called ALARO-1 (ALadin to AROme) configuration, used operationally within the model ALADIN/CHMI.

The present thesis describes the author's contribution to the ACRANEB2 developments in which he took part during the years 2011–2016. It does not provide a comprehensive overview of the ACRANEB2 scheme, which can be found in Mašek et al. [2016] and Geleyn et al. [2017], with regard to its shortwave and longwave aspects respectively. These two articles (attached to the printed version of this thesis) describe the achievements made since the early 2000s by a group of people under the leadership of Jean-François Geleyn, who invented the ACRANEB and ACRANEB2 concepts and systematically pushed forward their NWP implementation. The author contributed to this endeavour with the following ACRANEB2 developments:

- creating tools for handling various optical datasets

- constructing fitting references for broadband gaseous transmissions, Rayleigh scattering, and cloud optical properties

- developing a robust minimization procedure, used for all sorts of non-linear fits

- constructing a 1D narrowband radiative transfer model, used as a reference for evaluating the accuracy of the broadband approach and bracketing technique

- proposing a new functional shape for broadband gaseous transmissions, respecting their asymptotic behaviour resulting from secondary saturation

- addressing the double temperature dependence of longwave gaseous transmissions and accommodating it in NER decomposition

- parameterizing the non-random spectral overlap between gaseous pairs in absorptivity space

- parameterizing the broadband optical saturation of the water vapour e-type continuum and its spectral overlap with line absorption

- parameterizing the optical saturation of broadband Rayleigh scattering as an analogue to the secondary saturation of gaseous absorption

- proposing a new functional shape for fits providing unsaturated broadband cloud optical properties; refitting against modern datasets

- parameterizing the optical saturation of shortwave cloud absorption, taking into account its non-local nature and vertical variation across the cloud

- parameterizing the non-random spectral overlap between shortwave gaseous and cloud absorptions

- contributing to the design of shortwave and longwave intermittency strategies

- developing an improved bracketing technique based on self-calibrated interpolation weights

- implementing a generalized cloud overlap

- improving the diagnostics of direct solar flux and sunshine duration

- creating the ACRANEB2 code and its stand-alone single column version

- performing extensive ACRANEB2 validation ranging from 1D idealized cases to 3D real cases

The focus of the thesis is on four components crucial to ACRANEB2 success: broadband gaseous transmissions, shortwave cloud optical saturation, the bracketing technique, and selective intermittency. The structure of the thesis is as follows:

Chapter 1 gives a general overview of the radiative transfer problem in the NWP environment. It starts from the radiative transfer equation and introduces a set of approximations leading to the final delta-two-stream and adding system. Then it describes the two main approaches to the computationally challenging problem of spectral integration, comparing their pros and cons. Finally it outlines the embedding of the radiative transfer scheme in the NWP model.

Chapter 2 constitutes the core of the work, presenting the key improvements leading to the ACRANEB2 scheme. These include the new parameterizations of the broadband gaseous transmissions and of the shortwave cloud optical saturation that are necessary for obtaining sufficient accuracy. These parameterizations are complemented by the revised bracketing technique, increasing the accuracy of longwave atmospheric exchanges; and by selective intermittency, making the cost of the new gaseous transmissions affordable.

The Conclusion summarizes the main achievements that have led to an efficient yet accurate broadband radiation scheme. It also lists the scheme's known limitations and future challenges.

1. Radiative transfer in the NWP context

1.1 Radiative transfer equation

Radiative transfer in any medium is *described* by the microscopic Maxwell's equations. Their direct solution is however not tractable for the systems containing high number of elementary electric charges, since every charge responds to electromagnetic fields generated by all other charges. For this reason, the problem has to be simplified before it can be *solved* mathematically. In an important case of the randomly placed and well separated particles, this can be done in several steps described at the very beginning of Mishchenko et al. [2002].

For an isolated particle, such as air molecule, aerosol or cloud droplet, *single scattering properties* (absorption and scattering cross sections, the scattering phase function) can be determined using macroscopic Maxwell's theory. It expresses bound charges and bound currents via polarization and magnetization fields, which are in turn given by constitutive relations. In the simplest case of a spherical particle with constant refractive index, analytical answer is provided by the Lorenz-Mie theory, covering the full range of size parameters including the geometrical optics and Rayleigh scattering limits. For more complicated particle shapes (e.g. ice crystals or their aggregates), single scattering properties can be calculated numerically.

The next step assumes a volume element containing the small number of well separated particles with known single scattering properties. When the volume element is exposed to incident electromagnetic wave, each particle responds to the total electromagnetic field composed of the incident wave and the secondary waves generated by all other particles. Wide particle separation combined with their small number ensures validity of the *single scattering approximation*, where the action of secondary waves on particles can be neglected. This is because each particle is in the far-field zones of all other particles, so that secondary waves reaching the particle are much weaker than the incident wave. So is their superposition, since the number of particles in the volume element is small. Resulting scattered wave is thus given by the superposition of secondary waves generated by particles *individually* responding to the incident wave.

Additional simplification applies when the particles in the volume element are randomly positioned and oriented. In a generic situation it leads to the *incoherent scattering*, when the intensity of scattered wave (represented by time averaged Poynting vector) is a simple sum of the intensities of secondary waves generated by the individual particles, regardless of their phase differences.

Single scattering approximation does not hold in the atmosphere, where the number of particles is huge. Even if the particles remain well separated and randomly placed, another step must be taken. It explicitly accounts for the fact that the particles are now exposed to the total electromagnetic field significantly contributed by the *multiple scattering*, thus very different from the incident wave.[1]

---

[1]Please note that the scattered radiation exists also in a purely absorbing case, attenuating the incident wave behind particle.
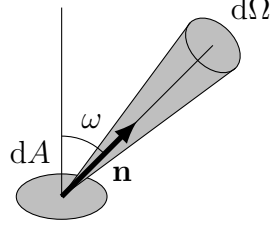
Figure 1.1: Explanation of spectral radiance $I_\nu(\mathbf{n})$: Radiant energy $\mathrm{d}E$ passing through the surface with area $\mathrm{d}A$ into the solid angle $\mathrm{d}\Omega$ oriented in the direction $\mathbf{n}$, cumulated through the spectral interval $[\nu, \nu + \mathrm{d}\nu]$ during the time $\mathrm{d}t$, is given as $\mathrm{d}E = I_\nu(\mathbf{n}) \cos\omega\, \mathrm{d}A\, \mathrm{d}\Omega\, \mathrm{d}\nu\, \mathrm{d}t$. Unit vector $\mathbf{n}$ is at angle ω to normal of the surface $\mathrm{d}A$, so that quantity $\cos\omega\, \mathrm{d}A$ is the area projected to direction $\mathbf{n}$.

Basic quantity of interest becomes spectral radiance I_ν, explained on figure 1.1. Its spatial and directional distributions are determined by the *radiative transfer equation* with appropriate boundary conditions. In the simplest case not considering polarization, the radiative transfer equation takes the shape:

$$\mathbf{n} \cdot \boldsymbol{\nabla} I_\nu(\mathbf{n}, \mathbf{r}) = \overbrace{-k_\nu^{\mathrm{abs}}(\mathbf{r})\rho(\mathbf{r})I_\nu(\mathbf{n}, \mathbf{r})}^{\text{absorption}} + \overbrace{k_\nu^{\mathrm{abs}}(\mathbf{r})\rho(\mathbf{r})B_\nu(T(\mathbf{r}))}^{\text{emission}}$$
$$\underbrace{+ k_\nu^{\mathrm{scat}}(\mathbf{r})\rho(\mathbf{r})\left[-I_\nu(\mathbf{n}, \mathbf{r}) + \frac{1}{4\pi}\oint_{4\pi} P_\nu(\mathbf{n}\cdot\mathbf{n}', \mathbf{r})I_\nu(\mathbf{n}', \mathbf{r})\,\mathrm{d}\Omega'\right]}_{\text{scattering}} \quad (1.1)$$

$$\frac{1}{4\pi}\oint_{4\pi} P_\nu(\mathbf{n}\cdot\mathbf{n}', \mathbf{r})\,\mathrm{d}\Omega' = \frac{1}{2}\int_{-1}^{1} P_\nu(\mu, \mathbf{r})\,\mathrm{d}\mu = 1 \qquad \mu \equiv \mathbf{n}\cdot\mathbf{n}' = \cos\Theta \quad (1.2)$$

The left hand side of equation (1.1) is the derivative of spectral radiance $I_\nu(\mathbf{n})$ in direction $\mathbf{n}$, evaluated at location $\mathbf{r}$ (see figure 1.2). It is contributed by three processes represented by the corresponding terms on the right hand side – absorption, emission and scattering. Symbols k_ν^{abs} and k_ν^{scat} denote the mass absorption and mass scattering coefficients of the medium, while ρ and T are its density and thermodynamic temperature. $B_\nu(T)$ is the blackbody radiance given by the Planck's law, P_ν is the scattering phase function respecting normalization (1.2), and $\mathrm{d}\Omega'$ is the infinitesimal solid angle in direction $\mathbf{n}'$. The absorption term decreases radiance along optical path, while the emission term increases it. The scattering term can have either sign since it consists of two counter-acting contributions – radiance $I_\nu(\mathbf{n})$ is decreased by scattering from direction $\mathbf{n}$ into other directions (first term in the square bracket), while it is increased by scattering from all directions into direction $\mathbf{n}$ (second term in the square bracket).

There are still several implicit assumptions behind the radiative transfer equation 1.1. First of all, it is supposed that emission coefficient k_ν^{emis} equals to absorption coefficient k_ν^{abs}, which is the consequence of Kirchhoff's law, valid in the *local thermodynamic equilibrium*. It restricts applicability of the radiative transfer equation to the troposphere and stratosphere, since the local thermodynamic equilibrium breaks down in the mesosphere around 60–70 km altitude. Here the inelastic collisions between air molecules become not frequent enough to dissipate
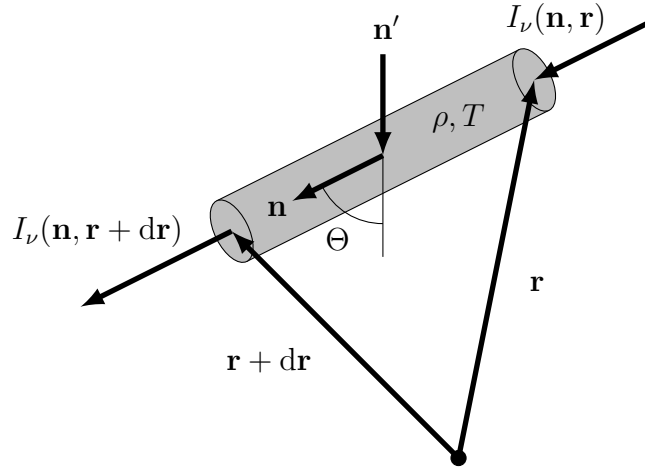
Figure 1.2: Geometry applied in a derivation of the radiative transfer equation. Change of the radiance $I_\nu(\mathbf{n}, \mathbf{r})$ is evaluated along an infinitesimal cylinder of height $|d\mathbf{r}|$, oriented in the direction of unit vector $\mathbf{n} = d\mathbf{r}/|d\mathbf{r}|$. The cylinder contains a radiatively active substance with the density ρ and temperature T. It can be illuminated from any direction $\mathbf{n}'$.

radiant energy absorbed by a molecule, so that it can be reemitted without being related to the kinetic temperature of the surrounding gas. Second, it is assumed that the radiation field adjusts to the forcings *immediately*. This is justified since the light-crossing time of the atmosphere is less than a millisecond, while the forcings evolve on the time scales of minutes or longer. Third, no interaction between different frequencies implies *elastic* scattering, excluding meteorologically insignificant phenomena such as Raman scattering or fluorescence. These can, however, be important in remote sensing employing lidars. Fourth, atmospheric refraction is neglected. In reality, it makes our day few minutes longer. Fifth, dependence of the scattering phase function on the cosine of scattering angle $\mathbf{n} \cdot \mathbf{n}'$ instead of separate incident and scattered directions $(\mathbf{n}, \mathbf{n}')$ means that any non-spherical particles must be *randomly oriented*. It excludes an impressive optical phenomenon of sun pillars, which is however too rare to be meteorologically significant. Random orientation of the air molecules results from their thermal motion, while for the small aerosol and cloud particles dispersed in the air it is ensured by turbulence. Only in the situations with very weak turbulence, larger ice particles of suitable shape can align due to the action of aerodynamic forces, associated with their non-negligible fall speed.

Radiative transfer equation (1.1) is a linear integro-differential equation for the spectral radiance $I_\nu(\mathbf{n}, \mathbf{r})$. In order to determine its solution uniquely, proper *boundary conditions* must be specified. A common way is to prescribe incoming radiance on open boundaries and to specify reflection(-emission) condition on material boundaries. In the physically realistic situations, such formulation leads to a well-posed problem. Perfectly reflecting boundary enclosing a non-absorbing cavity would allow for the existence of infinitely many solutions, but such highly idealized situation never occurs in practice.

Despite all underlying simplifications, radiative transfer equation (1.1) is adequate for evaluating the radiative fluxes and related energy budget in the tropo-

sphere and stratosphere. It is therefore fully sufficient in the short range NWP models, whose tops are not too far in the mesosphere. For example, current operational model ALADIN/CHMI has the highest level at 1.1 hPa, corresponding to altitude around 48 km, which is still in the stratosphere. Unfortunately, detailed numerical solution of equation (1.1) is beyond the reach of NWP. Additional simplifications must be done in order to cut the computational cost of spatial, angular and spectral integrations to the acceptable level.

1.2 Spatial and angular integrations

Spatial and angular integrations of equation (1.1) are closely interconnected. In the contemporary NWP models, they involve almost exclusively so-called *plane-parallel* and *delta-two-stream approximations*, combined with *adding method*. Altogether, they reduce the problem to the solution of independent linear algebraic systems for fluxes.

a) Plane-parallel approximation

First step, significantly reducing the computational cost and enabling parallel computing, replaces the 3D spatial problem with the set of *independent* 1D problems, where the lateral radiative exchanges between neighbouring model columns are neglected. Atmosphere in each model column is assumed plane-parallel and horizontally homogeneous, extending to infinity so that lateral boundaries are suppressed. As a consequence, all spatial fields in the given column depend on the vertical coordinate only. This is the plane-parallel approximation, enabling to collapse radiative transfer equation (1.1) into the shape involving only azimuthally integrated radiance $I_\nu(\mu)$ and azimuthally averaged phase function $P_\nu(\mu, \mu')$:

$$\mu \frac{dI_\nu}{d\delta_\nu}(\mu) = -I_\nu(\mu) + 2\pi(1 - \varpi_\nu)B_\nu(T) + \frac{\varpi_\nu}{2} \int_{-1}^{1} P_\nu(\mu, \mu')I_\nu(\mu') \, d\mu' \qquad (1.3)$$

$$\delta_\nu(z) \equiv \int_z^{\infty} [k_\nu^{abs}(z') + k_\nu^{scat}(z')]\rho(z') \, dz' \qquad (1.4)$$

$$\varpi_\nu \equiv \frac{k_\nu^{scat}}{k_\nu^{abs} + k_\nu^{scat}} \qquad (1.5)$$

$$I_\nu(\mu) \equiv \int_0^{2\pi} I_\nu(\mu, \phi) \, d\phi \qquad (1.6)$$

$$P_\nu(\mu, \mu') \equiv \frac{1}{2\pi} \int_0^{2\pi} P_\nu(\cos\Theta) \, d\phi \qquad (1.7)$$

$$\cos\Theta \equiv \mathbf{n} \cdot \mathbf{n}' = \sqrt{(1 - \mu^2)(1 - \mu'^2)} \cos(\phi - \phi') + \mu\mu' \qquad (1.8)$$

Equation (1.3) is formulated using the optical depth (1.4) in place of vertical coordinate. It is measured from the TOA (Top Of the Atmosphere), formally put at $z = \infty$, down to current level. Vertical dependence of radiance I_ν, phase function P_ν, single scattering albedo ϖ_ν and temperature T is not explicitly indicated. Symbols μ and ϕ denote cosine of zenith angle and azimuth. Equation (1.3) uses convention where downward propagating rays have positive μ, as shown on
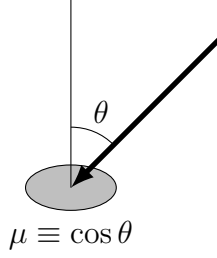
$$\mu \equiv \cos\theta$$

Figure 1.3: Convention for zenith angle θ of the incident ray and its cosine μ. Downward propagating rays have $\mu > 0$, while upward propagating rays have $\mu < 0$.

figure 1.3. Independence of azimuthally averaged phase function $P_\nu(\mu, \mu')$ on angle ϕ' follows from periodicity of the argument $\cos\Theta$ in difference $\phi - \phi'$.

In the solar spectrum, it is convenient to split the radiance into *bounded* diffuse component I_ν^{diff} and *singular* direct component I_ν^{dir}, representing perfectly collimated unscattered solar radiation:

$$I_\nu(\mathbf{n}) \equiv I_\nu^{\mathrm{diff}}(\mathbf{n}) + I_\nu^{\mathrm{dir}}(\mathbf{n}) \equiv I_\nu^{\mathrm{diff}}(\mathbf{n}) + F_\nu^{\mathrm{dir}} \cdot \delta(\mathbf{n}, \mathbf{n}_0) \tag{1.9}$$

Symbol $\delta(\mathbf{n}, \mathbf{n}_0)$ denotes the Dirac delta function on the sphere[2], and $\mathbf{n}_0$ is the unit vector along unscattered beam having DNI (Direct Normal Irradiance) F_ν^{dir}. Rederiving the plane-parallel approximation with decomposition (1.9) yields equations for azimuthally integrated diffuse radiance $I_\nu^{\mathrm{diff}}(\mu)$ and for direct normal irradiance F_ν^{dir}:

$$\mu \frac{\mathrm{d}I_\nu^{\mathrm{diff}}}{\mathrm{d}\delta_\nu}(\mu) = -I_\nu^{\mathrm{diff}}(\mu) + 2\pi(1 - \varpi_\nu)B_\nu(T)$$

$$+ \frac{\varpi_\nu}{2}\int_{-1}^{1} P_\nu(\mu, \mu')I_\nu^{\mathrm{diff}}(\mu')\,\mathrm{d}\mu' + \frac{\varpi_\nu}{2}F_\nu^{\mathrm{dir}}P_\nu(\mu, \mu_0) \tag{1.10}$$

$$\mu_0 \frac{\mathrm{d}F_\nu^{\mathrm{dir}}}{\mathrm{d}\delta_\nu} = -F_\nu^{\mathrm{dir}} \tag{1.11}$$

Splitting single radiative transfer equation into separate equations (1.10) and (1.11) was possible thanks to the boundedness of diffuse radiance. Equation (1.11) is autonomous and can be integrated trivially, giving solution

$$F_\nu^{\mathrm{dir}} = F_\nu^{\odot} \exp\left(-\frac{\delta_\nu}{\mu_0}\right), \tag{1.12}$$

where μ_0 is the cosine of solar zenith angle, and $F_\nu^{\odot}$ is DNI at the TOA. This solution can be inserted into equation (1.10), where it occurs in the source term converting direct radiation into diffuse one.

Applicability of the plane-parallel approximation becomes problematic at high horizontal resolutions, where the cumuliform clouds become resolved and their

---

[2]Mathematically, $\delta(\mathbf{n}, \mathbf{n}')$ is a generalized bidirectional function or distribution, acting on arbitrary function h on the sphere as $\oint_{4\pi} \delta(\mathbf{n}, \mathbf{n}')h(\mathbf{n}')\,\mathrm{d}\Omega' = h(\mathbf{n})$. It thus fulfils normalization condition $\oint_{4\pi} \delta(\mathbf{n}, \mathbf{n}')\,\mathrm{d}\Omega' = 1$. Coordinate expression for the Dirac delta function on the sphere is $\delta(\mathbf{n}, \mathbf{n}') = \delta(\mu - \mu')\delta(\phi - \phi')$.

eventual 3D radiative effects can no longer be parameterized, since they start to produce non-negligible lateral radiative exchanges with neighbouring model columns. On the other hand, plane-parallel approximation is well justified at low horizontal resolutions, where the resolved horizontal gradients of the cloud and temperature fields are much smaller than the vertical ones, so that lateral exchanges can be safely ignored. Another criterion illustrating applicability of the plane-parallel approximation in the shortwave spectrum is the horizontal shift of the cloud shadows. For low and medium clouds it typically reaches several km, which is still acceptable for horizontal mesh sizes around $10\,\mathrm{km}$, but becomes questionable for horizontal mesh sizes $1\,\mathrm{km}$ and finer. When the cloud field on *resolved* horizontal scales is homogeneous, lateral radiative effects cancel when evaluating gridbox energy budget. However, on the edges of cloudy regions such cancellation does not occur, and it breaks down completely when the model starts to resolve horizontal non-homogeneities of the cloud field.

b) Two-stream approximation

Second step, addressing the angular integration, makes additional assumptions transforming equation (1.10) into a linear system of ordinary differential equations. Most natural way is to evaluate azimuthally integrated diffuse radiance $I_\nu^{\mathrm{diff}}(\mu)$ only for a discrete set of directions μ and to replace scattering integral with the quadrature rule. In the simplest case, only two directions are used. Integral on interval $[-1, 1]$ can then be replaced by the sum of one-node Gaussian quadratures on intervals $[-1, 0]$ and $[0, 1]$:

$$\int_{-1}^{1} P_\nu(\mu, \mu') I_\nu^{\mathrm{diff}}(\mu')\, \mathrm{d}\mu' \approx P_\nu(\mu, -\tfrac{1}{2}) I_\nu^{\mathrm{diff}}(-\tfrac{1}{2}) + P_\nu(\mu, \tfrac{1}{2}) I_\nu^{\mathrm{diff}}(\tfrac{1}{2}) \tag{1.13}$$

The same Gaussian quadratures can be applied to definitions of upward diffuse flux $F_\nu^\uparrow$ and downward diffuse flux $F_\nu^\downarrow$, relating them to diffuse radiances $I_\nu^{\mathrm{diff}}(-\tfrac{1}{2})$ and $I_\nu^{\mathrm{diff}}(\tfrac{1}{2})$:

$$F_\nu^\uparrow \equiv -\int_{-1}^{0} I_\nu^{\mathrm{diff}}(\mu)\mu\, \mathrm{d}\mu \approx \frac{1}{2} I_\nu^{\mathrm{diff}}(-\tfrac{1}{2}) \tag{1.14}$$

$$F_\nu^\downarrow \equiv \int_{0}^{1} I_\nu^{\mathrm{diff}}(\mu)\mu\, \mathrm{d}\mu \approx \frac{1}{2} I_\nu^{\mathrm{diff}}(\tfrac{1}{2}) \tag{1.15}$$

Total upward flux has only diffuse component, since in most circumstances underlying surface is rough, converting direct solar ray into diffuse reflected light. Total downward flux alias GHI (Global Horizontal Irradiance) is given by the sum of diffuse and direct components, where the latter is DNI multiplied by the cosine of solar zenith angle in order to get direct flux S_ν across horizontal surface:

$$\mathrm{GHI}_\nu \equiv F_\nu^\downarrow + \mu_0 F_\nu^{\mathrm{dir}} \equiv F_\nu^\downarrow + S_\nu \tag{1.16}$$

Assuming further that the scattering phase function is linear in its argument $\mu = \cos\Theta$, full information about it is contained in the first-order moment alias asymmetry factor g_ν:

$$P_\nu(\mu) = 1 + 3g_\nu\mu \tag{1.17}$$

$$g_\nu \equiv \frac{1}{2}\int_{-1}^{1} P_\nu(\mu)\mu\, \mathrm{d}\mu \tag{1.18}$$

Azimuthally averaged phase function (1.17) is:

$$P_\nu(\mu, \mu') = 1 + 3g_\nu \mu \mu' \qquad (1.19)$$

Quadrature rules (1.13)–(1.15) are exact as long as integrand is at most first-order polynomial in μ on intervals $[-1, 0)$ and $(0, 1]$, with possible discontinuity at $\mu = 0$. With the scattering phase function (1.17) they would be exact if the azimuthally integrated diffuse radiance $I_\nu^{\mathrm{diff}}(\mu)$ had constant values for $\mu < 0$ and for $\mu > 0$. This is the case when the diffuse radiance $I_\nu^{\mathrm{diff}}(\mathbf{n})$ is *hemispheric constant*.

Sampling the azimuthally integrated diffuse radiance $I_\nu^{\mathrm{diff}}(\mu)$ in only one upward and one downward directions leads to the so-called *two-stream approximation*. Its final formulation replaces diffuse radiances with upward and downward diffuse fluxes and can be written in a general shape

$$\frac{\mathrm{d}F_\nu^\uparrow}{\mathrm{d}\delta_\nu} = \alpha_{1\nu} F_\nu^\uparrow - \alpha_{2\nu} F_\nu^\downarrow - (\alpha_{1\nu} - \alpha_{2\nu})\pi B_\nu(T) - \alpha_{3\nu} F_\nu^\odot \exp\left(-\frac{\delta_\nu}{\mu_0}\right) \qquad (1.20)$$

$$\frac{\mathrm{d}F_\nu^\downarrow}{\mathrm{d}\delta_\nu} = \alpha_{2\nu} F_\nu^\uparrow - \alpha_{1\nu} F_\nu^\downarrow + (\alpha_{1\nu} - \alpha_{2\nu})\pi B_\nu(T) + \alpha_{4\nu} F_\nu^\odot \exp\left(-\frac{\delta_\nu}{\mu_0}\right) \qquad (1.21)$$

$$\alpha_{1\nu} = U[1 - \varpi_\nu(1 - \bar{\beta}_\nu)] \qquad \alpha_{3\nu} = \varpi_\nu \beta_\nu(\mu_0) \qquad (1.22)$$

$$\alpha_{2\nu} = U\varpi_\nu \bar{\beta}_\nu \qquad \alpha_{4\nu} = \varpi_\nu[1 - \beta_\nu(\mu_0)], \qquad (1.23)$$

where U is a diffusivity factor (see section 2.4 of Mašek et al. [2016]), ϖ_ν is the single scattering albedo, $\beta_\nu(\mu_0)$ is the upscatter fraction for direct solar ray, and $\bar{\beta}_\nu$ is the backscatter fraction for the incident radiation isotropic over hemisphere.

Choice of the quadrature rules (1.13)–(1.15), combined with the scattering phase function (1.17), leads to formulas:

$$\beta_\nu(\mu_0) = \frac{1}{2} - \frac{3}{4}g_\nu \mu_0 \qquad (1.24)$$

$$\bar{\beta}_\nu = \frac{1}{2} - \frac{3}{8}g_\nu \qquad (1.25)$$

These, together with specification of the diffusivity factor U, select a particular two-stream formulation from all the possibilities covered by the general equations (1.20)–(1.23). It should be noted that the phase function (1.17) is physically meaningful (non-negative) only for asymmetry factor $g_\nu \in [-\frac{1}{3}, \frac{1}{3}]$. Still, the above derived two-stream formulation can be used as long as the upscatter fraction (1.24) remains in the physical range $[0, 1]$, which yields weaker constraint $g_\nu \in [-\frac{2}{3}, \frac{2}{3}]$. This limitation can be removed completely by so-called delta-scaling, described in the next subsection.

The upscatter and backscatter fractions (1.24)–(1.25) can be expressed as integrals

$$\beta_\nu(\mu_0) \equiv \frac{1}{2}\int_{-1}^0 P_\nu(\mu_0, \mu)\,\mathrm{d}\mu \qquad \mu_0 \geq 0 \qquad (1.26)$$

$$\bar{\beta}_\nu \equiv \int_0^1 \beta_\nu(\mu_0)\,\mathrm{d}\mu_0, \qquad (1.27)$$

13

where the azimuthally averaged phase function is given by formula (1.19). One might be tempted to use the true phase function in integral (1.26), in order to get accurate upscatter and backscatter fractions. However, such effort does not make much sense in the two-stream framework, where the assumed two-parametric angular distribution of diffuse radiation is another accuracy limitation. Stated differently, backscatter fraction (1.27) is exact only for hemispheric constant incident radiation, while for different angular distributions it becomes approximate. Substantial improvement of accuracy is thus not possible without going to the higher angular resolution alias more streams.

It can be concluded that the two-stream approximation reduces the radiative transfer problem to the linear system of ordinary differential equations (1.20)–(1.21) for upward and downward diffuse fluxes. The system is non-homogeneous, with thermal emission and scattering of direct solar radiation acting as the source terms. For a homogeneous layer, the system can be integrated analytically, giving linear relation between incoming and outgoing fluxes:[3]

$$S_{B\nu} = a_{1\nu} S_{T\nu} \tag{1.28}$$

$$\begin{bmatrix} F_{B\nu}^{\downarrow} \\ F_{T\nu}^{\uparrow} \end{bmatrix} = \begin{bmatrix} a_{4\nu} & a_{5\nu} \\ a_{5\nu} & a_{4\nu} \end{bmatrix} \cdot \begin{bmatrix} F_{T\nu}^{\downarrow} \\ F_{B\nu}^{\uparrow} \end{bmatrix} + \begin{bmatrix} 1 - a_{4\nu} - a_{5\nu} \\ 1 - a_{4\nu} - a_{5\nu} \end{bmatrix} \cdot B_{\nu}(T) + \begin{bmatrix} a_{2\nu} \\ a_{3\nu} \end{bmatrix} \cdot S_{T\nu} \tag{1.29}$$

Subscripts 'T' and 'B' denote fluxes at the top and bottom interfaces of the layer, $a_{1\nu}$ is the direct transmission, $a_{2\nu}$ is the direct-diffuse transmission (sum $a_{1\nu} + a_{2\nu}$ is the total transmission), $a_{3\nu}$ is the direct-diffuse reflectivity or plane albedo, $a_{4\nu}$ is the diffuse or global transmission, and finally $a_{5\nu}$ is the diffuse reflectivity or spherical albedo. Quantity $(1 - a_{4\nu} - a_{5\nu})$ is the global absorption, and by Kirchhoff's law it is equal to the layer emissivity. Transmissions and reflectivities $a_{1\nu}$ to $a_{5\nu}$ fully specify optical properties of the layer, depending on the two-stream coefficients $\alpha_{1\nu}$ to $\alpha_{4\nu}$ and on the layer optical depth $\Delta\delta_{\nu}$. Their analytical formulations are listed in appendix C of Mašek et al. [2016].

c) Delta-scaling

In the meteorological context, backward scattering never prevails. It is therefore sufficient to assume asymmetry factors $g_{\nu} \geq 0$. However, scattering by aerosol and cloud particles is *strongly anisotropic*, dominated by near-forward directions. The phase function (1.17) cannot represent it realistically enough, especially if there is a restriction $g_{\nu} \leq \frac{2}{3}$, necessary for getting meaningful upscatter fraction (1.24). Still, performance of the two-stream approximation for the strongly forward-scattering phase functions can be improved significantly by *delta-scaling*. As explained by McKellar and Box [1981], the idea is to exploit scaling invariance of the radiative transfer equation in order to transform the problem with highly asymmetric phase function into an equivalent problem with more isotropic one. This equivalent problem can be solved more accurately by the two-stream approximation, since it better fits its assumptions.

---

[3]Linear relation between incoming and outgoing fluxes would be obtained also for a non-homogeneous layer, but in such case reflectivities for upward and downward diffuse radiation can be different.

Delta-scaling is based on the fact that when the two scattering phase functions P_ν and P'_ν are related by

$$P_\nu(\mathbf{n} \cdot \mathbf{n}') = 4\pi f_\nu \delta(\mathbf{n}, \mathbf{n}') + (1 - f_\nu) P'_\nu(\mathbf{n} \cdot \mathbf{n}'),^4 \qquad (1.30)$$

radiative transfer equation (1.3) with the phase function $P_\nu(\mu)$, single scattering albedo ϖ_ν and optical depth δ_ν has the same solution as for the scaled phase function $P'_\nu(\mu)$, formulated in the scaled variables ϖ'_ν and δ'_ν:

$$\varpi'_\nu = \frac{(1 - f_\nu)\varpi_\nu}{1 - f_\nu\varpi_\nu} \qquad (1.31)$$

$$\mathrm{d}\delta'_\nu = (1 - f_\nu\varpi_\nu)\,\mathrm{d}\delta_\nu \quad \Rightarrow \quad \delta'_\nu = \int_0^{\delta_\nu} (1 - f_\nu\varpi_\nu)\,\mathrm{d}\delta_\nu \qquad (1.32)$$

It means that radiances of the two solutions correspond as:

$$I_\nu(\mu, \delta_\nu) = I'_\nu(\mu, \delta'_\nu) \qquad (1.33)$$

When the scaled phase function $P'_\nu(\mu)$ is assumed continuous, unscaled phase function $P_\nu(\mu)$ has a Dirac peak sending proportion f_ν of scattered radiation in the forward direction. Factor 4π in equation (1.30) comes from the requirement that both $P_\nu(\mu)$ and $P'_\nu(\mu)$ are normalized. Realizing that asymmetry factor can be expressed as the spherical integral

$$g_\nu = \frac{1}{4\pi} \oint_{4\pi} P_\nu(\mathbf{n} \cdot \mathbf{n}')\,\mathbf{n} \cdot \mathbf{n}'\,\mathrm{d}\Omega', \qquad (1.34)$$

relation between scaled and unscaled asymmetry factors can be readily obtained from equation (1.30):

$$g'_\nu = \frac{g_\nu - f_\nu}{1 - f_\nu} \qquad (1.35)$$

Supposing $0 \leq f_\nu \leq g_\nu$, delta-scaling (1.30)–(1.32) implies inequalities:

$$0 \leq g'_\nu \leq g_\nu \qquad\qquad \varpi'_\nu \leq \varpi_\nu \qquad\qquad \delta'_\nu \leq \delta_\nu \qquad (1.36)$$

It means that the delta-scaled system is more isotropic and optically thinner than the unscaled one. It also has lower relative importance of scattering.

Scaling invariance (1.30)–(1.32) holds also for the radiative transfer equation in the shape (1.10)–(1.11), i.e. when the diffuse and direct radiances are separated according to equation (1.9). In such case, however, boundedness of the diffuse radiance implies that the direct radiation scattered via forward Dirac peak is not converted to diffuse radiation, but it is retained in the direct beam. It can be seen from equation (1.12), whose scaled variant increases DNI, so that it does not represent unscattered solar radiation any longer:

$$F_\nu^{\mathrm{dir}'} = F_\nu^{\odot} \exp\left(-\frac{\delta'_\nu}{\mu_0}\right) \geq F_\nu^{\odot} \exp\left(-\frac{\delta_\nu}{\mu_0}\right) = F_\nu^{\mathrm{dir}} \qquad (1.37)$$

---

[4]In the literature, equation (1.30) is usually written as $P_\nu(\mu) = 2f_\nu\delta(1 - \mu) + (1 - f_\nu)P'_\nu(\mu)$, which can be obtained from the azimuthally averaged phase function $P_\nu(\mu, \mu') = 2f_\nu\delta(\mu - \mu') + (1 - f_\nu)P'_\nu(\mu, \mu')$ by setting $\mu' = 1$. For more details see Wiscombe [1977].

This is not a problem at all, since the unscattered solar radiation can still be obtained from unscaled equation (1.12). Downward flux of the scattered radiation can then be retrieved as:

$$F_\nu^\downarrow = F_\nu^{\downarrow'} + \mu_0 F_\nu^{\mathrm{dir}'} - \mu_0 F_\nu^{\mathrm{dir}} = F_\nu^{\downarrow'} + S_\nu' - S_\nu \qquad (1.38)$$

In any case, the truly unscattered solar flux is of little practical importance, since the measuring instruments always deliver higher value, collecting all radiation (both unscattered and scattered) coming from a circumsolar region covering the solar disk and its near neighbourhood. Should the model DNI be verified against measurements, this effect must be accounted for at least approximately, following e.g. Mauno et al. [2011].

In order to use delta-scaling, proportion of forward Dirac scattering f_ν must be specified. The most common choice in the two-stream case is:

$$f_\nu = g_\nu^2 \quad \Rightarrow \quad g' = \frac{g}{1+g} \qquad (1.39)$$

It ensures that with the scaled phase function

$$P_\nu'(\mu) = 1 + 3g_\nu'\mu, \qquad (1.40)$$

the first and second-order moments of the unscaled phase function $P_\nu(\mu)$ are equal to those of Henyey and Greenstein [1941] phase function. According to Hansen [1969], the latter phase function is a good approximation for Lorenz-Mie scattering in optically thick atmospheres. Moreover, choice (1.39) ensures $g_\nu' \leq \frac{1}{2}$, so that the scaled upscatter and backscatter fractions having the shape

$$\beta_\nu'(\mu_0) = \frac{1}{2} - \frac{3}{4}g_\nu'\mu_0 \qquad (1.41)$$

$$\bar{\beta} = \frac{1}{2} - \frac{3}{8}g_\nu', \qquad (1.42)$$

are always from the physical range $[0, 1]$.

There exist many (delta-)two-stream formulations, the most common ones being compared e.g. by Meador and Weaver [1980], King and Harshvardhan [1986], and Harshvardhan and King [1993]. None of them is accurate for all combinations of optical depths, single scattering albedos, asymmetry factors and sun elevations, so that compromises must be made when picking formulation suitable for NWP usage. One frequent choice is the delta-Eddington approximation (Joseph et al. [1976]), employing the scaled phase function (1.40) with the proportion of forward Dirac scattering (1.39), and assuming azimuthally integrated diffuse radiance $I_\nu(\mu)$ linear in μ in the whole range $[-1, 1]$. The choice of the ACRANEB and ACRANEB2 schemes, characterized by equations (1.39)–(1.42), is different. It was first introduced by Zdunkowski and Korb [1985] as a variant of PIFM (Practical Improved Flux Method). Here it will be referred to as the delta-two-stream formulation of Ritter and Geleyn [1992], who derived it in a more straightforward and conceptually cleaner way.[5] It can be viewed as a special case of Stamnes and Swanson [1981] discrete ordinate method with only two streams, approximating the Henyey-Greenstein scattering phase function by

---

[5]Equivalence of the two formulations is proven in appendix A of Mašek et al. [2016].

Wiscombe [1977] delta-M method with the order of approximation $M = 1$. Key ingredient is the approximation of scattering integral by the separate Gaussian quadratures on intervals $[-1, 0]$ and $[0, 1]$, leading to formula (1.13). Advantages of this 'double-Gauss' approach are explained in section C of Stamnes et al. [1988].

It is instructive to compare accuracy of the delta-Eddington and Ritter-Geleyn delta-two-stream formulations. On figure 1.4 this is done for a non-absorbing homogeneous layer, illuminated from the top by the collimated beam and having non-reflective bottom boundary. Case of conservative scattering $\varpi_\nu = 1$ was taken intentionally, since it is most sensitive to the treatment of angular integration. Error of the total transmission $a_{1\nu} + a_{2\nu}$ is shown for the range of sun elevations (represented by the cosine μ_0 of solar zenith angle) and layer optical depths δ_ν. Reference solution was obtained by the Monte Carlo simulation, using the Henyey-Greenstein phase function with asymmetry factor $g_\nu = 0.843$. Such phase function roughly approximates scattering by the fair weather cumulus clouds at wavelength $\lambda = 754\,\text{nm}$, corresponding to frequency $\nu = 398\,\text{THz}$ (for detailed phase function see King and Harshvardhan [1986]). It can be seen that in absolute terms, the delta-Eddington approximation is most accurate for high sun elevations and also for optically thick layers. The total transmission error is mostly positive, reaching maximum around $\mu_0 = 0.05$ and $\delta_\nu = 0.1$. Error structure of the Ritter-Geleyn formulation is more dipole-like, with positive error for optically thin layers at low sun (similar to delta-Eddington), and with negative error for optically thick layers at high sun. Maximum negative error is observed around $\mu_0 = 1$ and $\delta_\nu = 15$. The best accuracy is obtained roughly along diagonal going from optically thick layers at low sun towards optically thin layers at high sun.

Figure 1.4 demonstrates also beneficial impact of delta-scaling. Without it, the Ritter-Geleyn formulation would strongly underestimate the total transmission in a substantial part of the (μ_0, δ_ν) domain. It should be noted that in this case, the total transmission of optically thin layers at high sun exceeds the physical limit 1. This is because asymmetry factor g_ν exceeds $\frac{2}{3}$, which is the limit for physically meaningful unscaled upscatter fraction $\beta_\nu(\mu_0)$.

In case of conservative scattering investigated above, accuracy of the delta-Eddington and Ritter-Geleyn formulations is comparable. This is confirmed also by the left panel on figure 1.5, comparing their diffuse reflectivities with Monte-Carlo reference (red). Ritter-Geleyn formulation (green) is superior for optical depths below 1, but for higher optical depths it overestimates the diffuse reflectivity, reaching maximum absolute error around 0.10. On the other hand, the delta-Eddington approximation (yellow) slightly underestimates the diffuse reflectivity for optical depths below 10, but for deeper layers it becomes nearly perfect. The Ritter-Geleyn formulation without delta-scaling (cyan) would be unusable, suffering from positive bias in the whole range of optical depths, reaching maximum absolute error around 0.25. This again demonstrates beneficial impact of delta-scaling. For the Eddington approximation, however, diffuse transmission and reflectivity are not influenced by delta-scaling. This is sometimes source of confusion, leading to the false belief that, in the absence of direct flux, delta-scaling is useless. It is only true when $\alpha_{1\nu}\,\mathrm{d}\delta_\nu$ and $\alpha_{2\nu}\,\mathrm{d}\delta_\nu$ are scaling invariants,
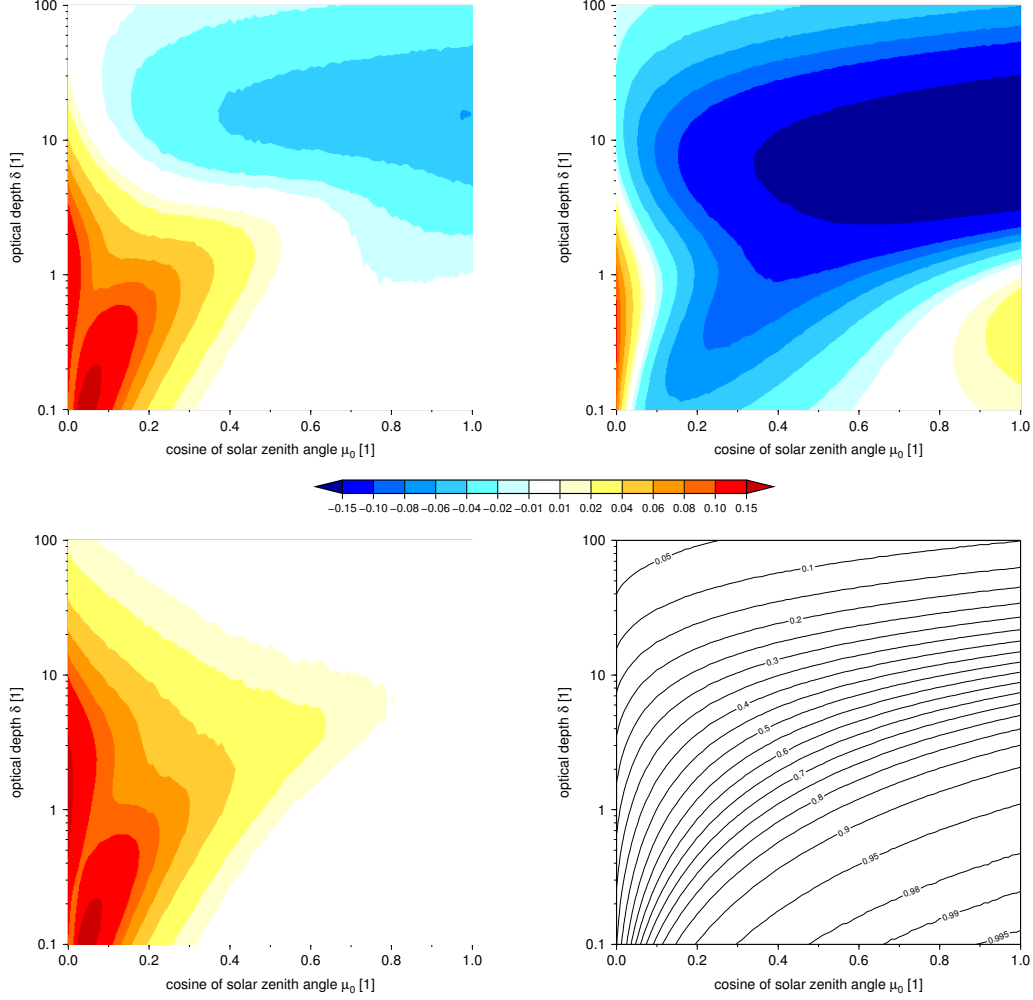
Figure 1.4: Accuracy of various (delta-)two-stream formulations demonstrated for a homogeneous layer with single scattering albedo $\varpi_\nu = 1$ and asymmetry factor $g_\nu = 0.843$. Error of the total transmission $(a_{1\nu} + a_{2\nu})$ is shown as the function of sun elevation and optical depth. **Top left:** Error of the Ritter-Geleyn formulation. **Top right:** Error of the Ritter-Geleyn formulation, but without delta-scaling. **Bottom left:** Error of the delta-Eddington approximation. **Bottom right:** Reference solution obtained by the Monte Carlo simulation, using the Henyey-Greenstein phase function.
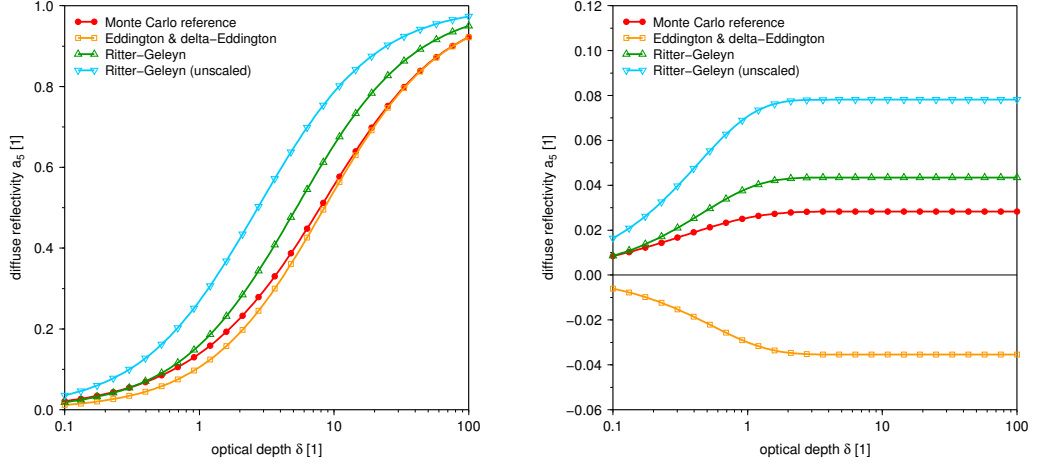
Figure 1.5: Dependence of spherical albedo $a_{5\nu}$ on the optical depth δ_ν for a homogeneous layer with asymmetry factor $g_\nu = 0.843$. Reference Monte Carlo simulation used the Henyey-Greenstein phase function. Same (delta-)two-stream formulations as on figure 1.4 are shown. **Left:** Non-absorbing case with single scattering albedo $\varpi_\nu = 1$. **Right:** Strongly absorbing case with single scattering albedo $\varpi_\nu = 0.5$.

which is the case if and only if the backscatter fraction scales as:

$$\bar{\beta}'_\nu = \frac{\bar{\beta}_\nu}{1 - f_\nu} \tag{1.43}$$

It can be verified easily that the scaling relation (1.43) holds for the Eddington approximation with $\bar{\beta}_\nu = \frac{1}{8}(4 - 3g_\nu - 1/\varpi_\nu)$, but *not* for the Ritter-Geleyn formulation with $\bar{\beta}_\nu = \frac{1}{8}(4 - 3g_\nu)$.

So far it seems that the delta-Eddington and Ritter-Geleyn formulations are of similar quality. What makes distinction between them are cases with strong absorption and sufficiently asymmetric phase function. One such case is shown on the right panel of figure 1.5, having the same phase function as on the left panel, but with single scattering albedo $\varpi_\nu = 0.5$. In such conditions, the delta-Eddington approximation yields negative spherical albedo $a_{5\nu}$ for any optical depth δ_ν. This is because in the delta-Eddington approximation, the backscatter fraction $\bar{\beta}'_\nu$ contains extra term $-1/(8\varpi'_\nu)$, that can eventually make it negative. The Ritter-Geleyn formula 1.42 is free of such term, always delivering physically meaningful backscatter fraction $\bar{\beta}'_\nu$. Resulting spherical albedo $a_{5\nu}$ is overestimated especially for higher optical depths, but this is a minor problem compared to the negative delta-Eddington values.

The delta-two-stream formulation suitable for NWP usage should be reliable for all relevant combinations of sun elevation, single scattering albedo, asymmetry factor and optical depth. The Ritter-Geleyn formulation was therefore found *superior* to the widely used delta-Eddington approximation, since it can be meaningfully used in a wider range of conditions. The delta-Eddington approximation is more accurate for optically thick nearly conservative layers, but the accuracy of the Ritter-Geleyn formulation, preventing unphysical behaviour, should be more uniform across parameter space.

19

Finally, it should be noted that for reference solution, the global transmission $a_{4\nu}$ and spherical albedo $a_{5\nu}$ are related to the total transmission $(a_{1\nu} + a_{2\nu})$ and plane albedo $a_{3\nu}$ by integral relations

$$a_{4\nu} = 2 \int_0^1 (a_{1\nu} + a_{2\nu}) \mu_0 \, \mathrm{d}\mu_0 \qquad (1.44)$$

$$a_{5\nu} = 2 \int_0^1 a_{3\nu} \mu_0 \, \mathrm{d}\mu_0, \qquad (1.45)$$

while for the examined (delta-)two-stream approximations these relations *do not hold*. Harshvardhan and King [1993] used relations (1.44)–(1.45) to construct integrated two-stream approximations, rederiving the global transmission $a_{4\nu}$ and spherical albedo $a_{5\nu}$ by evaluating the angular integrals numerically. They have shown that integrated delta-Eddington approximation employing the two-node Gaussian quadrature is free from unphysical behaviour. Such approach implies computational overhead, since the total transmission and plane albedo must be evaluated not only for actual sun elevation, but also at the two quadrature nodes. Moreover, it points to the internal inconsistency of the original schemes, which is more severe for the delta-Eddington approximation than for the Ritter-Geleyn formulation.

d) Adding method

For a homogeneous layer, the delta-two-stream approximation yields the linear relations (1.28)–(1.29) between incoming and outgoing fluxes. To accomplish the vertical integration, one must deal with the non-homogeneous atmosphere. The most natural way is to slice the assumed atmospheric column into homogeneous layers, and to apply relations (1.28)–(1.29) in each layer, using its actual optical properties. Fluxes leaving one layer enter the next layer and the solution is made unique by prescribing the top and bottom boundary conditions. This approach is known as *adding method*, since it builds up non-homogeneous optical path by adding smaller homogeneous pieces. Resulting system for fluxes at the layer interfaces remains linear, with fixed number of non-zero diagonals. Adding method also enables to extend the plane-parallel approximation by incorporating the non-trivial cloud geometry, following Geleyn and Hollingsworth [1979]. This is the first step beyond purely 1D radiative transfer, but its impact remains limited to the assumed atmospheric column.

In order to include partial cloud cover, each layer of assumed model column is divided into the *clearsky* part containing gases and aerosols, and the *cloudy* part containing gases, aerosols, cloud droplets and ice particles. Cloud in the layer l occupies fraction n_l of the gridbox, as depicted on figure 1.6 (atmospheric layers are indexed from the top to bottom, ranging from 1 to L). Since the optical properties of the *homogeneous* clearsky and cloudy parts of the layer are different, delta-two-stream system (1.29) must be applied separately in each part. For the
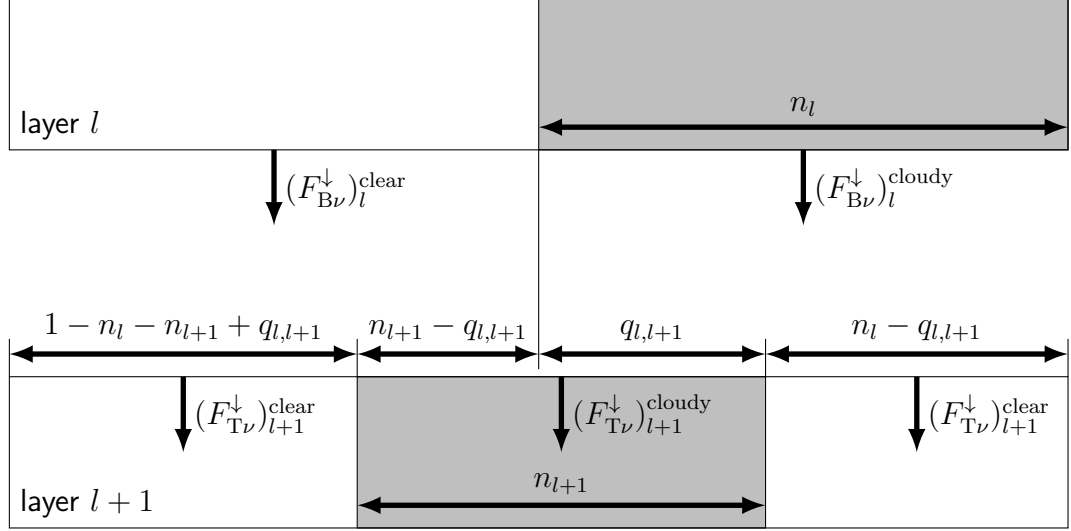
20

Figure 1.6: Cloud overlap geometry of adjacent layers l and $l+1$, having cloud fractions n_l and n_{l+1}. Cloudy parts of the layers are grey, and they overlap on the fraction of gridbox $q_{l,l+1}$. For clarity, the layers on diagram are detached. In reality they are touching.

model level l it reads:

$$
\begin{bmatrix} F_{B\nu}^{\downarrow} \\ F_{T\nu}^{\uparrow} \end{bmatrix}_l^{\text{clear}} = \begin{bmatrix} a_{4\nu} & a_{5\nu} \\ a_{5\nu} & a_{4\nu} \end{bmatrix}_l^{\text{clear}} \cdot \begin{bmatrix} F_{T\nu}^{\downarrow} \\ F_{B\nu}^{\uparrow} \end{bmatrix}_l^{\text{clear}} + \begin{bmatrix} J_{B\nu}^{\downarrow} \\ J_{T\nu}^{\uparrow} \end{bmatrix}_l^{\text{clear}} \tag{1.46}
$$

$$
\begin{bmatrix} F_{B\nu}^{\downarrow} \\ F_{T\nu}^{\uparrow} \end{bmatrix}_l^{\text{cloudy}} = \begin{bmatrix} a_{4\nu} & a_{5\nu} \\ a_{5\nu} & a_{4\nu} \end{bmatrix}_l^{\text{cloudy}} \cdot \begin{bmatrix} F_{T\nu}^{\downarrow} \\ F_{B\nu}^{\uparrow} \end{bmatrix}_l^{\text{cloudy}} + \begin{bmatrix} J_{B\nu}^{\downarrow} \\ J_{T\nu}^{\uparrow} \end{bmatrix}_l^{\text{cloudy}} \tag{1.47}
$$

Symbols $J_{B\nu}^{\downarrow}$ and $J_{T\nu}^{\uparrow}$ are shorthand notations for the source term, containing contributions from thermal emission and scattering of the direct solar radiation.

Equations (1.46)–(1.47) suppose no lateral exchanges between the clearsky and cloudy parts of the layer. On the layer interfaces, however, clearsky and cloudy fluxes are redistributed according to cloud geometry shown on figure 1.6. If the adjacent cloud layers l and $l+1$ overlap on fraction $q_{l,l+1}$ of the gridbox, then the fluxes leaving the bottom of layer l should be redistributed before entering the top of layer $l+1$ according to relation:

$$
\begin{bmatrix} F_{T\nu}^{\text{clear}} \\ F_{T\nu}^{\text{cloudy}} \end{bmatrix}_{l+1}^{\downarrow} = \begin{bmatrix} \dfrac{1 - n_l - n_{l+1} + q_{l,l+1}}{1 - n_{l+1}} & \dfrac{n_l - q_{l,l+1}}{1 - n_{l+1}} \\ \dfrac{n_{l+1} - q_{l,l+1}}{n_{l+1}} & \dfrac{q_{l,l+1}}{n_{l+1}} \end{bmatrix} \cdot \begin{bmatrix} F_{B\nu}^{\text{clear}} \\ F_{B\nu}^{\text{cloudy}} \end{bmatrix}_l^{\downarrow} \tag{1.48}
$$

Analogously, the fluxes leaving the top of layer $l+1$ should be redistributed before entering the bottom of layer l:

$$
\begin{bmatrix} F_{B\nu}^{\text{clear}} \\ F_{B\nu}^{\text{cloudy}} \end{bmatrix}_l^{\uparrow} = \begin{bmatrix} \dfrac{1 - n_l - n_{l+1} + q_{l,l+1}}{1 - n_l} & \dfrac{n_{l+1} - q_{l,l+1}}{1 - n_l} \\ \dfrac{n_l - q_{l,l+1}}{n_l} & \dfrac{q_{l,l+1}}{n_l} \end{bmatrix} \cdot \begin{bmatrix} F_{T\nu}^{\text{clear}} \\ F_{T\nu}^{\text{cloudy}} \end{bmatrix}_{l+1}^{\uparrow} \tag{1.49}
$$

Matrix rows in equations (1.48)–(1.49) contain redistribution weights, summing up to one. It must be stressed that these equations are formulated for the *flux densities*, while in the literature they are often given for the flux densities multiplied by the corresponding gridbox fractions.[6] When cloud fraction in the target layer is one or zero, redistribution weights giving the flux density entering its clearsky or cloudy part, respectively, are undetermined. This is not a problem, since the flux density in the given part is of no interest when this part occupies zero area.

Several hypotheses can be made about overlap between the adjacent cloud layers. Two limit cases are *random* overlap with $q_{l,l+1} = n_l n_{l+1}$, and *maximum* overlap with $q_{l,l+1} = \min(n_l, n_{l+1})$. In principle, less than random overlap can occur, but it is rarely observed. When maximum overlap between the adjacent cloud layers is used for a multi-layer cloud, it is referred to as *maximum-random* overlap. This is because geometry of distant cloud layers not restricted by the adjacent overlaps is random. As remarked by Geleyn and Hollingsworth [1979], positions of cloudy parts separated by cloud free air become totally independent when maximum-random overlap is applied.

In the NWP models, simplest choice was to use random cloud overlap. This is because it can be collapsed into the shape where the layer transmissions and reflectivities are averaged between clearsky and cloudy parts, and the delta-two-stream and adding system is solved without considering cloud geometry. However, random cloud overlap becomes insufficient for higher vertical resolutions, since it ignores correlations between positions of the cloudy parts once the cloud is sliced finely enough. Much more realistic is maximum-random cloud overlap, that is still widely used. Its drawback are overestimated overlaps between distant cloudy parts of the *contiguous* cloud, while Hogan and Illingworth [2000] found that the cloud layers separated by more than 4 km overlap randomly, regardless the cloud is contiguous or not. For this reason they proposed a generalized cloud overlap in the shape

$$q_{l,l+1} = (1 - \alpha)n_l n_{l+1} + \alpha \min(n_l, n_{l+1}), \tag{1.50}$$

where α is the weight placing the adjacent overlap between random ($\alpha = 0$) and maximum ($\alpha = 1$). Analyzing experimental data, Hogan and Illingworth [2000] concluded that the weight α can be well approximated by a decaying exponential of the geometric distance between the layer centres. Using this shape of α leads to so-called *exponential-random* cloud overlap, variant of which is used also in a recent version of the ACRANEB2 scheme.

Delta-two-stream and adding system with L atmospheric layers contains $8L$ unknown fluxes (2 incoming and 2 outgoing fluxes for the clearsky part, 2 incoming and 2 outgoing fluxes for the cloudy part of each layer). There are $4L$ two-stream equations (2 for the clearsky part and 2 for the cloudy part of each layer). These are complemented by $4L - 4$ redistribution relations (4 at each internal layer interface). In order to close the system, 4 boundary conditions must be prescribed. At the TOA (top of the layer 1), incoming diffuse fluxes are zero:

$$(F_{T\nu}^{\downarrow})_1^{\text{clear}} = 0 \tag{1.51}$$

$$(F_{T\nu}^{\downarrow})_1^{\text{cloudy}} = 0 \tag{1.52}$$

---

[6]The reason is that the latter quantities from the clearsky and cloudy parts can be added to get overall gridbox value, while the flux densities must be averaged.

At the Earth's surface (bottom of the layer L), both emission and reflection can take place, so that the boundary condition has a general shape:

$$(F_{\mathrm{B}\nu}^{\uparrow})_L^{\mathrm{clear}} = \epsilon_{\mathrm{S}\nu}\pi B_\nu(T_\mathrm{S}) + \bar{\alpha}_{\mathrm{S}\nu}(F_{\mathrm{B}\nu}^{\downarrow})_L^{\mathrm{clear}} + \alpha_{\mathrm{S}\nu}(\mu_0)(S_{\mathrm{B}\nu})_L^{\mathrm{clear}} \tag{1.53}$$

$$(F_{\mathrm{B}\nu}^{\uparrow})_L^{\mathrm{cloudy}} = \epsilon_{\mathrm{S}\nu}\pi B_\nu(T_\mathrm{S}) + \bar{\alpha}_{\mathrm{S}\nu}(F_{\mathrm{B}\nu}^{\downarrow})_L^{\mathrm{cloudy}} + \alpha_{\mathrm{S}\nu}(\mu_0)(S_{\mathrm{B}\nu})_L^{\mathrm{cloudy}} \tag{1.54}$$

In the equations above, $\epsilon_{\mathrm{S}\nu}$ and T_S are surface emissivity and temperature, while $\alpha_{\mathrm{S}\nu}(\mu_0)$ and $\bar{\alpha}_{\mathrm{S}\nu}$ are surface plane and spherical albedos, respectively. They are related by integral formula analogous to equation (1.45):

$$\bar{\alpha}_{\mathrm{S}\nu} = 2\int_0^1 \alpha_{\mathrm{S}\nu}(\mu_0)\mu_0\,\mathrm{d}\mu_0 \tag{1.55}$$

Since the surface is non-transparent, its emissivity is related to spherical albedo by formula:

$$\epsilon_{\mathrm{S}\nu} = 1 - \bar{\alpha}_{\mathrm{S}\nu} \tag{1.56}$$

Cloud geometry influences also the source term, namely its part representing scattering of the direct solar radiation. At the TOA, direct solar flux across horizontal plane is given as DNI scaled by cosine of solar zenith angle:

$$(S_{\mathrm{T}\nu})_1^{\mathrm{clear}} = (S_{\mathrm{T}\nu})_1^{\mathrm{cloudy}} = \mu_0 F_\nu^\odot \tag{1.57}$$

It is propagated across the clearsky and cloudy parts of the layer l by applying equation (1.28):

$$(S_{\mathrm{B}\nu})_l^{\mathrm{clear}} = (a_{1\nu})_l^{\mathrm{clear}}\,(S_{\mathrm{T}\nu})_l^{\mathrm{clear}} \tag{1.58}$$

$$(S_{\mathrm{B}\nu})_l^{\mathrm{cloudy}} = (a_{1\nu})_l^{\mathrm{cloudy}}(S_{\mathrm{T}\nu})_l^{\mathrm{cloudy}} \tag{1.59}$$

On the layer interfaces, it must be redistributed in the same way as downward diffuse flux, i.e. using the weights from equation (1.48).

Approximations dealing with spatial and angular integrations of the radiative transfer equation lead to the final delta-two-stream and adding system, represented by equations (1.46)–(1.49) and closed by the boundary conditions (1.51)–(1.54). Solution of the system involves inversion of matrix $8L \times 8L$ with 11 non-zero diagonals. Thanks to this, computational cost of the solver is *linear* in the number of layers L.

1.3   Spectral integration

So far, the delta-two-stream and adding system was formulated for the *monochromatic* radiation. In order to get the total energy budget driving temperature evolution, integration over relevant part of the spectrum must be carried on. It would be trivial if the world was grey, having the optical properties spectrally flat. This is not the case in the Earth's atmosphere, where the major complication comes from the gaseous absorption spectra. These are very complex, containing myriads of absorption lines having different strengths and half-widths, typically structured into the absorption bands separated by the weakly absorbing window regions. Absorption coefficient can vary very abruptly, falling many orders of magnitude as one moves from the center of a strong line to the nearby wing

region. Even worse, dependence of absorption coefficient on pressure and temperature complicates the treatment of non-homogeneous optical paths. And the atmosphere *is* non-homogeneous.

a) Line-by-line approach

The radiative transfer equation (1.1) and its delta-two-stream approximation (1.20)–(1.21) treat the different frequencies ν *independently*. The most straightforward approach to spectral integration would be to solve the monochromatic radiative transfer repeatedly for a set of frequencies being dense enough to resolve the individual spectral lines. Resulting flux over spectral interval $\Delta\nu$ is then given by the integral

$$F = \int_{\Delta\nu} F_\nu \, \mathrm{d}\nu, \qquad (1.60)$$

evaluated using suitable quadrature rule. Such *line-by-line* approach is indeed used in order to construct very accurate reference solutions. Its cost, however, makes it completely unusable in the NWP environment, where the calculation of radiative transfer can take microseconds per model column, but not minutes or even hours. In order to make the radiative transfer calculations feasible, significant shortcuts in the treatment of spectral integration must be sought, facing the additional complications coming from the presence of stratification and scattering. As will be seen later, the main difficulty of the *parameterized* radiative transfer comes from the interaction of spectral integration with spatial and angular ones.

Main techniques addressing an efficient spectral integration are the *band approach* and the *correlated k-distribution method*. They are briefly outlined in subsections b) and c).

b) Band approach

The idea behind band approach is to find such transmissions and reflectivities, with which the single solving of the delta-two-stream and adding system will give fluxes reasonably close or identical to the spectrally integrated reference results. In other words, the problem with spectrally varying optical properties is replaced by the *grey* problem, where the optical properties are spectrally flat. The mean difficulty lies in the parameterization of the band optical properties, which must take into account the non-local phenomenon of *optical saturation*. When the assumed spectral band is sufficiently wide, additional complications arise from the *spectrally correlated* optical properties of various radiatively active components, as well as from the non-negligible variation of Planck function (for more details see section 2.3 of Geleyn et al. [2017]).

In an idealized case with the single source and no scattering, the grey system *equivalent* to the original one exists, enabling to evaluate band absorption coefficient. Here it will be demonstrated in the simplest case, where the collimated beam with incident spectral flux F_ν undergoes a homogeneous path with absorber amount u. Transmitted flux integrated over spectral interval $\Delta\nu$ then reads:

$$\int_{\Delta\nu} F_\nu \exp(-k_\nu^{\mathrm{abs}} u) \, \mathrm{d}\nu \equiv \exp(-k^{\mathrm{abs}} u) \int_{\Delta\nu} F_\nu \, \mathrm{d}\nu \qquad (1.61)$$

Equation (1.61) can be inverted to express band absorption coefficient k^{abs} as

$$k^{\mathrm{abs}} = -\frac{1}{u} \ln \int_{\Delta\nu} \exp(-k_\nu^{\mathrm{abs}} u) w_\nu \, \mathrm{d}\nu$$

$$= \bar{k}^{\mathrm{abs}} - \frac{1}{u} \ln \int_{\Delta\nu} \exp[-(k_\nu^{\mathrm{abs}} - \bar{k}^{\mathrm{abs}})u] w_\nu \, \mathrm{d}\nu, \quad (1.62)$$

where w_ν is the spectral weight proportional to the incident spectral flux F_ν, meeting the normalization condition

$$\int_{\Delta\nu} w_\nu \, \mathrm{d}\nu = 1, \tag{1.63}$$

and $\bar{k}^{\mathrm{abs}}$ is the linear average of absorption coefficient k_ν^{abs}:

$$\bar{k}^{\mathrm{abs}} = \int_{\Delta\nu} k_\nu^{\mathrm{abs}} w_\nu \, \mathrm{d}\nu \tag{1.64}$$

Band absorption coefficient (1.62) generally depends on absorber amount u. This dependence cancels out in a grey case $k_\nu^{\mathrm{abs}} = \bar{k}^{\mathrm{abs}}$, which is trivial, or for absorber amount u so small that $|k_\nu^{\mathrm{abs}} - \bar{k}^{\mathrm{abs}}|u \ll 1$ for each frequency ν. In the latter case, known as the *weak-line limit*, exponential at the second line of equation (1.62) can be linearized, yielding unit value of the integral. For bigger absorber amount u and positive spectral weights w_ν, equation (1.62) gives band absorption coefficient $k^{\mathrm{abs}} < \bar{k}^{\mathrm{abs}}$. This phenomenon, following from the convex shape of exponential function, is known as *optical saturation*. It has dramatic impact on the *strong-line limit*, where the growth of band optical depth $\delta \equiv k^{\mathrm{abs}} u$ is controlled by absorption in the far line wings, since in the vicinity of the line centres all radiation has already been absorbed. The lower limit for band absorption coefficient k^{abs} is its minimum $k_{\min}^{\mathrm{abs}}$ over given spectral interval. Growth of band optical depth δ with absorber amount u is thus restricted by the linear envelope:

$$k_{\min}^{\mathrm{abs}} u \leq \delta(u) \leq \bar{k}^{\mathrm{abs}} u \tag{1.65}$$

Equations (1.61) and (1.62) are valid also for slanted beam, provided that vertical absorber amount u is replaced by u/μ_0, where μ_0 is the cosine of beam zenith angle. In case of diffuse incident radiation, vertical absorber amount u must be multiplied by diffusivity factor U, taking into account lengthened mean path.

The aim of band models is to provide explicit formulas relating the band gaseous optical depth δ to the mean line parameters. In few idealized situations, these can be obtained analytically. Two important cases, suitable for the water vapour and other asymmetric-top molecules, assume randomly positioned Lorentz lines with either exponential (Goody [1952]), or exponential-tailed S^{-1} distribution of line strengths S (Malkmus [1967]). Lorentz profile is a good approximation for the impact line shape when the collision time is negligible.[7] It is

---

[7]This is true in the ultraviolet, visible and infrared regions. In the microwave region, however, asymmetric Van Vleck and Weisskopf [1945] profile must be used, ensuring zero limit of k_ν for $\nu \to 0$.

popular due to its simple analytical formulation

$$k_\nu^{\text{abs}} = \frac{S}{\pi} \cdot \frac{\alpha_\text{L}}{(\nu - \nu_0)^2 + \alpha_\text{L}^2} \tag{1.66}$$

$$\int_{-\infty}^{+\infty} k_\nu^{\text{abs}} \, \text{d}\nu = S,$$

where S is the line strength, α_L is the line-half width, and ν_0 is the position of line centre.

To get analytical formulations, further simplifications must be employed: N Lorentz lines having the same half-width α_L, distributed in the interval of width $\Delta\nu = Nd$, where the spectral weights are assumed constant. Finally, the limit $N \to \infty$ is made, keeping the constant mean line spacing d. It means that the results are strictly valid in the artificial spectral interval $(-\infty, +\infty)$. Nevertheless, they can be applied also in the finite spectral interval, provided its width $\Delta\nu$ is large enough to contain many lines, but small enough to assume their random positioning and to neglect variation of spectral weights. In order to suppress contribution of lines centred outside the finite spectral interval, width $\Delta\nu$ must be much larger than the line half-width α_L.[8]

The Malkmus band model is preferable to the Goody one, because it assumes more realistic distribution of weak lines. It provides very simple formula for band optical depth

$$\delta_{\text{malkmus}}(u) = \frac{\pi\alpha_\text{L}}{2d} \left(\sqrt{1 + \frac{4\bar{S}u}{\pi\alpha_\text{L}}} - 1 \right), \tag{1.67}$$

where $\bar{S}$ is the mean line strength. Application of the Malkmus formula (1.67) still requires replacement of the line half-width α_L with the mean value $\bar{\alpha}_\text{L}$, since in reality the band contains lines of different half-widths. Averaging formula for $\bar{\alpha}_\text{L}$ is most commonly obtained from the optically thick, non-overlapping limit. Warner and Ellingson [2000] explained that determining the band model parameters by matching the asymptotic limits is not optimal, since these are rarely reached in practice. They have obtained remarkably better accuracy by fitting the Malkmus formula directly against line-by-line results, using a relevant range of absorber amounts.[9] Residual error is then almost purely due to the band model assumptions.

Applicability of *random* band models is further restricted by the fact that for big absorber amount u they give band optical depth $\delta(u) \propto \sqrt{u}$, which at some point falls below linear envelope (1.65). Validity range of the square-root approximation is analyzed in section VIII.3 of Plass [1958], where it is shown that there is also *upper* limit on absorber amount u. Here it should be noted that the asymptotic behaviour violating lower constraint (1.65) is an artefact coming from limit $N \to \infty$ at constant line spacing d. This is because $2N$ spectral lines positioned randomly in interval of width $2Nd$ overlap more efficiently than N lines scattered in interval of width Nd. Bigger line overlap results in more transparent

---

[8]This ensures that spectral lines centred outside the assumed interval will affect absorption only near its boundaries, while deeper inside contribution of their far wings can be neglected.

[9]Such approach requires use of the non-linear least-squares fitting.

band alias lower band optical depth. Overlap effect acts only for bigger absorber amounts, so that the weak-line limit remains unaffected.

There is a simple possibility how to achieve the correct asymptotic behaviour of the random band model for big absorber amount u. It is sufficient to extend the band optical depth by the term $k_{\min}^{abs} u$, representing the background continuum absorption. At the same time, mean line strength $\bar{S}$ have to be replaced by $\bar{S} - k_{\min}^{abs} d$, in order to preserve the weak-line limit $\bar{S} u / d$. Figure 1.8, comparing the band approach with the k-distribution method, demonstrates beneficial impact of the continuum correction for the Goody band model.

Regardless of the way how the band model parameters were derived, their link to the mean line parameters $\bar{S}$ and $\bar{\alpha}_L$ is crucial for the treatment of the non-homogeneous optical paths. The problem is traditionally solved by the Curtis-Godson scaling approximation (Curtis [1952], Godson [1953]). It assumes a single Lorentz line absorbing along the non-homogeneous optical path, and constructs the homogeneous path yielding the same weak and strong-line limits. The procedure results in the path averaging rules

$$\langle S \rangle = \frac{1}{u} \int_0^u S(u) \, \mathrm{d}u \tag{1.68}$$

$$\langle \alpha_L \rangle = \frac{1}{\langle S \rangle u} \int_0^u \alpha_L(u) S(u) \, \mathrm{d}u, \tag{1.69}$$

where the absorber amount u is used as the vertical coordinate, and the vertical variation of the line parameters S and α_L follows from their pressure and temperature dependences.[10] The path averaging rules (1.68) and (1.69) are finally applied to the mean line parameters $\bar{S}$ and $\bar{\alpha}_L$, and the Malkmus formula (1.67) is evaluated.

As explained above, applicability of the Malkmus band model is restricted to the *narrow* spectral intervals[11], where its assumptions roughly hold. However, use of hundred or more such intervals would be prohibitive from the computational point of view. For this reason, band approach in the NWP models must be applied in much broader spectral intervals. This is only possible if the variation of spectral weights is taken into account, together with the non-random distribution of absorption lines on larger scales. Both effects can be included by an empirical correction of the Malkmus formula. Key element, necessary for the treatment of the non-homogeneous optical paths, is keeping the Malkmus core and applying the additional corrections that are small. Like this, link of the fundamental band model parameters to the mean line parameters is preserved. Yet another complication arises from the fact that on larger scales, spectral transmissions of different gases can be correlated, resulting in non-additivity of their broadband optical depths. Spectral correlations can appear also between various radiatively active species. They must be parameterized whenever found significant, resulting in the broadband scheme resembling Matryoshka. Still, Mašek et al. [2016] and Geleyn et al. [2017] proved that such approach is feasible, guaranteeing sufficient accuracy of the ACRANEB2 scheme even with the single shortwave and single longwave spectral intervals. Moreover, the broad spectral intervals make

---

[10]The line strength S depends on temperature, while the Lorentzian line half-width α_L depends also on pressure (via the frequency of molecular collisions).

[11]Spectral interval can be assumed narrow, when it has $\Delta \nu / \nu \lesssim 0.01$.

the cost of the full cloud-radiation interaction feasible, via the use of selective intermittency described in section 2.7.

Application of the band approach to aerosols and clouds is straightforward in the narrow spectral intervals, where they can be safely treated as the grey bodies. This is because their optical properties are much smoother than gaseous absorption. Grey treatment of aerosols is justified also in the broad spectral intervals, provided their optical depth is small, so that linear averaging can be applied. Situation for clouds is different. Mašek et al. [2016] showed that in the full shortwave spectrum, optical saturation of cloud absorption must be parameterized, taking scattering into account. On the other hand, Geleyn et al. [2017] proved that in the full longwave spectrum, grey treatment of clouds is justified.

Phenomenon of optical saturation is caused by the changing spectral composition of radiation passing through the atmosphere. The band approach parameterizes this effect without going to spectrally detailed calculations. The main complication in doing so is the presence of scattering, altering the optical paths in a non-trivial way. Possible solution for gaseous absorption and Rayleigh scattering is to evaluate optical saturation along the *idealized optical paths*, described in section 2.5 of Mašek et al. [2016], and in sections 6.3 and 6.4 of Geleyn et al. [2017]. These provide accurate results in the important limit cases dominated by gases. In the situations dominated by clouds, shortwave cloud optical saturation must be evaluated by the more sophisticated method introduced in section 6.3 of Mašek et al. [2016], taking multiple scattering into account. Here the idealized optical paths become less relevant, but their use for gaseous optical saturation still gives reasonable results. This is because cruder approximations can be afforded for the less influential processes (gaseous absorption and scattering in this case).

c) Correlated k-distribution method

There are three main limitations of the band approach – simplifying assumptions on the distribution of line strengths and positions, necessity to use the scaling approximation when treating non-homogeneous optical paths, and evaluation of the optical saturation in scattering environment. The first limitation can be avoided elegantly by the so-called *k*-distribution method, for the *homogeneous* atmosphere introduced to meteorology by Arking and Grossman [1972]. The idea is simple. In a sufficiently narrow spectral interval, such that variation of spectral weights can be neglected, the band transmission is given by spectral integral that can be transformed into integral over *k*-values:

$$\tau \equiv \frac{1}{\Delta\nu} \int_{\Delta\nu} \exp(-k_\nu^{\text{abs}} u)\,\mathrm{d}\nu = \int_0^\infty \exp(-ku) g'(k)\,\mathrm{d}k$$
$$= \int_0^1 \exp[-k(g)u]\,\mathrm{d}g \approx \sum_i \exp[-k(g_i)u]\,\Delta g_i \quad (1.70)$$

Function $g(k)$ gives the proportion of spectral interval $\Delta\nu$ where the absorption coefficient $k_\nu^{\text{abs}} < k$. In other words, $g(k)$ is the cumulative probability function of k-values, and its derivative $g'(k)$ is the corresponding probability density function. The last step, changing integration in k-space to integration in g-space,
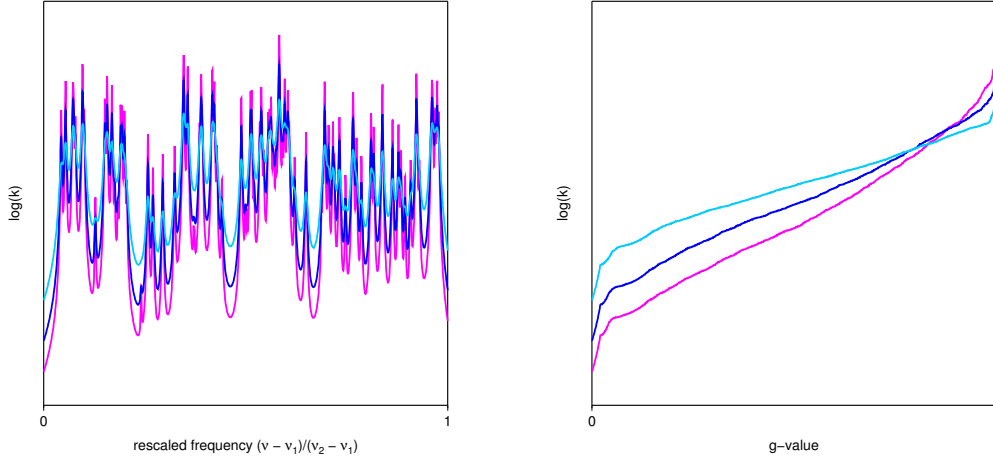
Figure 1.7: The synthetic absorption spectrum consisting of 100 randomly placed Lorentz lines with exponential distribution of line strengths, plotted for three line half-width to mean line spacing ratios α_{L}/d: magenta – 0.1; dark blue – 0.2; blue – 0.5. Horizontal sampling uses 2000 regular intervals. **Left:** Original spectrum. **Right:** Reordered spectrum.

introduces $k(g)$ as the inverse function of $g(k)$.[12]

The last integral in equation (1.70) can be approximated by the sum, using quadrature points g_i and weights Δg_i, where the latter sum up to one:

$$\sum_i \Delta g_i = 1 \tag{1.71}$$

Equation (1.70) thus approximates the band transmission by the weighted sum of decaying exponentials, providing the band optical depth:

$$\delta(u) = -\ln\left\{\sum_i \exp[-k(g_i)u]\,\Delta g_i\right\} \tag{1.72}$$

For the given choice of quadrature points and weights, values $k(g_i)$ must be calculated from underlying spectroscopic data, and this calculation must be done for the set of temperatures and pressures. In practice it is sufficient to use $\lesssim 10$ quadrature points for a gas, which is enormous compression of information, given the fact that dependence of the gaseous absorption coefficient k_ν^{abs} on frequency ν is very complicated, containing thousands of spectral lines. By the reordering of k_ν^{abs} values, much smoother and monotonically increasing function $k(g)$ is obtained, still containing full information necessary for determining the band transmission, including the effects of line shape, spacing, overlap and intensity distribution. Figure 1.7 illustrates reordering for the synthetic spectrum consisting of 100 Lorentz lines. From the shape of $\log(k)$ versus g curves it follows that g-points should be clustered around 0 and 1, where the slope is steepest.

It is instructive to compare the curves of growth for different methods of spectral integration. Figure 1.8 does this for a homogeneous case, using the same

---

[12]Mathematically, going from the frequency integration to the integration over g-values corresponds to the move from Riemann to Lebesgue integral.
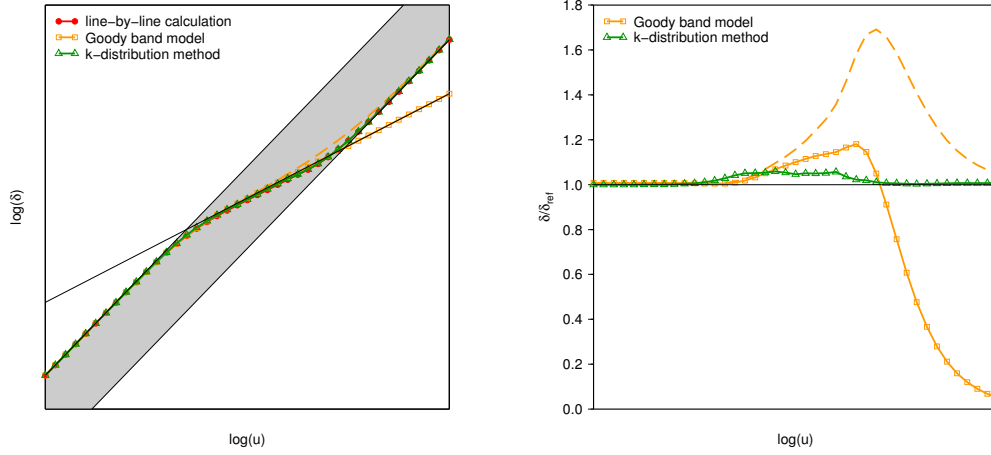
Figure 1.8: The band optical depth $\delta(u)$ of magenta spectrum on figure 1.7: red dots – the reference line-by-line calculation (spectral sampling with 2000 regular intervals); yellow squares – the Goody band model (2 parameters); yellow dashed line – the Goody band model extended by continuum term (3 parameters); green triangles – the k-distribution method (10 g-intervals 0–0.001–0.005–0.02–0.2–0.5–0.8–0.98–0.995–0.999–1). **Left:** The curves of growth alias $\log(\delta)$ versus $\log(u)$. Straight lines denote slopes of linear and square-root regions, with $\delta(u) \propto u$ and $\delta(u) \propto \sqrt{u}$ respectively. Grey shade is the linear envelope (1.65). **Right:** Ratios $\delta/\delta_{\text{ref}}$ versus $\log(u)$.

synthetic spectrum as on figure 1.7, having ratio $\alpha_{\text{L}}/d = 0.1$. Underlying distribution of spectral lines meets assumptions of the Goody [1952] band model. Red curve shows results of the line-by-line calculation performed for 2000 frequencies, and it serves as the reference. Yellow curve is the Goody band model, which has only two independent parameters related to the mean line intensity, half-width and spacing. It can be seen that for small absorber amounts it is very close to the reference, and even for intermediate ones the error remains within 20%. For large absorber amounts, however, its applicability limit is broken. This is because it continues to follow the square-root growth also when the continuum background starts to dominate the reference solution, bringing it back to linear growth. The correct asymptotic behaviour for big absorber amounts can nevertheless be restored by incorporating the continuum term, as was discussed in subsection b). This possibility is indicated by yellow dashed curve, which captures the continuum dominated region, but it suffers from considerable overestimation between intermediate and large absorber amounts. Green curve is the k-distribution method with 10 g-intervals. It is able to follow the reference closely, with the error staying within 5% in the full range of absorber amounts. Additional advantage of the k-distribution method is its applicability for *any* line distribution and *arbitrary* line shape.

Thanks to the limited width of spectral interval $\Delta\nu$, necessary for neglecting the variation of spectral weights, it can be assumed that band transmissions of gases 1 and 2 are multiplicative. Application of the k-distribution method than

30

gives the band transmission of the mixture as

$$\tau_{12} = \tau_1 \tau_2 = \sum_i \exp[-k_1(g_i)u_1] \, \Delta g_i \sum_j \exp[-k_2(g_j)u_2] \, \Delta g_j$$

$$= \sum_{i,j} \exp[-k_1(g_i)u_1 - k_2(g_j)u_2] \, \Delta g_i \Delta g_j = \sum_{i,j} \exp[-k_{ij}(q)u] \, \Delta g_i \Delta g_j, \quad (1.73)$$

where the following notations were introduced:

$$u \equiv u_1 + u_2 \tag{1.74}$$

$$q \equiv \frac{u_2}{u_1 + u_2} \tag{1.75}$$

$$k_{ij}(q) \equiv (1 - q)k_1(g_i) + q k_2(g_j) \tag{1.76}$$

Equation (1.73) enables to get the k-distribution of the mixture from the k-distributions of its individual components. The only annoying fact is that the number of k-values alias g-points increases from N to N^2, because of the double sum in equation (1.73). Lacis and Oinas [1991] prevented the added computational burden by ordering the values of $k_{ij}(q)$, and then reblocking them back to N intervals. Fu and Liou [1992] developed an alternative approach, making the k-distribution dependent also on mixture composition q. It means that k-values in each g-interval have to be determined and tabulated not only for the range of pressures and temperatures, but also for the desired set of mixture compositions. By the careful choice of spectral intervals it can be achieved that there are no more than two dominant absorbing gases in each.[13]

The k-distribution method can deal also with the *non-homogeneous* atmosphere. Here the *correlated assumption* comes to play, introduced rigorously by Fu and Liou [1992]. The band transmission along the non-homogeneous optical path is given by double integral

$$\tau = \frac{1}{\Delta \nu} \int_{\Delta \nu} \exp\left[-\int_{\Delta z} k_\nu^{\mathrm{abs}}(p(z), T(z))\rho(z) \, \mathrm{d}z\right] \mathrm{d}\nu, \tag{1.77}$$

where the absorption coefficient k_ν^{abs} varies in vertical via its pressure and temperature dependences, and $\rho(z)$ is the density profile of absorbing gas, so that $\rho(z)\,\mathrm{d}z$ is the increment of absorber amount. In the k-distribution method, however, it is desirable to express the band transmission as:

$$\tau = \int_0^1 \exp\left[-\int_{\Delta z} k(g, p(z), T(z))\rho(z) \, \mathrm{d}z\right] \mathrm{d}g \tag{1.78}$$

Equation (1.78) is equivalent to (1.77), provided that ordering of k-values at each point of the optical path is the same. In other words, g-value associated with given frequency ν should be pressure and temperature independent:

$$g(k_\nu(p, T), p, T) = h(\nu) \tag{1.79}$$

Constraint (1.79) is the so-called correlated assumption, with h being arbitrary function of frequency ν only. It holds exactly e.g. for an isolated Lorentz

---

[13]The band approach is more advantageous in this respect, since it can apply multiplicativity of the band transmissions directly, without restricting the number of absorbing gases.
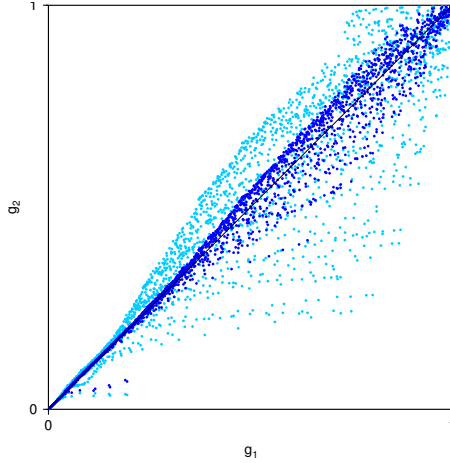
Figure 1.9: Scatterplot showing correlation of g-values at different pressures p_1 and p_2: dark blue – $p_2/p_1 = 2$; blue – $p_2/p_1 = 5$. Data points are obtained from the synthetic spectra shown on figure 1.7, using spectral sampling with 2000 regular intervals. On horizontal axis there are g-values of magenta spectrum with $\alpha_L/d = 0.1$, while on vertical axis there are corresponding g-values of dark blue and blue spectra with $\alpha_L/d = 0.2$ and 0.5 respectively. Proportionality of Lorentz line-half width α_L to pressure is exploited.

line, or when the line overlaps can be neglected. This is not the case in the atmosphere, where the correlation of g-values is disturbed by vertical variation of pressure, temperature, and also gaseous composition. All these effects result in *blurring* of g-values, for pressure variation alone illustrated on figure 1.9. It can be seen that even for pressure ratio 5, representing the vertical variation across the troposphere, correlation of g-values for a single gas is considerable. Realism of the correlated assumption comes from the fact that the line positions are independent of pressure and temperature. So even if the line strengths and half-widths change, regions of high and low absorption remain the same.

Full strength of the correlated k-distribution method becomes apparent when it is applied in the scattering environment. Involved spectral intervals are sufficiently narrow to assume Rayleigh scattering, aerosols, clouds and the Earth's surface as grey bodies in each. In the presence of scattering, k-distribution method never evaluates the band transmissions according to equation (1.70). Instead, it performs radiative transfer calculations in each g-interval, where the gaseous absorption can be assumed *quasi-monochromatic*. As a consequence, the optical saturation becomes a *resolved* phenomenon, and its interaction with scattering does not have to be addressed. At the very end, fluxes from each g-interval are summed up to get final flux for given spectral interval. This is enormous simplification of the scattering problem, faced in the broadband schemes. The main accuracy limitation, that cannot be escaped, is the correlated assumption.

The price paid for reordering of k-values is the need to solve the radiative transfer equation many times. In the widely used RRTMG (Rapid Radiative Transfer Model, optimized for use in GCMs) scheme of Iacono et al. [2008], there are 14 shortwave intervals with the total of 112 g-points, plus 16 longwave intervals with the total of 140 g-points. Altogether, radiative transfer equation

have to be solved 252 times in order to get broadband fluxes. On the contrary, ACRANEB2 scheme needs only nine solvings of the delta-two-stream and adding system – one shortwave and eight longwave, the latter because of the NER decomposition with bracketing.

Computational cost of the RRTMG scheme is still too high for the NWP models, where it is typically used with reduced spatial and/or temporal resolutions. This is still the mainstream approach, despite the serious *structural deficiency* compromising an outstanding accuracy of the correlated k-distribution method by infrequent calls of the radiation scheme, unable to exploit the available high resolution information. The problem is inspected in section 2.7, describing an interesting alternative offered by the ACRANEB2 scheme. Efforts are ongoing also on the RRTMG side. If the cost of the correlated k-distribution method was further reduced, the scheme could be called more frequently in space and/or time. Recent line of attack aims at developing the FSCK (Full-Spectrum Correlated-k) method, extending applicability of the reordering idea to wide spectral intervals. The ambition is to reduce the number of necessary g-points and of related quasi-monochromatic solvings of the radiative transfer equation, without significant deterioration of accuracy. Works of Pawlak et al. [2004] and Hogan [2010] explore this possibility in the shortwave and longwave spectra respectively, addressing *some* of the associated problems.

d) Basic spectral split

Many NWP radiative transfer codes are greatly simplified by the fact that emission spectra of the Sun and Earth practically do not overlap[14], since their temperatures are very different (5770 K versus 200 to 300 K). Thanks to this, relevant part of the electromagnetic spectrum spanning from the ultraviolet to far-infrared regions, can be split to disjoint *solar* and *thermal* bands.[15] In the solar band (shortwave spectrum), Earth's atmosphere and surface do not emit, and the only source of diffuse radiation is the scattering of direct solar beam. In the thermal band (longwave spectrum), there is no direct solar beam, so that the only source of diffuse radiation is the emission by the Earth's atmosphere and surface. As long as the overlap between solar and terrestrial spectra is neglected, the source term contains either the scattering of direct solar beam or the terrestrial emission, but not both.

1.4 General outline of the radiative transfer scheme

Aim of radiative transfer parameterization in the NWP model is to provide shortwave and longwave radiative fluxes at all layer interfaces of each model column, including the TOA and the Earth's surface. Inputs to radiation scheme are 3D

---

[14]They overlap for wavelengths from 3 to 5 μm, but this region is insignificant for atmospheric energy budget, being on the tail of both solar and terrestrial emission spectra. Solar-terrestrial overlap has to be taken into account by the remote sensing applications working at these wavelengths.

[15]In case of the ACRANEB2 scheme, wavelengths from 0.245 to 105 μm are covered, with the boundary between solar and thermal bands placed at 4.642 μm.

fields describing thermodynamic state and composition of the atmosphere (temperature, pressure, specific humidity, concentrations of ozone and greenhouse gases, aerosol load, cloud fraction, liquid and ice cloud condensates), 2D fields specifying surface properties (direct and diffuse albedos, emissivity and temperature), and astronomical parameters (incoming solar radiation at the TOA and actual sun elevation in each model column). For more advanced schemes, additional information may be needed. Surface albedos, emissivity and incoming solar radiation at the TOA must be specified in the spectral division used by the radiation scheme.

Having all necessary inputs, radiative transfer is calculated in two steps. In the first step, radiation scheme evaluates transmissions and reflectivities of model layers, combining the contributions of radiatively active gases, aerosols and clouds. Optical properties are calculated separately for clearsky and cloudy parts of the layers. In the second step, approximated radiative transfer equation with corresponding boundary conditions is solved in each spectral band, delivering fluxes at layer interfaces. For shortwave fluxes, distinction between direct and diffuse components is kept.

For evaluating radiative energy budget only the net fluxes F integrated over whole spectrum are of interest, but from the implementation point of view as well as for applications and verification it is advantageous to keep the fluxes split into shortwave and longwave parts. At the TOA and at the surface, the net fluxes are complemented by the upward and downward fluxes $F^\uparrow$ and $F^\downarrow$, following from boundary conditions.

In the NWP model, sum of the shortwave and longwave net radiative fluxes contributes to the total energy budget, determining evolution of the temperature field. If the radiative transfer was the only assumed process, atmospheric heating rate at pressure level p would be given by the vertical divergence of the net flux

$$\frac{\partial T}{\partial t} = -\frac{a_{\mathrm{g}}}{c_{\mathrm{p}}} \cdot \frac{\partial F}{\partial p} \tag{1.80}$$

$$F \equiv F^\downarrow - F^\uparrow, \tag{1.81}$$

where T is temperature, t is time, a_{g} is gravity acceleration and c_{p} is specific heat of air at constant pressure. Convention (1.81) defines the net flux F as positive when the downward energy transfer prevails. Equation 1.80 evaluated separately for shortwave and longwave net fluxes is an important indicator of radiative heating or cooling.

2. Key improvements leading to the ACRANEB2 scheme

As was mentioned in the introduction, this chapter presents the most important author's contributions leading to the ACRANEB2 scheme. Four components are described: broadband gaseous transmissions (sections 2.1–2.4), shortwave cloud optical saturation (section 2.5), bracketing technique for internal longwave atmospheric exchanges (section 2.6), and intermittent update of gaseous transmissions and bracketing weights (section 2.7). First three components improve accuracy of the ACRANEB2 scheme in a stand-alone mode, while the last component reduces the computational cost and ensures reasonable error balance in the NWP environment, keeping the full cloud-radiation interaction. All results presented in this chapter were obtained without aerosols, so that meaning of *clearsky* conditions is restricted to situations with atmospheric gases only.[1] Aerosols were not addressed in this thesis mostly because of their grey treatment in the ACRANEB2 scheme, uninteresting from the spectral integration point of view. Anyway, omission of aerosols should not affect relevance of the obtained results.

2.1 Broadband corrected Malkmus formula

First task of the band approach is to deliver band optical depth $\delta(u, p, T)$ of a considered gas along the homogeneous optical path with the absorber amount u, pressure p and temperature T. This is achieved by fitting desired functional dependence against the reference detailed in section 3.1 of Mašek et al. [2016], using the minimization procedure described in section 3.5 therein. In the solar band, reference gaseous transmissions are averaged by the solar spectrum at the TOA, where the idealized optical paths start. In the thermal band, transmissions averaged with the Planck weights at temperature of the emitting body are needed, as explained in section 3.1 of Geleyn et al. [2017].

The Malkmus formula (1.67) cannot be applied in broad spectral intervals, where the underlying assumptions are not met. Additional corrections are thus needed. First of all, these should take into account *secondary saturation*, leading to the slower than $\sqrt{u}$ strong-line growth of band optical depth $\delta(u)$. They should also improve accuracy of $\delta(u, p, T)$ fits by including peculiarities coming e.g. from continuum absorption.

An uncorrected broadband Malkmus formula can be written in the shape

$$\delta_{\text{malkmus}}(u, p, T) = \frac{a(T)}{2b(p, T)} \cdot \left[\sqrt{1 + 4b(p, T)u} - 1 \right] \tag{2.1}$$

$$a(T) = a_0 \cdot \frac{1 + a_1 T}{1 + a_2 T} \qquad b(p, T) = \frac{b_0}{p} \cdot \frac{1 + b_1 T}{1 + b_2 T}$$

$$a_0, b_0 > 0 \qquad a_1, a_2, b_1, b_2 \geq 0,$$

containing 6 fitting parameters a_0, a_1, a_2, b_0, b_1 and b_2. Independence of coefficient $a(T)$ on pressure and proportionality of coefficient $b(p, T)$ to $1/p$ are

---

[1] In the literature, conditions without clouds and aerosols are sometimes called *pristine*, while the term *clearsky* is reserved for those without clouds.

adopted from the narrowband case[2], while their temperature dependences are fitted by simple hyperbolic formulas, ensuring positive results. The broadband formula (2.1) retains weak-line limit independent of pressure alias line shape. In the strong-line limit, pressure still enters only via product pu. Secondary saturation, following from the non-linear averaging of many narrowband Malkmus formulas, is then parameterized by the rescaling

$$\delta_{\mathrm{I}}(u,p,T) = \frac{\delta_{\mathrm{crit}}}{\alpha} \left\{ \left[1 + \frac{\delta_{\mathrm{malkmus}}(u,p,T)}{\delta_{\mathrm{crit}}} \right]^{\alpha} - 1 \right\} \quad (2.2)$$
$$0 < \alpha < 1 \qquad \delta_{\mathrm{crit}} > 0,$$

which introduces two new fitting parameters α and δ_{crit}, ensuring the $u^{\frac{\alpha}{2}}$ strong-line growth of band optical depth $\delta_{\mathrm{I}}(u)$. The rescaling (2.2) is designed in such way that it starts to act for optical depths $\delta_{\mathrm{malkmus}} \sim \delta_{\mathrm{crit}}$, not affecting the weak-line limit.

Correction (2.2) makes the Malkmus formula usable in the full solar and thermal bands. Further improvement, needed to get sufficiently accurate heating rates, can be achieved by the temperature and pressure dependent secondary corrective fits

$$\delta_{\mathrm{aux}}(u,p,T) = \delta_{\mathrm{I}}(u,p,T)$$
$$\times \left[P_{00}(T) + \frac{\delta_{\mathrm{I}}(u,p,T)}{\delta_{\mathrm{I}}(u,p,T) + D} \sum_{j=0}^{5} P_j(T) \cdot \ln^j \delta_{\mathrm{I}}(u,p,T) \right]_{+} \quad (2.3)$$

$$\delta_{\mathrm{II}}(u,p,T) = \delta_{\mathrm{aux}}(u,p,T) \left[1 + \frac{Q(p)}{1 + \delta_{\mathrm{aux}}(u,p,T)} \right]_{+}, \quad (2.4)$$

bringing additional 25 fitting parameters: scalar $D > 0$, second order polynomials $P_{00}(T)$, $P_0(T)$, ..., $P_5(T)$, and second order polynomial $Q(p)$. Shape of the corrective fits (2.3)–(2.4) was motivated by the error behaviour of band optical depth $\delta_{\mathrm{I}}(u,p,T)$, with some simplifications done in order to achieve computationally cheap formulas. Equations (2.3)–(2.4) do not guarantee non-negative results. For safety, eventual negative values are truncated to zero, as indicated by subscript '+'.

Accuracy of the homogeneous solar fits for the water vapour and ozone is demonstrated on figure 2.1. Individual panels show contours in the (p,T) plane of the error function

$$\varepsilon(p,T) = \sqrt{ \frac{1}{K} \sum_{k=1}^{K} \ln^2 \frac{\delta(u_k,p,T)}{\delta_{\mathrm{ref}}(u_k,p,T)} }, \quad (2.5)$$

where the sum goes through 33 absorber amounts used in the fitting procedure. The reason for choosing the root-mean-square error of $\ln \delta$ is the considerable variation of band optical depth δ in the region of interest, spanning many orders of magnitude. The error function (2.5) is consistent with the least-squares fitting procedure, which minimizes the sum of $\varepsilon^2(p,T)$ over 15 values of pressure and

---

[2]In the narrowband case there is $a(T) = \bar{S}(T)/d$ and $b(p,T) = \bar{S}(T)/[\pi \bar{\alpha}_{\mathrm{L}}(p,T)]$, with $\bar{\alpha}_{\mathrm{L}}(p,T) \propto p$.

5 values of temperature.[3] Error of the uncorrected Malkmus formula (2.1) (top row) is definitely too large to be used in the full solar band. Reasonable values of the error function (2.5) are below 0.1, indicated by the shades of grey, meaning the average relative error of band optical depth δ up to $\sim$10%. The rescaling (2.2) improves the accuracy dramatically (middle row), reducing the maximum error below 0.15. The error distribution across the (p, T) plane becomes smoother, especially for ozone. Finally, the secondary corrective fits (2.3)–(2.4) (bottom row) reduce the error slightly for water vapour, pushing it below 0.1 except for insignificant low pressure region.[4] In case of ozone, they lead to almost perfect fit, with the maximum error deeply below 0.01. It should be stressed that the fitting of band optical depth $\delta_{\mathrm{II}}(u, p, T)$ was not done in steps, but simultaneously for all 33 fitting parameters occurring in formulas (2.1)–(2.4). Globally optimal results are thus ensured.

Accuracy of the fits with respect to absorber amount u can be inspected on figure 2.2, showing reference and fitted $\delta(u)$ curves for two meteorologically important error-prone regions, represented by the lower left and upper right corners of the error maps on figure 2.1. For convenience, the absorber amount u is expressed in pressure units, obtained by multiplying the value in $\mathrm{kg\,m^{-2}}$ by standard gravity acceleration $a_{\mathrm{g}} = 9.80665\,\mathrm{m\,s^{-2}}$. It is now obvious why the uncorrected Malkmus formula with $\sqrt{u}$ strong-line growth cannot capture the reference band optical depth well. Addition of the rescaling (2.2) restores correct strong-line growth for the water vapour (top row), leaving little space for further improvement. Situation is more complicated for ozone (bottom row), where for big absorber amounts u the $\delta(u)$ growth increases again. This can be attributed to a strong ozone continuum absorption in the solar wavelengths, which starts to dominate once the absorption near the line centres becomes depleted. This effect cannot be described by the simple rescaling (2.2), on the other hand the secondary corrective fits (2.3)–(2.4) include it very accurately.

Evaluation of band optical depth along the non-homogeneous optical path is done via the Curtis-Godson approximation (1.68)–(1.69) translated to coefficients $a(T)$ and $b(p, T)$, complemented by explicit averaging rules for pressure and temperature required by the secondary corrective fits (2.3)–(2.4) (for details see section 3.6 of Mašek et al. [2016]). Since the monotonicity of resulting band optical depth $\delta(u)$ is not assured, incremental gaseous optical depth must be safely evaluated as

$$\Delta\delta = [\delta(u + \Delta u) - \delta(u)]_{+}, \qquad (2.6)$$

where again subscript '+' denotes truncation of negative values to zero. Nevertheless, the ill behaved cases, where this truncation takes part, are rare within the fitting ranges of absorber amount, pressure and temperature. In principle, one could use explicitly averaged pressure and temperature also for evaluating Malkmus coefficients $a(T)$ and $b(p, T)$ along the non-homogeneous optical path. Such approach, however, would give less accurate results than the Curtis-Godson approximation.

---

[3]Fitting range is 5–1000 hPa for pressure, and 204.0–307.6 K for temperature. Fitting range of the absorber amount is chosen individually for each gas, so that it covers both the weak-line limit and the maximum value likely to be encountered in the scattering atmosphere.

[4]Low pressure region is insignificant for water vapour, due to its negligible stratospheric abundances, but not for ozone.
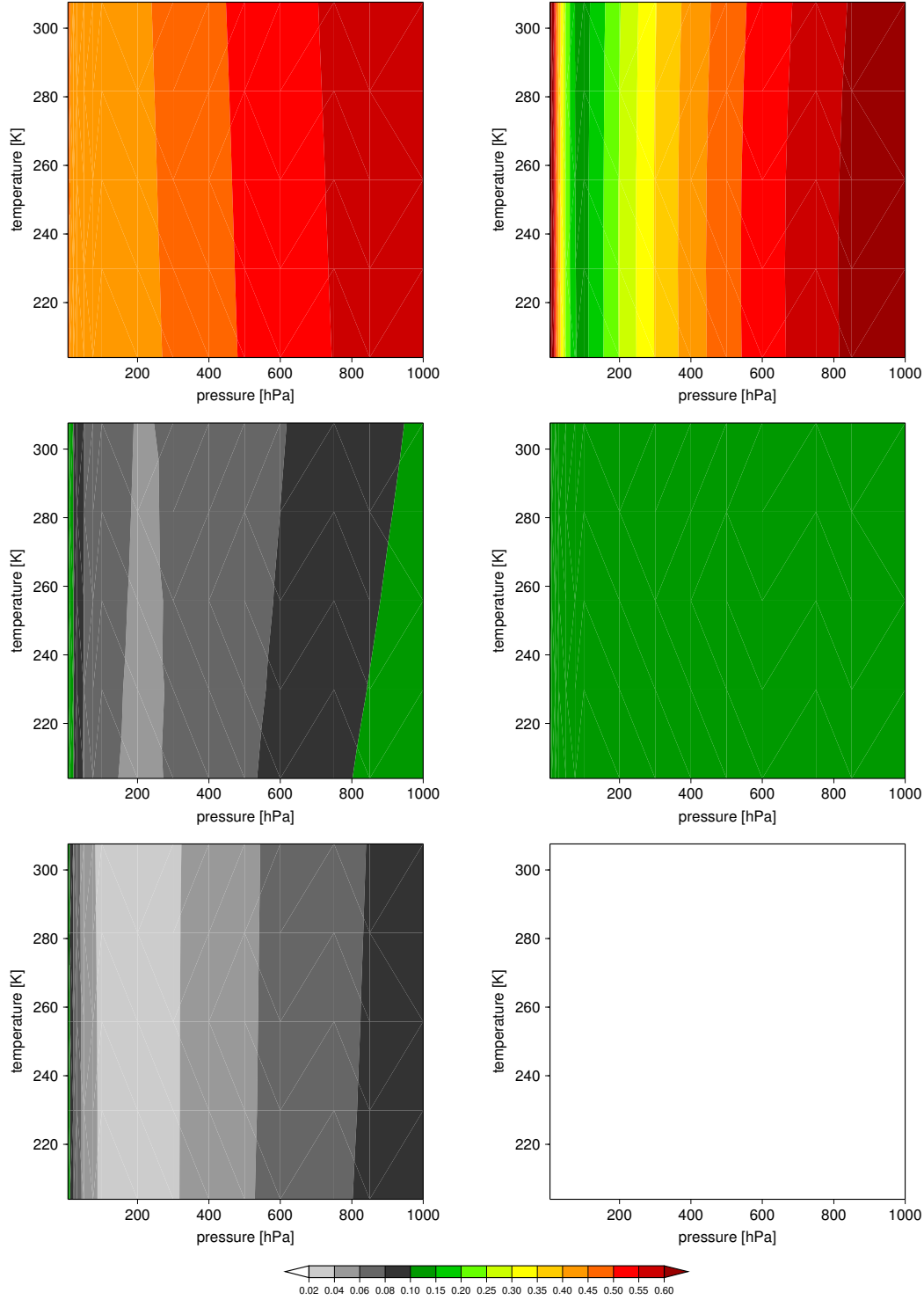
Figure 2.1: Error of the Malkmus formula, applied in the full solar spectrum, with respect to the narrowband reference. For each pressure and temperature, error over relevant range of absorber amounts is evaluated using equation (2.5). **Left:** Error maps for water vapour. **Right:** Error maps for ozone. **Top:** The uncorrected Malkmus formula. **Middle:** The Malkmus formula with the broadband correction I. **Bottom:** The Malkmus formula with the broadband corrections I and II.
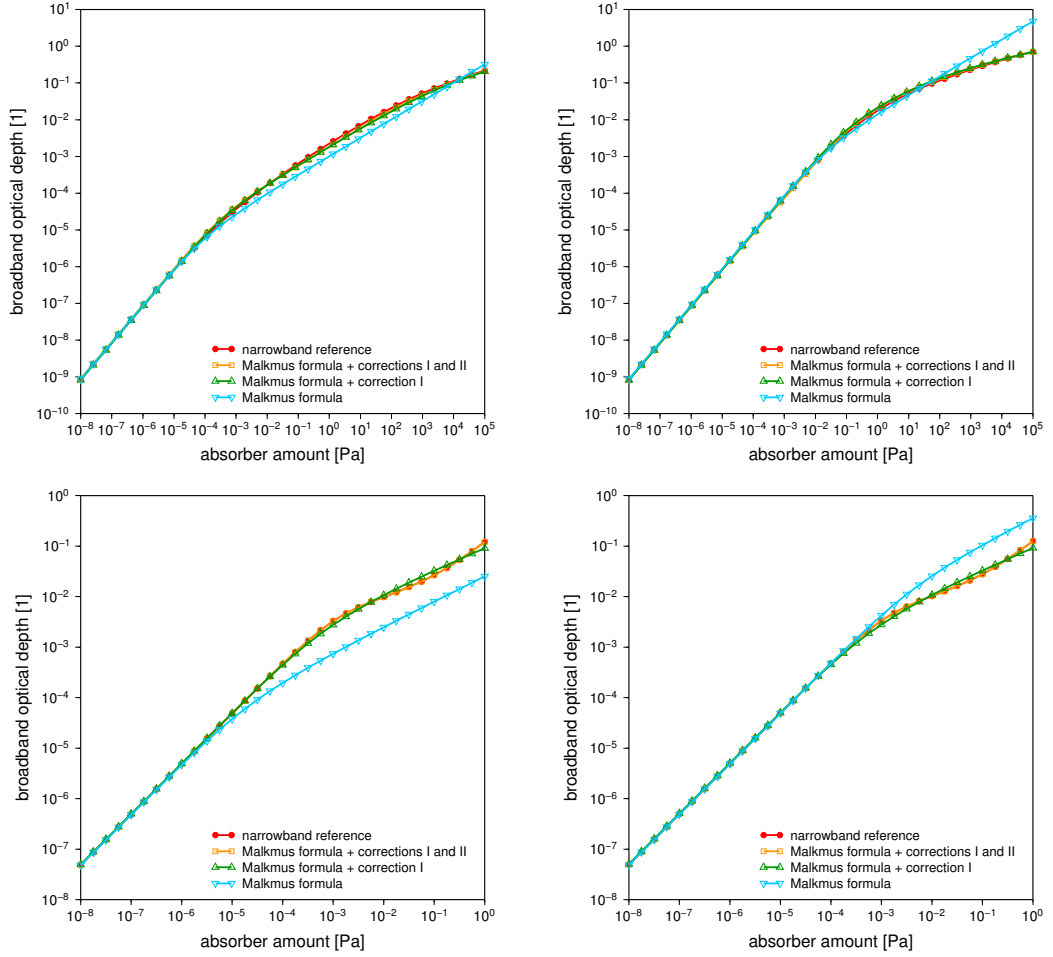
Figure 2.2: Dependence of band optical depth in the full solar spectrum, given by different versions of the Malkmus formula, on the absorber amount. The narrowband reference is plotted in red. **Top:** Water vapour. **Bottom:** Ozone. **Left:** Low pressure and temperature ($p = 5\,\mathrm{hPa}$, $T = 204.0\,\mathrm{K}$). **Right:** High pressure and temperature ($p = 1000\,\mathrm{hPa}$, $T = 307.6\,\mathrm{K}$).

It must be admitted that while the rescaling (2.2) is conceptually simple, dealing with secondary saturation by introducing only two extra fitting parameters, the secondary corrective fits (2.3)–(2.4) go against this simplicity. They cannot be avoided when the high accuracy of heating rates is required (see figure 2 of Mašek et al. [2016]).

2.2   Double temperature dependence of the longwave gaseous transmissions

Broadband approach in the thermal spectrum brings an additional complication related to emission: band transmission τ depends not only on path temperature T, via the line strengths and line half-widths, but also on temperature of the emitting body T_e, via the Planck weights $w_\nu(T_e)$ whose variation in the wide spectral interval cannot be neglected. Longwave gaseous transmissions are thus functions of the absorber amount, pressure, and two temperatures. This *double temperature dependence* was first consistently addressed by Ramanathan and Downey [1986] in the absorptivity-emissivity framework. It was ignored in the original ACRANEB scheme, despite the fact that in the atmosphere temperatures T and T_e can differ by several tens of K. The cure was implemented only in the ACRANEB2 scheme, where the assumption $T = T_e$ was relaxed in the NER framework. The idea, put forward by Geleyn et al. [2017], is to linearize Planck *weights* around suitably chosen temperature T_0, so that for any temperature T_e they can be expressed via fixed weights $\tilde{w}_\nu$ and $\tilde{\tilde{w}}_\nu$, proportional to the blackbody radiance $B_\nu(T_0)$ and its derivative $\mathrm{d}B_\nu/\mathrm{d}T(T_0)$:

$$w_\nu(T_e) \equiv \frac{\pi B_\nu(T_e)}{\sigma T_e^4} \approx w_\nu(T_0) + \frac{\mathrm{d}w_\nu}{\mathrm{d}T}(T_0)(T_e - T_0)$$

$$= \tilde{w}_\nu + 4\left(\frac{T_e}{T_0} - 1\right)(\tilde{\tilde{w}}_\nu - \tilde{w}_\nu) \tag{2.7}$$

$$\tilde{w}_\nu \equiv \frac{\pi B_\nu(T_0)}{\sigma T_0^4} \tag{2.8}$$

$$\tilde{\tilde{w}}_\nu \equiv \frac{\pi}{4\sigma T_0^3} \cdot \frac{\mathrm{d}B_\nu}{\mathrm{d}T}(T_0) \tag{2.9}$$

$$\int_0^\infty w_\nu(T_e)\,\mathrm{d}\nu = \int_0^\infty \tilde{w}_\nu\,\mathrm{d}\nu = \int_0^\infty \tilde{\tilde{w}}_\nu\,\mathrm{d}\nu = 1 \tag{2.10}$$

Band transmission $\tau|_{T_e}$, averaged with Planck weights $w_\nu(T_e)$, is then approximated as

$$\tau|_{T_e} \equiv \int_0^\infty \tau_\nu w_\nu(T_e)\,\mathrm{d}\nu \approx \tilde{\tau} + 4\left(\frac{T_e}{T_0} - 1\right)(\tilde{\tilde{\tau}} - \tilde{\tau}) \tag{2.11}$$

$$\tilde{\tau} \equiv \int_0^\infty \tau_\nu \tilde{w}_\nu\,\mathrm{d}\nu \tag{2.12}$$

$$\tilde{\tilde{\tau}} \equiv \int_0^\infty \tau_\nu \tilde{\tilde{w}}_\nu\,\mathrm{d}\nu, \tag{2.13}$$

where the transmissions $\tilde{\tau}$ and $\tilde{\tilde{\tau}}$ are evaluated with fixed spectral weights $\tilde{w}_\nu$ and $\tilde{\tilde{w}}_\nu$ respectively.
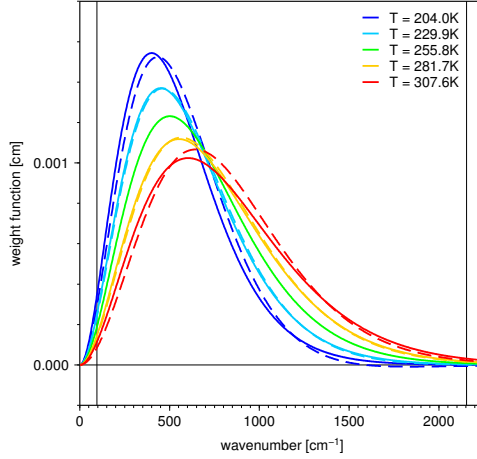
Figure 2.3: Planck weights for five different temperatures (solid lines), and their linearizations around temperature $T_0 = 255.8\,\mathrm{K}$ (dashed lines). Wavenumber $1/\lambda$ is used as horizontal coordinate. Thin vertical lines denote boundaries of ACRANEB2 longwave spectral interval. Weights are normalized so that area below each curve on interval $[0, \infty)$ is one.

Linearization (2.7) preserves normalization of Planck weights, but it does not guarantee their positive values. This can be seen from figure 2.3, where linearized weights at the lowest temperature (dashed dark blue) become slightly negative for wavenumbers $1/\lambda$ exceeding $1600\,\mathrm{cm^{-1}}$. It can also be seen that linearization of Planck weights with respect to temperature damps their wings and shifts the maximum towards higher wavenumbers. Nevertheless, figure 2.5 demonstrates that linearization (2.7) is acceptable for the meteorological range of temperatures. Here it must be stressed that linearization of Planck *function* around temperature T_0 would violate normalization of Planck weights. Even if renormalized, there would be severe problem with their negative values at low temperatures. Moreover, renormalization breaks down at temperature $T = \frac{3}{4}T_0$, where the integral becomes zero. Proposed linearization of Planck *weights* escapes this problem completely.

Strength of equation (2.11) lies in the fact that it enables to replace 4D fit of the longwave gaseous optical depth $\delta(u, p, T, T_\mathrm{e})$ with the two 3D fits $\tilde{\delta}(u, p, T)$ and $\tilde{\tilde{\delta}}(u, p, T)$, taking the shape (2.1)–(2.4). Since the correction to temperature T_e is applied on band transmissions, these must be diagnosed from the corresponding band optical depths as $\tilde{\tau} = \exp(-\tilde{\delta})$ and $\tilde{\tilde{\tau}} = \exp(-\tilde{\tilde{\delta}})$. Resulting transmission is eventually transformed back to band optical depth $\delta\big|_{T_\mathrm{e}} = -\ln\tau\big|_{T_\mathrm{e}}$. Further usage of T_e-corrected transmissions and optical depths in the NER framework is explained in sections 6.3, 6.4 and 6.6 of Geleyn et al. [2017]. The ACRANEB2 scheme chooses linearization temperature $T_0 = 255.8\,\mathrm{K}$, which is in the middle of the temperature fitting range.

Importance of discrimination between temperatures T and T_e can be demonstrated using the CIRC (Continual Intercomparison of Radiation Codes; see Oreopoulos et al. [2012]) case 2. In order to exclude gas overlap issues, only water vapour was kept and its e-type continuum was neglected. Strong impact was achieved by selecting the case with the highest precipitable water vapour
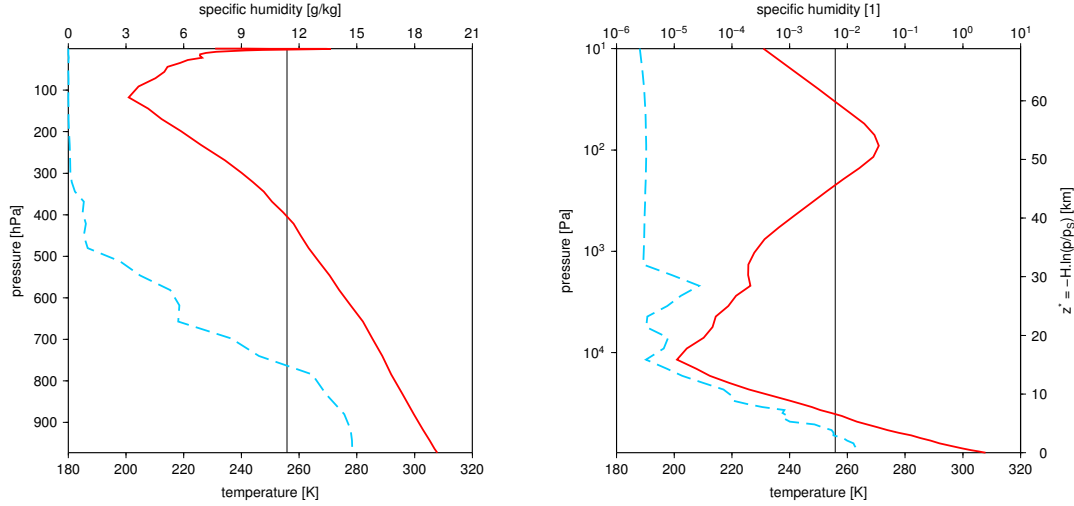
Figure 2.4: Profiles of temperature (solid red; lower scale) and specific humidity (dashed blue; upper scale) for CIRC case 2. Thin vertical line denotes linearization temperature $T_0 = 255.8\,\mathrm{K}$. **Left:** Linear pressure and humidity scales. **Right:** Logarithmic pressure and humidity scales. Height scale is approximate, obtained from pressure using characteristic height $H = 7.5\,\mathrm{km}$.

$(48.5\,\mathrm{kg\,m^{-2}})$. Vertical profiles of temperature and humidity are shown on figure 2.4. There are 54 atmospheric layers.

Figure 2.5 shows the longwave heating rates obtained by the narrowband model. Three different treatments of temperature T_e are compared. Red curve is an unapproximated reference calculation using Planck weights at temperature of the emitting body. Yellow curve uses Planck weights fixed at temperature $T_0 = 255.8\,\mathrm{K}$. Its absolute error remains below $0.2\,\mathrm{K/day}$ across most of the troposphere, reaching $0.4\,\mathrm{K/day}$ near $200\,\mathrm{hPa}$ level, and maximum $0.7\,\mathrm{K/day}$ at the top of the model domain. Apart from few isolated regions, this zeroth-order approximation works remarkably well in the troposphere and stratosphere. It differs from the isothermal emissivity method, criticized by Ramanathan and Downey [1986], by setting T_e in Planck weights to constant value T_0 instead of local value T. Green curve further improves the accuracy by linearizing Planck weights around temperature $T_0 = 255.8\,\mathrm{K}$. This first-order approximation is indeed superior to the zeroth-order one, having absolute error below $0.2\,\mathrm{K/day}$ across the whole model domain.

Performance of linearization (2.11) in the broadband scheme is demonstrated on the left panel of figure 2.6. Calculation is still of absorptivity-emissivity type, compared against unapproximated narrowband reference. Apart from the model top, absolute error of green curve is below $0.2\,\mathrm{K/day}$, confirming outstanding accuracy of the linearization (2.11), and of the broadband fits (2.1)–(2.4). Yellow curve corresponds to old ACRANEB scheme, using isothermal emissivity method alias assumption $T_\mathrm{e} = T$. Its error is positive across most of the troposphere, reaching unacceptable value $0.5\,\mathrm{K/day}$ between 500 and $600\,\mathrm{hPa}$ levels. Right panel shows the results obtained in isothermal case with $T = T_0 = 255.8\,\mathrm{K}$. Here the error of green and yellow curves is comparable, coming solely from the broadband fits. Their difference comes from the fact that the green curve uses 3D
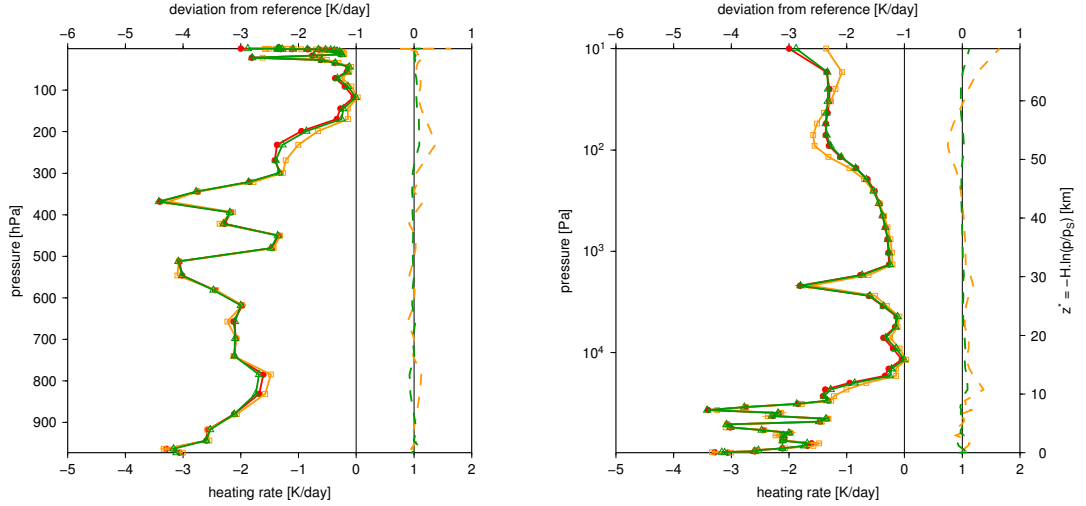
Figure 2.5: Longwave heating rates for CIRC case 2, containing only water vapour without e-type continuum, calculated by the narrowband model: red dots – true Planck weights (reference); yellow squares – Planck weights taken at temperature $T_0 = 255.8\,\mathrm{K}$; green triangles – Planck weights linearized around temperature $T_0 = 255.8\,\mathrm{K}$. Dashed lines denote deviation from reference (upper scale). **Left:** Vertical scale linear in pressure. **Right:** Vertical scale logarithmic in pressure. Height scale is approximate, obtained from pressure using characteristic height $H = 7.5\,\mathrm{km}$.

fit of $\tilde{\delta}(u, p, T)$ alias $\delta(u, p, T, T_0)$, while the yellow curve uses 3D fit of $\delta(u, p, T, T)$, which can be different from the former fit even for $T = T_0$.

Relaxing the $T_e = T$ assumption, used by the isothermal emissivity method, is a critical factor for the success of the broadband scheme with single longwave interval. It is necessitated by the considerable temperature variation across the depth of atmosphere.

2.3 Broadband treatment of water vapour e-type continuum

Infrared spectrum of water vapour consists of strong absorption bands, separated by window regions dominated by weaker continuum absorption. Still, the water vapour continuum plays an important role in controlling the longwave radiation budget, since it is 8–12 μm window where the most of terrestrial radiation escapes to space. The water vapour continuum consists of two components – the *self continuum* generated by collisions between the water vapour molecules, and the *foreign continuum* due to collisions of the water vapour molecules with molecules of other gases (for more details see Ptashnik et al. [2011a] and Ptashnik et al. [2012]). Origin of the foreign continuum is the accumulated far-wing absorption by spectral lines centred in the surrounding absorption bands. The self continuum is characterized by proportionality of its absorption cross section to partial water vapour pressure e, discovered in 1960s and first separated from the foreign continuum by Bignell [1970]. Origin of the self continuum is still
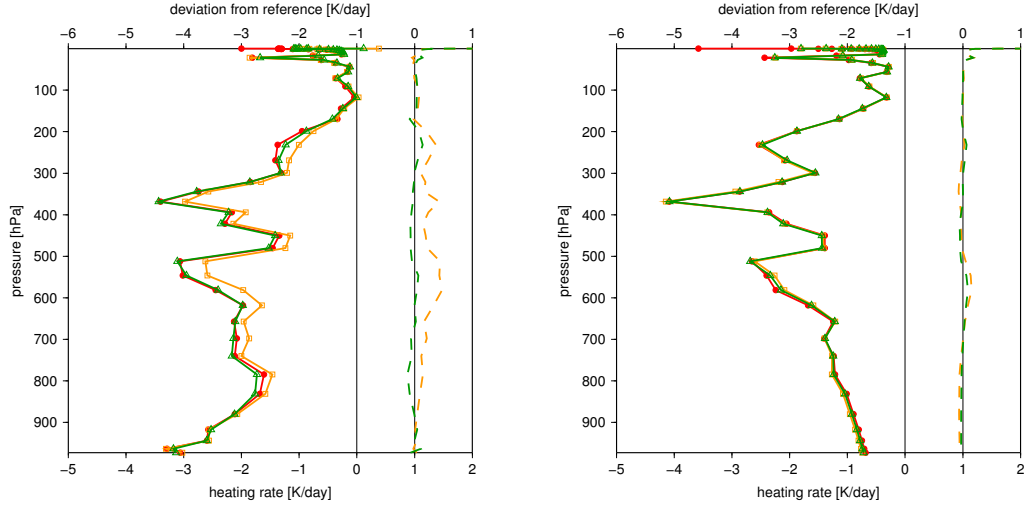
Figure 2.6: Longwave heating rates for CIRC case 2, containing only water vapour without e-type continuum: red dots – narrowband reference; yellow squares – broadband scheme with $T_e = T$ assumption; green triangles – broadband scheme with linearization (2.7) and $T_0 = 255.8\,\mathrm{K}$. Dashed lines denote deviation from reference (upper scale). **Left:** Unmodified temperature profile. **Right:** Temperature profile reset to constant value $T = T_0$.

a matter of debate (for historical overview and recent developments see Shine et al. [2012]). Two competing theories assume the generating mechanism to be either absorption by water dimers, or far-wing absorption by water monomer lines, differing significantly from Lorentzian profile. The main complication for verifying these theories, especially in the near-infrared region, is the lack of laboratory measurements in conditions representing the Earth's atmosphere (Shine et al. [2016]). Moreover, different mechanisms can dominate water vapour continuum in different spectral regions. According to critical review of Ptashnik et al. [2011b], 20–40% of observed mid-infrared and far-infrared self continuum can be explained by true-bound water dimers, plus there can be comparable contribution from quasi-bound dimers. They also claim that in the near-infrared region, modern continuum models can underestimate water vapour self continuum by around an order of magnitude.

Nevertheless, for the practical purpose a semi-empirical model of the water vapour continuum was created by Clough et al. [1989], later significantly improved by Mlawer et al. [2012] and referred to as MT_CKD (Mlawer-Tobin-Clough-Kneizys-Davies). It combines the effect of collisionally broadened water monomer lines, having exponentially decaying far wings, with the effect of weak interactions involving water vapour molecules, resulting in a broader continuum. The first mechanism is responsible for stronger continuum observed inside absorption bands, while the second dominates in window regions. Empirical parameters of the MT_CKD model were determined from the fit to available observations. The model itself then enables to extrapolate results from data-rich to data-sparse regions, but according to Ptashnik et al. [2011a] such extrapolation is questionable in the near-infrared and visible regions. This can be a problem for remote sensing but not so much for the ACRANEB2 scheme, which assumes water vapour self

44

continuum only in the longwave spectrum, relying on the fact that in the short-wave spectrum it is much weaker and masked by water vapour line absorption and by the foreign continuum.

Absorption coefficient of the water vapour continuum can be written as

$$k_\nu^{\text{cont}} = c_\nu^{\text{self}}(T)e + c_\nu^{\text{foreign}}(T)(p - e)$$
$$= [c_\nu^{\text{self}}(T) - c_\nu^{\text{foreign}}(T)]e + c_\nu^{\text{foreign}}(T)p \equiv c_\nu^{e-\text{type}}(T)e + c_\nu^{\text{foreign}}(T)p, \quad (2.14)$$

where c_ν^{self} and c_ν^{foreign} are the self and foreign continuum coefficients depending only on temperature T, e is partial pressure of water vapour, p is total pressure, so that $p - e$ is partial pressure of dry air. Difference $c_\nu^{\text{self}} - c_\nu^{\text{foreign}} \equiv c_\nu^{e-\text{type}}$ will be referred to as the e-type continuum coefficient. It is always positive, since in the MT_CKD version 2.5.2 the foreign continuum coefficient is at least about one order of magnitude smaller than the self continuum coefficient.

Using equation (2.14), optical depth due to the water vapour continuum can be expressed as

$$\delta_\nu^{\text{cont}} \equiv k_\nu^{\text{cont}}u = c_\nu^{e-\text{type}}(T)eu + c_\nu^{\text{foreign}}(T)pu, \quad (2.15)$$

where u is water vapour amount along the optical path. For a homogeneous path it is proportional to specific humidity q, which is up to the first order proportional to partial pressure of water vapour e:

$$q = \frac{R_\text{d}e}{R_\text{v}p - (R_\text{v} - R_\text{d})e} \approx \frac{R_\text{d}}{R_\text{v}} \cdot \frac{e}{p} \quad (2.16)$$

Symbols R_d and R_v denote gas constant of dry air and of water vapour, respectively. From equation (2.16) it follows that the product eu is proportional to e^2, and this quadratic dependence is a signature characterizing the e-type absorption. Even though definition of the continuum absorption is somewhat *arbitrary*, depending both on the line cut-off procedure (see figure 3 of Ptashnik et al. [2011a]) and on the assumed line shape, equation (2.15) enables to isolate the e-type part *uniquely*. This is because doubling the water vapour amount at the given pressure and temperature doubles the line and foreign continuum absorptions, but quadruples the e-type continuum absorption.

In the old ACRANEB scheme, the e-type continuum was derived using the idea of Bignell et al. [1963], supposing that the half-widths of self broadened water vapour lines are an empirical multiple of their foreign broadened values. Ritter and Geleyn [1992] compared values calculated by this method with the experimental data of Burch [1981], finding factor 50 as a reasonable compromise.[5] However, since the measurements in the 8–12 μm window were available only at single temperature of 296 K, at the time it was not recognized that the method gives too steep negative temperature dependence, leading to overestimated e-type absorption at low temperatures. The ACRANEB2 scheme removes this deficiency by importing the water vapour e-type continuum from the recent MT_CKD continuum model (Mlawer et al. [2012]), using its version 2.5.2. Spectral profile and temperature dependence of these reference data is depicted on figure 2.7. It shows rather smooth spectral variation and strong decrease of the e-type continuum coefficient with temperature.

---

[5]Bignell et al. [1963] found this factor to be around 30 in the mid-infrared region, while according to Shine et al. [2012], the modern value is only around 5.
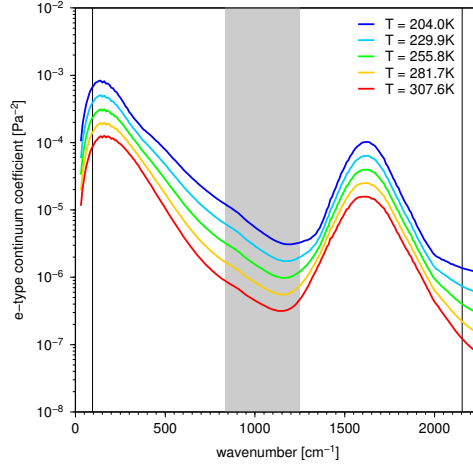
Figure 2.7: Spectral profiles of water vapour e-type continuum coefficient $c_\nu^{e-\text{type}}(T)$, taken from MT_CKD model version 2.5.2, plotted for five different temperatures. Wavenumber $1/\lambda$ is used as horizontal coordinate. Thin vertical lines denote boundaries of ACRANEB2 longwave spectral interval. Grey belt is the 8–$12\,\mu$m window.

Broadband parameterization of the e-type continuum has to deal with its strong spectral overlap with water vapour line absorption, as well as with the optical saturation. In order to accommodate both effects, Malkmus formula (2.1) was extended by the non-linear function of argument $c(T)eu$, which is the broadband analogue of monochromatic optical depth $c_\nu^{e-\text{type}}(T)eu$:

$$\delta_{\text{malkmus}}^{e-\text{type}}(u,p,e,T) = \delta_{\text{malkmus}}(u,p,T) + \frac{c(T)eu}{1 + c_3 c(T)eu} + c_4[c(T)eu]^{c_5} \qquad (2.17)$$

$$c(T) = c_1 \exp(-c_2 T)$$

$$c_1, c_2, c_3, c_4, c_5 > 0$$

Extended broadband Malkmus formula (2.17) is still the subject to corrections (2.2)–(2.4). It introduces five additional fitting parameters c_1 to c_5. For small absorber amounts u the second term linearizes to $c(T)eu$, while for big absorber amounts it saturates at value $1/c_3$. The slope is then controlled by the third term, which continues to grow and adjusts asymptotic behaviour given by rescaling (2.2). Formula (2.17) is designed in such way that in the limit $e \to 0$ it reduces back to original formula (2.1).

Parameters c_1 to c_5 were fitted using the same set of homogeneous optical paths as before, with the (u,p,T) fitting domain extended by specific humidities $q = 10^{-7}, 10^{-6}, 10^{-5}, \ldots, 10^{-2}$. These were needed for diagnosing partial water vapour pressure:

$$e = \frac{R_v q}{R_d + (R_v - R_d)q} \cdot p \qquad (2.18)$$

Cost function was still based on the root-mean-square error of $\ln \delta(u,p,e,T)$ with respect to the narrowband reference. In order to obtain maximum accuracy in the meteorologically relevant region, supersaturated states were excluded. Fitting procedure did not touch previously found values of 33 parameters occurring in
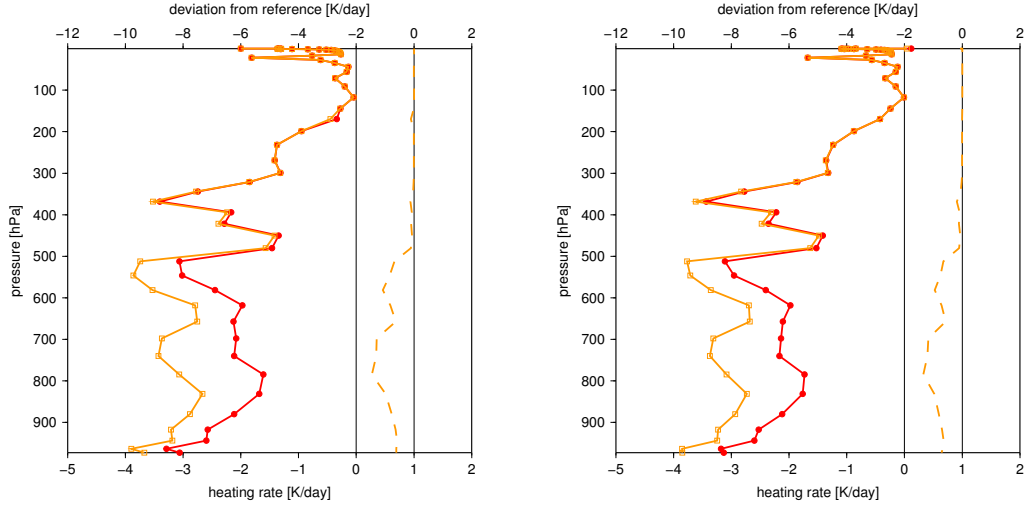
46

Figure 2.8: Longwave heating rates for CIRC case 2, containing only water vapour: red dots – e-type continuum excluded (reference); yellow squares – e-type continuum included. Dashed lines denote deviation from reference (upper scale). **Left:** The narrowband reference. **Right:** The ACRANEB2 scheme.

equations (2.1)–(2.4). These were simply reused in the evaluation of water vapour optical depths based on equations (2.1), (2.17) and (2.2)–(2.4). Consistently with section 2.2, two fits had to be performed – one with spectral weights $\tilde{w}_\nu$, other with spectral weights $\tilde{\tilde{w}}_\nu$. Success of the proposed treatment is indicated by the fact that an inclusion of the e-type continuum did not increase overall root-mean-square error of the broadband fits by more than 2%.

Final quality of the broadband e-type continuum treatment can be judged from figure 2.8. It compares longwave heating rates for CIRC case 2, again containing only water vapour. Two things are apparent. First, significance of the water vapour e-type continuum in warm and humid lower troposphere, resulting in stronger cooling below 500 hPa level – yellow curves including the e-type continuum give up to 1.5 K/day more cooling than the red curves excluding it. Difference starts to be visible around level where specific humidity q quickly rises above value 1 g/kg. Second, responses of the narrowband reference (left panel) and the broadband scheme (right panel) to inclusion of the e-type continuum, indicated by dashed yellow lines, are in excellent agreement. It means that the broadband methodology works fine, and it should not be invalidated by the future updates of the reference continuum model.

Values of the broadband fitting coefficients are not listed here. They can be found in appendix D of Mašek et al. [2016] for the shortwave gaseous optical depths, and in appendix B of Geleyn et al. [2017] for the longwave ones.

2.4 Non-random spectral overlaps between gases

The ACRANEB2 scheme considers absorption by three gases – H_2O, CO_2+ and O_3. Atmospheric abundances of H_2O and O_3 vary in space and time, and

these variations must be taken into account in the NWP models.[6] Situation with remaining radiatively active gases is different. These are well mixed across the troposphere and stratosphere, and their dry air mixing ratios can be assumed constant in the time scales of weather forecast. This enables to create CO_2+ as a fixed composition mixture of CO_2, N_2O, CH_4 and O_2,[7] and to fit broadband optical depth of the mixture as a whole, not component by component. Advantage of such approach is not only reduced computational cost of the scheme, but also an automatic inclusion of spectral overlaps between individual components, treated explicitly in the fitting reference. Remaining challenge for the broadband scheme is to parameterize non-random spectral overlaps between H_2O, CO_2+, and O_3. While in the shortwave spectrum they can be neglected without doing much harm (see figure 3 of Mašek et al. [2016]), in the longwave spectrum they must definitely be accounted for (see figure 15 of Geleyn et al. [2017]).

Results given in sections 2.1–2.3 were purposely presented only for one gas at a time, in order to avoid the overlap problem, which is addressed here. Starting point is the fact that if the transmissions of gases 1 and 2 are *spectrally uncorrelated*, band transmission of the mixture is the product of individual band transmissions, while band optical depth of the mixture is the sum of individual band optical depths:

$$\tau_{12}^{\text{rand}} = \tau_1 \tau_2 \tag{2.19}$$

$$\delta_{12}^{\text{rand}} = \delta_1 + \delta_2 \tag{2.20}$$

Superscript 'rand' is just another way of saying that there is no spectral correlation. In other words, absorptions of the two gases overlap *randomly* in the considered spectral interval.

In the parameterization it is more convenient to work with band absorptivity $\mathsf{a} \equiv 1 - \tau$, for which the condition (2.19) translates to:

$$\mathsf{a}_{12}^{\text{rand}} = \mathsf{a}_1 + \mathsf{a}_2 - \mathsf{a}_1 \mathsf{a}_2 \tag{2.21}$$

Random assumption usually holds well in the narrow spectral intervals, but not necessarily in the broader ones. Here the resulting band absorption a_{12} can differ from random value (2.21) by non-negligible departure $\Delta \mathsf{a}_{12}$:

$$\mathsf{a}_{12} = \mathsf{a}_{12}^{\text{rand}} + \Delta \mathsf{a}_{12} \tag{2.22}$$

Aim of the parameterization is to fit departure $\Delta \mathsf{a}_{12}$ as the function of suitable variables. First attempt assumed 4D dependence $\Delta \mathsf{a}_{12}(u_1, u_2, p, T)$, with u_1 and u_2 being absorber amounts. Later it was found that replacing absorber amounts by absorptivities a_1 and a_2 enables to omit explicit dependence of $\Delta \mathsf{a}_{12}$ on pressure and temperature, reducing the problem to 2D fit.

Second simplification, reducing the problem further to 1D fit, arises from the fact that relative departure $\Delta \mathsf{a}_{12}/\mathsf{a}_{12}^{\text{rand}}$ becomes small when the individual absorptivities have very different values. This can be understood by assuming

---

[6]Water vapour is a prognostic quantity, while for ozone monthly climatology is sufficient when considering broadband energy budget. Near real-time ozone data are however needed for applications such as calculation of UV index.

[7]Old ACRANEB scheme considered also CO, but it has negligible impact on energy budget since its absorption band is located near the shortwave-longwave boundary.

$\mathsf{a_2/a_1} \ll 1$. In such case $\mathsf{a_{12}^{rand}} \sim \mathsf{a_1}$, while the gas 2 cannot shift absorptivity of the mixture by more than $\sim\mathsf{a_2}$ from random value. Mathematically it means:

$$\frac{|\Delta\mathsf{a_{12}}|}{\mathsf{a_{12}^{rand}}} \lesssim \frac{\mathsf{a_2}}{\mathsf{a_1}} = \min\left(\frac{\mathsf{a_1}}{\mathsf{a_2}}, \frac{\mathsf{a_2}}{\mathsf{a_1}}\right) = \frac{1}{\max\left(\dfrac{\mathsf{a_1}}{\mathsf{a_2}}, \dfrac{\mathsf{a_2}}{\mathsf{a_1}}\right)} \approx \frac{1}{\dfrac{\mathsf{a_1}}{\mathsf{a_2}} + \dfrac{\mathsf{a_2}}{\mathsf{a_1}}} \tag{2.23}$$

Final formulation of inequality (2.23) is symmetric, so that it applies also for $\mathsf{a_1/a_2} \ll 1$. It is then natural to express departure $\Delta\mathsf{a_{12}}$ for *any* values of $\mathsf{a_1}$ and $\mathsf{a_2}$ as:

$$\Delta\mathsf{a_{12}}(\mathsf{a_1}, \mathsf{a_2}) = \mathsf{f}(\mathsf{a_1}, \mathsf{a_2}) \cdot \mathsf{g}(\mathsf{a_{12}^{rand}}) \tag{2.24}$$

$$\mathsf{f}(\mathsf{a_1}, \mathsf{a_2}) \equiv \frac{2\mathsf{a_1a_2}}{\mathsf{a_1}^2 + \mathsf{a_2}^2 + \epsilon_\mathsf{d}} \tag{2.25}$$

$$\mathsf{g}(0) = 0 \qquad \mathsf{g}(1) = 0, \tag{2.26}$$

Modulation factor $\mathsf{f}(\mathsf{a_1}, \mathsf{a_2})$ is normalized so that it is one for $\mathsf{a_1} = \mathsf{a_2}$, and the small number $\epsilon_\mathsf{d} = 10^{-20}$ was added in denominator to prevent division by zero when $\mathsf{a_1} = \mathsf{a_2} = 0$. Constraints (2.26) reflect the fact that when both gases are completely transparent or completely absorbing in the considered band, so is their mixture.

The last missing bit is the function $\mathsf{g}(\mathsf{a_{12}^{rand}})$. Its shape was motivated by the scatterplots shown on figure 2.9. These were obtained by running the narrowband reference on the set of optical paths extracted from five standard ICRCCM (InterComparison of Radiation Codes in Climate Models) atmospheres defined by Ellingson and Fouquart [1991]. In order to increase the number of data points, gaseous optical depths between each pair of levels were calculated. Plotting the ratio $\Delta\mathsf{a_{12}}(\mathsf{a_1}, \mathsf{a_2})/\mathsf{f}(\mathsf{a_1}, \mathsf{a_2})$ against random absorptivity $\mathsf{a_{12}^{rand}}$ revealed rather sharp dependences, especially striking for the most important (H_2O, CO_2+) overlap. For gaseous pairs containing O_3 the scatter is bigger, contributed by less important cases with strongly asymmetric absorptivities $\mathsf{a_1}$ and $\mathsf{a_2}$, indicated by lighter shades of grey. Anyway, scatterplots confirm plausibility of equations (2.24)–(2.26), indicating rather simple shape of function $\mathsf{g}(\mathsf{a_{12}^{rand}})$. It was proposed with only four fitting parameters A, B, C and D, reducing the risk of overfitting:

$$\mathsf{g}(\mathsf{a_{12}^{rand}}) = \mathsf{A}(1 - \mathsf{a_{12}^{rand}})^\mathsf{B}(\mathsf{a_{12}^{rand}})^\mathsf{C}(1 - \mathsf{Da_{12}^{rand}}) \tag{2.27}$$
$$\mathsf{B}, \mathsf{C} > 0$$

Positive values of B and C are needed in order to ensure constraints (2.26). In the fitting procedure, more strict requirements $\mathsf{B}, \mathsf{C} \geq 0.5$ were applied. On the contrary to Geleyn et al. [2017], restriction $\mathsf{D} \geq 1$ was relaxed, in order to improve quality of the fits in cases where the function $\mathsf{g}(\mathsf{a_{12}^{rand}})$ does not change sign.

Values of fitting coefficients are given in table 2.1, corresponding to green curves on figure 2.9. Two sets of values must be delivered – one obtained with spectral weights $\tilde{w}_\nu$, other with spectral weights $\tilde{\tilde{w}}_\nu$. It should be stressed that the fitting was not done on the function $\mathsf{g}(\mathsf{a_{12}^{rand}})$ directly, but the minimized quantity was the sum of squared differences $[\mathsf{a_{12}} - (\mathsf{a_{12}})_{ref}]$, more representative of the overall error. This explains why fitted curves tend to pass through darker data points – these have bigger influence, thanks to higher modulation factor $\mathsf{f}(\mathsf{a_1}, \mathsf{a_2})$. Linear
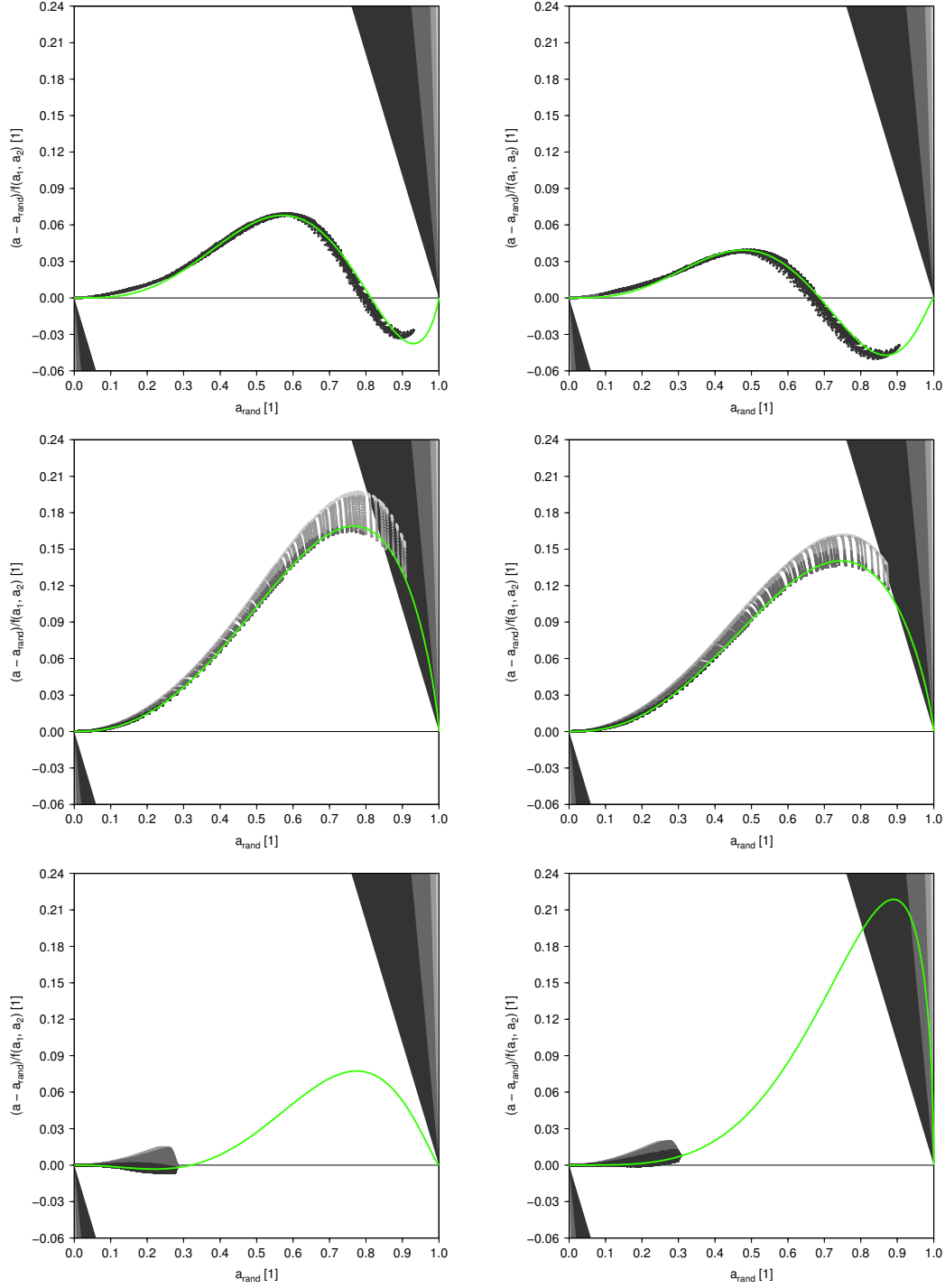
Figure 2.9: Fits of pair gaseous overlaps in the longwave spectrum. Shown is the ratio $\Delta a_{12}(a_1, a_2)/f(a_1, a_2)$, plotted against random absorptivity a_{12}^{rand}. Fitted dependence $g(a_{12}^{\text{rand}})$ is green, data points are grey. Shades of grey from the darkest to lightest correspond to modulation factor $f(a_1, a_2)$ from the intervals 1–$10^{-\frac{1}{2}}$–10^{-1}–$10^{-\frac{3}{2}}$–10^{-2}. Corresponding linear envelopes ensuring the final absorptivity a_{12} from the physical range $[0, 1]$ are also shown. **Left:** Results obtained with spectral weights $\tilde{w}_\nu$. **Right:** Results obtained with spectral weights $\tilde{\tilde{w}}_\nu$. **Top:** Pair (H_2O, CO_2+). **Middle:** Pair (H_2O, O_3). **Bottom:** Pair (CO_2+, O_3).

	spectral weights $\tilde{w}_\nu$		
gaseous pair	(H_2O, CO_2+)	(H_2O, O_3)	(CO_2+, O_3)
parameter			
A	3.394E+00	8.811E−01	−6.600E−01
B	8.659E−01	7.989E−01	1.237E+00
C	3.514E+00	2.468E+00	2.538E+00
D	1.229E+00	−2.366E−01	3.119E+00

	spectral weights $\tilde{\tilde{w}}_\nu$		
gaseous pair	(H_2O, CO_2+)	(H_2O, O_3)	(CO_2+, O_3)
parameter			
A	3.564E+00	1.111E+00	4.406E−02
B	1.238E+00	8.129E−01	5.042E−01
C	3.407E+00	2.600E+00	3.117E+00
D	1.455E+00	2.352E−01	−2.327E+01

Table 2.1: Dimensionless fitting parameters for the longwave pair gaseous overlaps. The CO_2+ mixture corresponds to atmospheric composition of year 2010, taken from WDCGG (World Data Centre for Greenhouse Gases) report: 389 ppmv of CO_2, 0.323 ppmv of N_2O, 1.808 ppmv of CH_4 and 209 460 ppmv of O_2.

envelopes on figure 2.1 mark forbidden regions where the fitted result would have to be truncated in order to ensure final absorptivity from the interval $[0, 1]$, provided that modulation factor reaches the value corresponding to given shade of grey. Practically it should not happen, since the problematic portions of green curves, visible for gaseous pairs containing O_3, are not supported by data points of given shade. They are therefore extrapolated beyond underlying ICRCCM cases, and it is very unlikely that they will be entered in a meteorologically relevant situations. For gaseous pairs containing H_2O, random longwave absorptivity does not exceed ∼0.9, while for pair (CO_2+, O_3) it remains below ∼0.3. Non-random spectral overlap of the last gaseous pair is clearly the least important one, and could eventually be neglected.

Final step deals with the non-random gaseous overlaps when H_2O, CO_2+ and O_3 are present simultaneously. In such case, pair absorptivities a_{12}, a_{13} and a_{23} are calculated first, based on equations (2.21), (2.22), (2.24), (2.25) and (2.27). Then they are converted to pair optical depths δ_{12}, δ_{13} and δ_{23}, and the final broadband optical depth is determined from the formula:

$$\delta = (\delta_1 + \delta_2 + \delta_3) + (\delta_{12} - \delta_1 - \delta_2) + (\delta_{13} - \delta_1 - \delta_3) + (\delta_{23} - \delta_2 - \delta_3)$$
$$= \delta_{12} + \delta_{13} + \delta_{23} - \delta_1 - \delta_2 - \delta_3 \quad (2.28)$$

Interpretation of formula (2.28) is straightforward. It adds the random result $\delta_1 + \delta_2 + \delta_3$ with the non-random contributions of pair overlaps, neglecting the non-random contribution of triple overlap.[8] Combination must be done in the space of optical depths, not absorptivities, since the former are additive while the

---

[8]The non-random contribution of triple overlap, given as $\delta_{123} - \delta_{12} - \delta_{13} - \delta_{23} + \delta_1 + \delta_2 + \delta_3$, would be difficult to parameterize. Fortunately it is very weak, so it can be neglected without any harm.
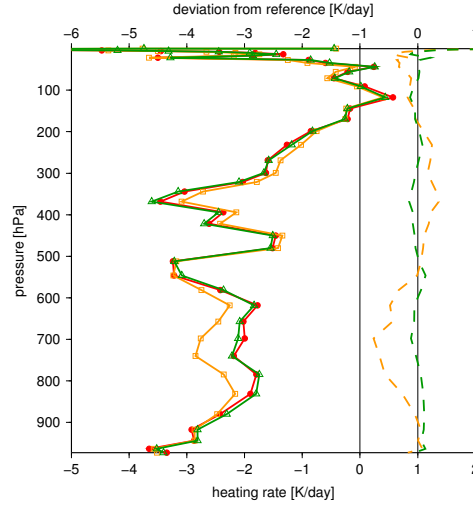
Figure 2.10: Impact non-random pair gaseous overlaps on longwave heating rates for CIRC case 2: red dots – the narrowband reference; yellow squares – the broadband scheme assuming random overlaps; green triangles – the broadband scheme with parameterized pair overlaps. Dashed lines denote deviations from the narrowband reference (upper scale). Broadband CO_2+ optical depth and CO_2+ pair overlaps with H_2O and O_3 were refitted using atmospheric composition of CIRC case 2. The longwave results, however, are not directly comparable to the published line-by-line reference, due to different assumptions made on the emission source term (piecewise constant versus vertically continuous).

latter are not. In final shape, the random result $\delta_1 + \delta_2 + \delta_3$ is subtracted, since the sum of pair optical depths $\delta_{12} + \delta_{13} + \delta_{23}$ contains contribution from each gas twice. The very last safety step is the truncation of values $\delta < \max(\delta_1, \delta_2, \delta_3)$, since the broadband optical depth of the mixture cannot fall below broadband optical depth of any component.

Accuracy of the proposed overlap treatment is demonstrated on figure 2.10, showing longwave heating rates for CIRC case 2, this time with all three gases included. Yellow curve, assuming random overlaps between gases, overestimates cooling in the lower troposphere by maximum $0.8\,\mathrm{K/day}$ at $700\,\mathrm{hPa}$ level, and underestimates it in the upper troposphere. Green curve, with parameterized non-random pair overlaps, reduces the absolute error dramatically, keeping it within $0.2\,\mathrm{K/day}$ across the troposphere and most of the stratosphere. Higher error visible near the top of domain is not caused by the overlap treatment, but it comes from the fits of individual gaseous optical depths. It is anyway in the region of little meteorological interest, at least for the short range NWP.

It is now possible to understand relative success of the longwave ACRANEB scheme, despite using isothermal emissivity assumption $T_e = T$, and neglecting non-random gaseous overlaps. From yellow curves on figures 2.6 and 2.10 it is obvious that the errors of these two approximations were in partial compensation, reducing bias especially in the lower troposphere. Improvement brought by the ACRANEB2 scheme was possible only when both these errors were removed – fixing only one of them would eventually increase the error. The line of attack was to start inspecting single gas isothermal cases, in order to verify the quality

of fitted broadband optical depths. Stepping to non-isothermal cases proved unacceptability of $T_e = T$ assumption, while going to multiple gases revealed necessity to parameterize their non-random overlaps.

Developments presented in sections 2.1–2.4 pushed the clearsky heating rate error of the ACRANEB2 scheme (both shortwave and longwave) below $0.2\,\mathrm{K/day}$ in the troposphere and most of the stratosphere, which is remarkable result for the single interval scheme. As discussed in section 9.2 of Mašek et al. [2016], main accuracy limitation in the shortwave spectrum then becomes spectrally flat surface albedo, causing error up to $0.3\,\mathrm{K/day}$. It seems that accuracy limit of the single interval approach was reached. Therefore, it does not make much sense to further improve broadband gaseous optical depths, maybe with exception of the high atmosphere. Need of higher accuracy would necessitate use of several shortwave spectral intervals.

2.5 Shortwave cloud optical saturation

With clouds entering the scene, radiation budget is altered dramatically. Difference between clear and overcast day is absolute, be it at noon or early morning. Beside obvious direct radiative effect on temperature, there are also indirect ones via water phase changes, or via influence of stratification on turbulent and convective transports. Even in the short range, accurate weather forecast is not possible without realistic interaction between radiation and clouds. The problem is demanding, since it requires reliable cloud inputs entering the radiation scheme, as well as accurate cloud optical properties derived inside. Situation is simpler but not trivial for liquid clouds, thanks to the sphericity of cloud droplets. Still the hypothesis on their size distribution must be made, given the fact that microphysics scheme works only with its one or two moments. For ice clouds, the complexity is increased considerably by the coexistence of various crystal habits, whose abundances depend not only on local conditions, but also on the cloud history. Nevertheless, there is a way out from this seemingly hopeless situation, based on observation that the spectral properties[9] of realistic droplet size distributions can be stratified along single parameter – droplet effective radius (see Hu and Stamnes [1993]). Similar approach can be applied also to ice clouds, but only after specifying composition of a 'prototype' cloud, usually representing certain type of cirrus cloud. In case of one-momentum microphysics scheme, only liquid and ice water contents are available, and the effective particle size must be diagnosed.

Compared to gaseous absorption, cloud optical properties are much smoother across the spectrum. In the longwave part of spectrum, clouds can be treated as grey bodies without sensible degradation of heating rates. In the shortwave part of spectrum, situation is different. Here the variation of single scattering albedo in the near-infrared region cannot be ignored, dropping from virtually 1 at the visible end to the minimum value 0.5 around $3\,\mu\mathrm{m}$ wavelength. According to Slingo [1989], at least four spectral intervals are needed to represent it explicitly. Single shortwave interval can thus be used only if the cloud optical saturation is

---

[9]Namely the mass extinction coefficient k_ν^{ext}, single scattering albedo ϖ_ν and asymmetry factor g_ν.

parameterized. Ignoring the saturation effect would lead to *severe* overestimation of shortwave cloud optical depth, making the scheme unusable.

In the original version of the ACRANEB scheme, cloud optical properties were derived from the underlying spectral data of Stephens [1978a,b] for liquid clouds, and of Rockel et al. [1991] for ice clouds. There was no dependence on liquid or ice water contents, equivalent to assumption of fixed effective particle size, with separate values for liquid and ice clouds. The cloud optical saturation was accounted for only *statically*, i.e. without considering actual cloud thickness. It necessarily led to too transparent thin clouds and too opaque thick clouds. Such situation was found unsatisfactory, therefore the ACRANEB cloud optical properties were revised even before gaseous transmissions. New treatment, developed in the years 2005–2006, made cloud optical properties implicitly dependent on effective particle size, via liquid or ice water content. It also parameterized the cloud optical saturation *dynamically*, by modifying mass absorption and scattering coefficients by factors that were functions of unsaturated cloud optical depth. The optical saturation was parameterized in both shortwave and longwave parts of spectrum, even if in the latter the impact was weak. Influence of cloud geometry on the optical saturation was taken into account heuristically. In the shortwave part of spectrum, vertical dependence of the cloud optical saturation was derived using the absorption approximation, which was however not very realistic. Still the main shortcoming, not realized at the time, was basing the optical saturation of ice clouds on Rockel et al. [1991] spectral data. These assumed spherical ice particles, giving spectral signature very similar to liquid clouds. It lead to a false conclusion that the cloud optical saturation is universal, independent of phase.

In the ACRANEB2 scheme, unsaturated broadband cloud optical properties were rederived from the more recent datasets (Hu and Stamnes [1993] for liquid clouds; Key et al. [2002] and Yang et al. [2005] for ice clouds in the shortwave and longwave parts of spectrum, respectively). Functional shape of the fits is given in section 6.2 of Mašek et al. [2016], with effective radius of water droplets and effective dimension of ice particles diagnosed using equations (46) and (47) therein. Parameterization of the cloud optical saturation was revised, keeping the concept of effective cloud optical depth, but updating details concerning vertical variation and cloud geometry. Separate saturation factors for liquid and ice clouds were introduced, necessitated by the results presented on figure 2.11. It shows saturation factors $c^{\text{abs}} \equiv k^{\text{abs}}/k_0^{\text{abs}}$ and $c^{\text{scat}} \equiv k^{\text{scat}\prime}/k_0^{\text{scat}\prime}$, calculated for the synthetic sample of homogeneous clouds, plotted against unsaturated cloud optical depth δ_0', where the prime denotes delta-scaled, and subscript '0' unsaturated values.[10] Each cloud was illuminated from the top, using either solar spectrum at the TOA (shortwave case), or the Planck weights at temperature $T_0 = 255.8\,\text{K}$ (longwave case). Radiative effect of gases, as well as reflection from the surface, were neglected. It should be noted that in the shortwave case, effect of sun elevation on the cloud optical saturation does not have to be considered. This is because in thicker clouds, where the saturation effect becomes important, direct solar radiation becomes converted to diffuse one within few tens of meters from the cloud top.

Figure 2.11 reveals several features, crucial for the scheme design. Apart

---

[10]Absorption coefficient k^{abs} is not subject to delta-scaling, that is why primes are omitted for it.
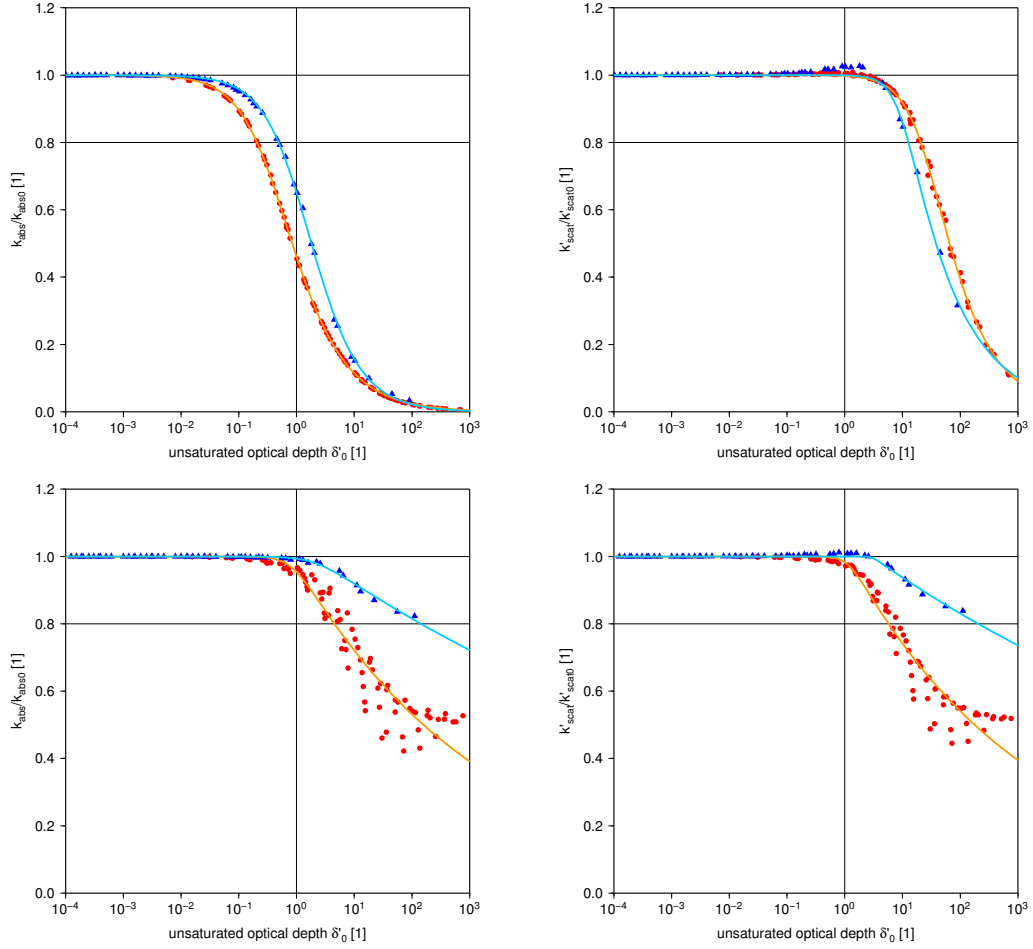
Figure 2.11: Saturation factors calculated for the synthetic sample of homogeneous clouds in vacuum, illuminated from the top: red dots – liquid clouds; dark blue triangles – ice clouds. Sample consisted of 90 liquid clouds with water contents $\rho_l = 0.01, 0.02, 0.05, 0.1, \ldots, 5\,\mathrm{g/m^3}$ and 80 ice clouds with water contents $\rho_i = 10^{-7}, 10^{-6}, 10^{-5}, \ldots, 1\,\mathrm{g/m^3}$, both of them having geometrical thicknesses $\Delta z = 10, 20, 50, 100, \ldots, 10\,000\,\mathrm{m}$. Yellow and blue curves are the fitted dependences for liquid and ice clouds, respectively. **Top:** Shortwave case. **Bottom:** Longwave case. **Left:** Cloud absorption. **Right:** Cloud scattering.

from clear separation between liquid and ice clouds, it is sharpness of shortwave dependences. The optical saturation of shortwave cloud absorption becomes significant[11] already for optical depths $\delta_0' < 1$, therefore it cannot be ignored. On the other hand, the optical saturation of shortwave cloud scattering starts to act only for optical depths $\delta_0' > 10$, i.e. in the situations with little meteorological relevance. Neglecting it should thus be harmless. Longwave dependences for liquid clouds are much less sharp. This is not a problem, since it happens either in the region where the saturation is weak, or for optical depths $\delta_0' \gtrsim 10$. Finally, longwave saturation is very weak for ice clouds, with saturation factors not falling below 0.8 for any cloud in the sample. For these reasons, the cloud optical saturation is neglected in the longwave part of spectrum, while in the shortwave part it is parameterized only for cloud absorption.

Smoothness of shortwave saturation dependences enables to describe them accurately with a simple function, containing only three fitting coefficients (subscripts 'l' and 'i' denote liquid and ice clouds, respectively):

$$c_l^{\text{abs}}(\delta_0') = \frac{1}{\left[1 + \left(\dfrac{\delta_0'}{\delta_{00l}}\right)^{m_l}\right]^{n_l}} \qquad c_i^{\text{abs}}(\delta_0') = \frac{1}{\left[1 + \left(\dfrac{\delta_0'}{\delta_{00i}}\right)^{m_i}\right]^{n_i}} \qquad (2.29)$$

Values of fitting coefficients found for liquid and ice clouds are:

$$\delta_{00l} = 0.437 \qquad m_l = 1.11 \qquad n_l = 0.617 \qquad (2.30)$$
$$\delta_{00i} = 1.35 \qquad m_i = 1.11 \qquad n_i = 0.797 \qquad (2.31)$$

Outstanding quality of these fits can be judged from the top left panel of figure 2.11. Fitted dependences are plotted also on remaining panels, but these are not used in the ACRANEB2 scheme.

The next step, initiated by the results presented on figure 2.12, was to incorporate vertical variation of the cloud optical saturation. Using the constant optical saturation for the whole cloud (green) gives the net flux at cloud boundaries within $5\,\text{W/m}^2$ from the narrowband reference (red), but it underestimates heating near the cloud top by $15\,\text{K/day}$, and overestimates it in the rest of cloud (top panels). This is because in reality, the optical saturation is weakest at the cloud top and increases towards its base. Presence of the surface reflection increases absorption near the cloud base (bottom panels), but the optical saturation in this region remains strongest. Concerning accuracy, the situation is less favourable now. The upward flux above cloud top is underestimated by $25\,\text{W/m}^2$, due to overestimated overall in-cloud absorption. Degradation caused by the surface reflection is not surprising, since the saturation curves were obtained in the idealized conditions with the perfectly absorbing surface. Still, vertically constant cloud optical saturation yields much better results than no saturation at all (blue), where the heating near the cloud top is overestimated by $25\,\text{K/day}$, and in case of perfectly reflecting surface the upward flux above cloud top is underestimated by $200\,\text{W/m}^2$.

Vertical variation of the cloud optical saturation can be introduced using the concept of *effective cloud optical depth*, which at the same time enables to accommodate impact of cloud geometry. The idea is simple – for each layer $l = 1, \ldots, L$,

---

[11]Adopted significance criterion was the saturation factor falling below 0.8.
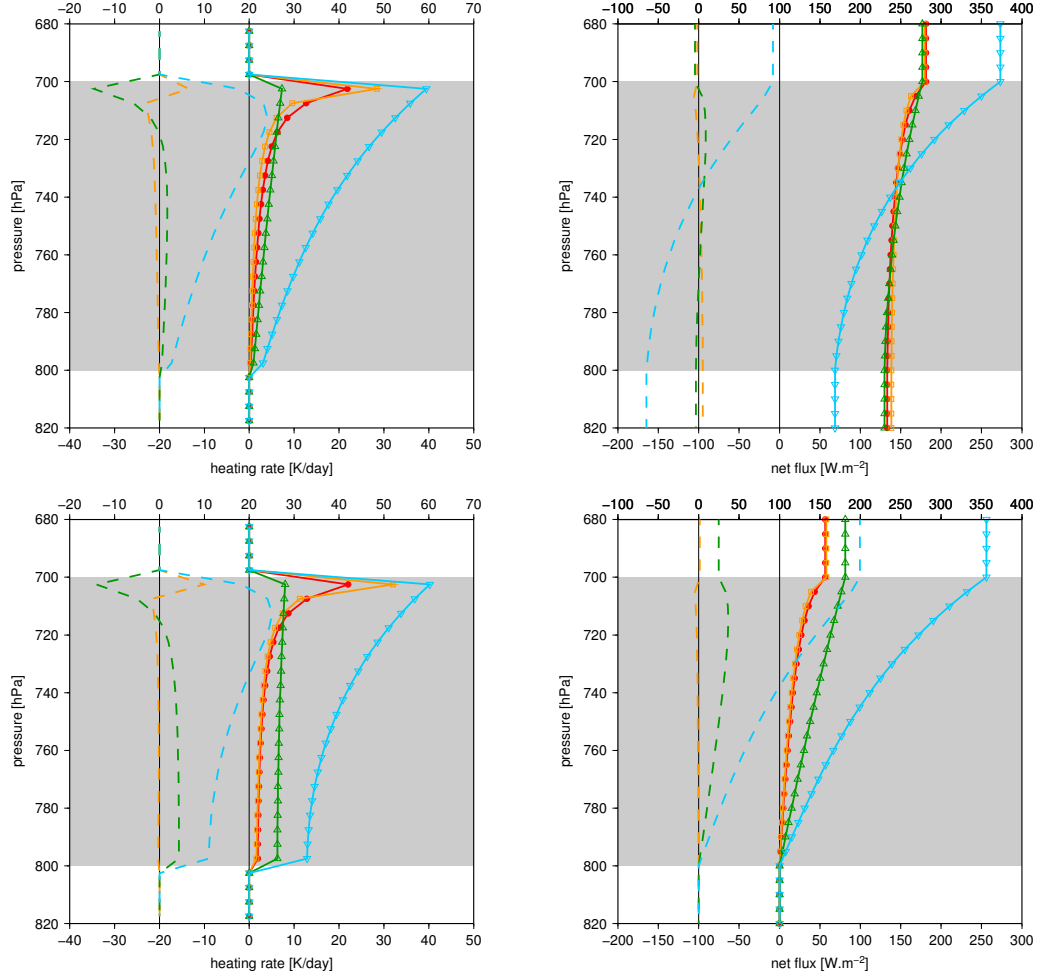
Figure 2.12: Importance of the optical saturation of shortwave cloud absorption, demonstrated for a homogeneous liquid cloud with water content $q_l = 0.1\,\mathrm{g/kg}$, extending between 700 and 800 hPa levels: red dots – the narrowband reference; yellow squares – the broadband scheme with vertically dependent cloud optical saturation; green triangles – the broadband scheme with vertically constant cloud optical saturation; blue inverse triangles – the broadband scheme ignoring cloud optical saturation. Dashed lines denote deviation from the narrowband reference (upper scale). Cloud layers are plotted in grey, radiative effect of gases is neglected. Cloud geometry is trivial – overcast at all cloudy layers. Sun elevation is 30°. **Top:** Perfectly absorbing surface. **Bottom:** Perfectly reflecting surface. **Left:** Shortwave heating rates. **Right:** Net shortwave fluxes.

local saturation factors (2.29) are evaluated replacing the argument δ'_0 by:

$$\delta_{0l}^{\text{eff}\,\prime} = \sum_{k=1}^{l-1} B_k^{\text{above}} n_k \delta'_{0k} + \delta'_{0l} + \sum_{k=l+1}^{L} B_k^{\text{below}} n_k \delta'_{0k} \tag{2.32}$$

$$B_k^{\text{above}} = \frac{B_l^{\text{above}} \rho_{lk} + B_i^{\text{above}} \rho_{ik}}{\rho_{lk} + \rho_{ik}} \qquad B_k^{\text{below}} = \frac{B_l^{\text{below}} \rho_{lk} + B_i^{\text{below}} \rho_{ik}}{\rho_{lk} + \rho_{ik}} \tag{2.33}$$

Quantity $\delta_{0l}^{\text{eff}\,\prime}$ represents effective optical depth of the whole cloud, relevant for saturation at cloud layer l. Cloud fractions n_k were included in order to suppress influence of the layers with small cloud cover. Coefficients B_k^{above} and B_k^{below} give different weight to cloud layers above and below layer l, making the optical saturation vertically dependent. They must discriminate between liquid and ice clouds according to formulas (2.33), so there are four tuning parameters B_l^{above}, B_l^{below}, B_i^{above} and B_i^{below}. Unsaturated optical depth of cloud at layer k is defined as

$$\delta'_{0k} = \left[(k_{0l}^{\text{abs}} + k_{0l}^{\text{scat}\,\prime})q_l + (k_{0i}^{\text{abs}} + k_{0i}^{\text{scat}\,\prime})q_i \right]_k \Delta p_k, \tag{2.34}$$

where q_{lk} and q_{ik} are the specific masses of cloud liquid and ice, and Δp_k is the layer pressure thickness.[12]

Optimal values of the tuning parameters occurring in formulas (2.33) were determined by fitting against the narrowband reference, using 322 atmospheric profiles extracted from the NWP model runs. Minimized quantity was the mean-square error of the net shortwave fluxes over all layer interfaces. Gaseous absorption, Rayleigh scattering and the surface reflection were taken into account on both sides, i.e. in the narrowband reference and in the ACRANEB2 scheme. The cloud optical saturation was enhanced by resetting the cloud fraction at all cloudy layers to one. Fitting procedure delivered values

$$B_l^{\text{above}} = 10 \qquad\qquad B_l^{\text{below}} = 0.029 \tag{2.35}$$

$$B_i^{\text{above}} = \ 5.3 \qquad\qquad B_i^{\text{below}} = 0.024, \tag{2.36}$$

where the dominance of the 'above' parameters over the 'below' ones ensures increasing effective cloud optical depth alias optical saturation as one moves from the top of the highest cloud to the base of the lowest one. Success of the tuning (2.35)–(2.36), still in the idealized conditions, can be judged from yellow curves on figure 2.12. Absolute error of the net flux is now within several W/m^2, regardless of surface reflection. Vertical heating rate profiles are very realistic, with absolute error below $2\,\text{K/day}$ in most of cloud, reaching maximum value around $10\,\text{K/day}$ at its topmost layer.

Final test demonstrates the performance of parameterization (2.29)–(2.36) in realistic conditions, where absorption by atmospheric gases, Rayleigh scattering and the surface reflection all take part. Case of waving cold front was selected, namely the snapshot over Prague having rich cloud structure and high precipitable water vapour $41\,\text{kg/m}^2$. Corresponding model atmospheric profiles are given on figure 2.13, showing existence of three separate cloud layers – ice top layer, mixed medium layer and liquid bottom layer – yielding liquid and ice water paths 85 and $77\,\text{g/m}^2$, respectively. Cloud fraction ranging from 0–0.5 ensured non-trivial cloud geometry.

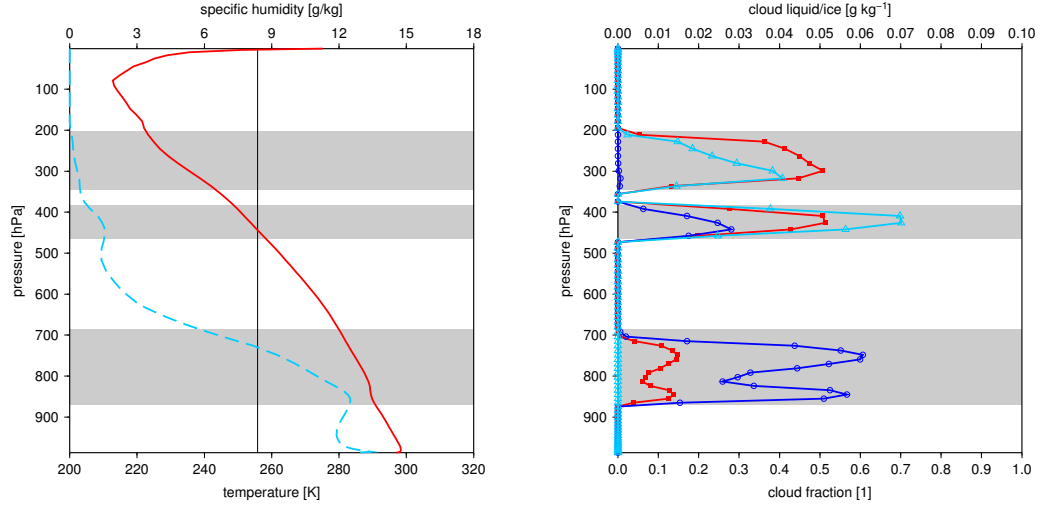[12]Mass absorption and scattering coefficients are thus expressed in inverse pressure units.

Figure 2.13: Atmospheric profiles over Prague on 01-Jul-2012 at 18:00 UTC, extracted from experimental ALADIN run. Passage of the frontal wave created three separate cloud layers plotted in grey. **Left:** Profiles of temperature (solid red; lower scale) and specific humidity (dashed blue; upper scale). **Right:** Profiles of cloud fraction (red squares; lower scale), cloud liquid and ice (dark blue circles and blue triangles; upper scale).

Resulting shortwave heating rates are presented on figure 2.14. They are relatively small due to the low sun, still showing importance of the cloud optical saturation convincingly. Neglecting it (green) causes overestimation of shortwave heating rates, most severe in the medium and bottom cloud layers, where it reaches factor of 3 or even more. Largest absolute error with respect to the narrowband reference (red) is seen in the medium cloud layer, reaching $1.8 \, \text{K/day}$. With the parameterized optical saturation of shortwave cloud absorption (yellow), absolute error in all cloud layers remains within $0.2 \, \text{K/day}$, which is remarkable result. Among the other things it proves that the treatment of mixed liquid-ice clouds works excellently, despite the fact that underlying fits (2.29)–(2.31) were done for pure liquid and pure ice clouds. Another important observation is that accuracy of shortwave heating rates is retained for both extreme cloud overlap treatments – maximum-random (left panel) and random (right-panel) – so the parameterization should work well also for the generalized cloud overlap.

The parameterized optical saturation of shortwave cloud absorption is a key result of this thesis, introducing the band approach for clouds. This component turned to be *critical* for success of the shortwave scheme with single spectral interval. The proposed treatment is very compact, containing only 10 fitting coefficients altogether, still taking cloud geometry and scattering into account. Even though underlying design choices were well motivated, accuracy achieved in realistic conditions came as a welcome surprise.
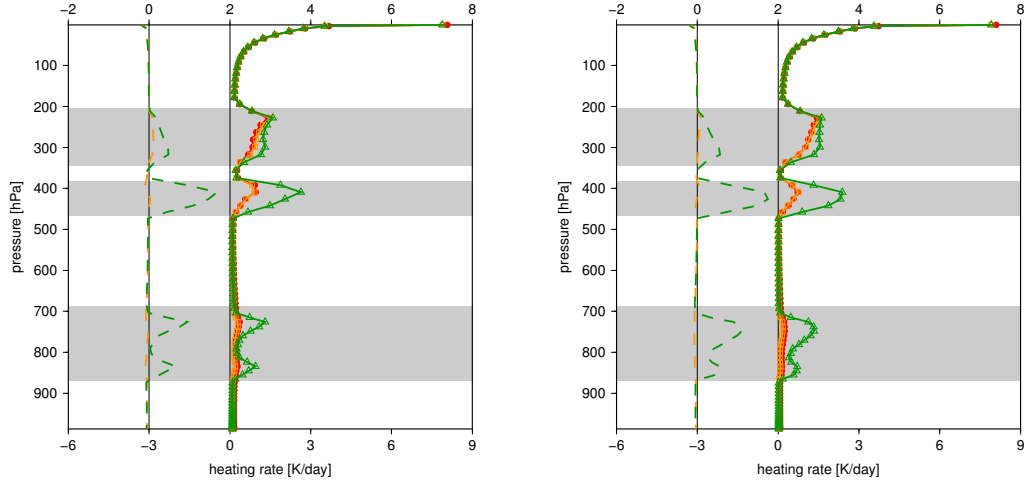
Figure 2.14: Shortwave heating rates for the case shown on figure 2.13: red dots – the narrowband reference; yellow squares – the broadband scheme with parameterized optical saturation of shortwave cloud absorption; green triangles – the broadband scheme ignoring cloud optical saturation. Dashed lines denote deviation from the narrowband reference (upper scale). Cloud layers are plotted in grey. Sun elevation is 9.2°, Lambertian surface has albedo $\bar{\alpha}_S = 0.18$. **Left:** Maximum-random overlap between cloud layers. **Right:** Random overlap between cloud layers.

2.6   Revised bracketing technique

Main challenges of the longwave radiative transfer are the existence of multiple emission sources, and strong temperature dependence of emitted radiation. In case of band approach, the gaseous optical saturation must be evaluated individually for each emission source, so that in final effect transmission between each pair of levels is needed. Non-multiplicativity of band transmissions yields computational cost quadratic in the number of atmospheric layers L, which becomes prohibitive at high vertical resolutions.

The ACRANEB and ACRANEB2 schemes bypass the L^2 computational barrier by the NER decomposition with bracketing. Details of ACRANEB2 implementation can be found in section 6 of Geleyn et al. [2017], and they will not be repeated here. Main idea is to split the net longwave flux into CTS (Cooling To Space), EWS (Exchange With Surface) and EBL (Exchange Between Layers) components. CTS and EWS fluxes consist of pair exchanges where one of the exchanging bodies is space[13] and the Earth's surface respectively, while the other body is the model atmospheric layer. CTS and EWS components can be calculated cheaply, since they involve only $L + 1$ and L exchanging pairs.[14] Computationally expensive component is the EBL flux, consisting of internal atmospheric exchanges, counting $L(L-1)/2$ layer pairs. It is typically much smaller than the CTS flux (see figure 3 of Geleyn et al. [2017]), so it is logical to approximate it.

---

[13]Space is treated as a blackbody with zero absolute temperature, i.e. the cosmic background radiation is not assumed due to its negligible energy.

[14]By convention, exchange between the Earth's surface and space is included in CTS, not in EWS flux.

The bracketing technique first calculates cheap minimum and maximum EBL *estimates* $F^{\text{EBL,min}}$ and $F^{\text{EBL,max}}$, then it interpolates the true EBL flux F^{EBL} between them. Estimation is based on two observations, valid in the absence of scattering:

1. Band optical depth of the layer decreases as the observer moves away from it. It is therefore highest when the observer is at the layer boundary, and lowest when the layer is viewed either from the surface or from space (indexing is explained on figure 2.15):

$$\Delta\delta_l^{\min} = \min(\delta(\tilde{0}, \tilde{l}) - \delta(\tilde{0}, \tilde{l} - 1), \delta(\tilde{l} - 1, \tilde{L}) - \delta(\tilde{l}, \tilde{L})) \qquad (2.37)$$

$$\Delta\delta_l^{\max} = \delta(\tilde{l} - 1, \tilde{l}) \qquad (2.38)$$

2. Exchanges in optically thick atmosphere are generally stronger than in optically thin one. This is because in the monochromatic case with no scattering, the net exchange between layers k and l has the shape

$$E_{kl\nu} = \underbrace{\tau_\nu(1 - \tau_{k\nu})(1 - \tau_{l\nu})}_{\text{optical factor}} \cdot \underbrace{[\pi B_\nu(T_k) - \pi B_\nu(T_l)]}_{\text{Planck factor}}, \qquad (2.39)$$

where $\tau_{k\nu}$ and $\tau_{l\nu}$ are the transmissions of exchanging layers, and τ_ν is the transmission of separating environment. Positive net exchange $E_{kl\nu}$ means prevailing energy flux from layer k to layer l. Optical factor is never negative, while the sign of Planck factor is determined by the temperature difference $T_k - T_l$. Exchange between completely transparent layers is zero. With increasing opacity of the atmosphere, the net exchange grows due to increasing product of layer emissivities $(1 - \tau_{k\nu})(1 - \tau_{l\nu})$, until the point where the growth is overridden by decreasing transmission τ_ν.[15]

From these observations it follows that minimum and maximum EBL estimates can be calculated using layer optical depths (2.37) and (2.38) respectively, assuming their additivity alias *greyness*. Two remarks are needed here. First, since in the longwave spectrum the only non-grey bodies are gases, equations (2.37)–(2.38) need to be applied only on gaseous optical depths. Taking into account double temperature dependence of grey optical depths (2.37)–(2.38) is not possible exactly, since each layer transmits radiation of multiple sources and these can have different temperatures T_{e}. Gaseous optical depths (2.37)–(2.38) are therefore evaluated using fixed weights $\tilde{w}_\nu$, appropriate in the limit when temperatures of exchanging bodies are close to linearization temperature T_0. Second, approximate nature of minimum and maximum EBL estimates does not guarantee that the true EBL flux will always lie between them. Apart from already explained reasons, additional one arises in situations where the temperature profile is not monotonic, so that different exchanges crossing given layer can have different signs. Increasing/decreasing absolute value of each exchange does not necessarily mean that the absolute value of their sum will also increase/decrease.

---

[15]For *adjacent* layers there is $\tau_\nu = 1$, so that growth continues until the blackbody limit $E_{kl\nu} = \pi B_\nu(T_k) - \pi B_\nu(T_l)$.
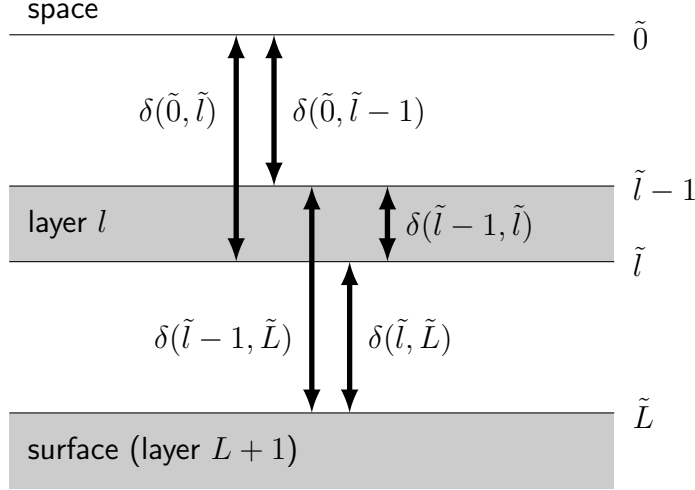
Figure 2.15: Broadband optical depths needed for minimum and maximum EBL estimates. There are L atmospheric layers $1, \ldots, L$ numbered from the top to bottom, with $L+1$ interfaces $\tilde{0}, \ldots, \tilde{L}$. The Earth's surface is treated as a completely non-transparent layer $L+1$.

Bracketing of the EBL flux can be mathematically written as

$$F^{\mathrm{EBL}} = (1-\alpha)F^{\mathrm{EBL,min}} + \alpha F^{\mathrm{EBL,max}} + \beta \qquad (2.40)$$
$$0 \le \alpha \le 1,$$

where α is interpolation weight and β is offset. They are both vertically dependent quantities. Equation (2.40) is applied at every layer interface, where the fluxes are evaluated. Value $\alpha = 0$ means that the EBL flux is dominated by *distant* exchanges, while $\alpha = 1$ means dominance of *local* exchanges. In the old ACRANEB scheme, bracketing weight α was determined by the statistical fit of reference *clearsky* results, and offset β was set to zero. It was found empirically that local exchanges dominate lower down in the atmosphere and in the regions of strong temperature inversions. The statistical fit took this into account by making weight α depending on normalized pressure and on vertical potential temperature gradient. Influence of clouds on bracketing weight was not considered, i.e. the fit obtained in the range of clearsky conditions was then applied in the full case with aerosols and clouds. Non-obvious fact that bracketing weight is little affected by clouds[16] not only simplified the fitting problem, but later it became a *key assumption* of the self-learning algorithm combined with selective intermittency.

Main advantage of statistically fitted bracketing weight was its simple and cheap calculation. With improved longwave gaseous transmissions, however, accuracy of the statistical fit became insufficient, compromising the final result. Another disadvantage was a necessity to redo the statistical fit at every change of the model vertical resolution, since maximum EBL estimate, unlike the true EBL flux and its minimum estimate, turned to be strongly resolution dependent. For

---
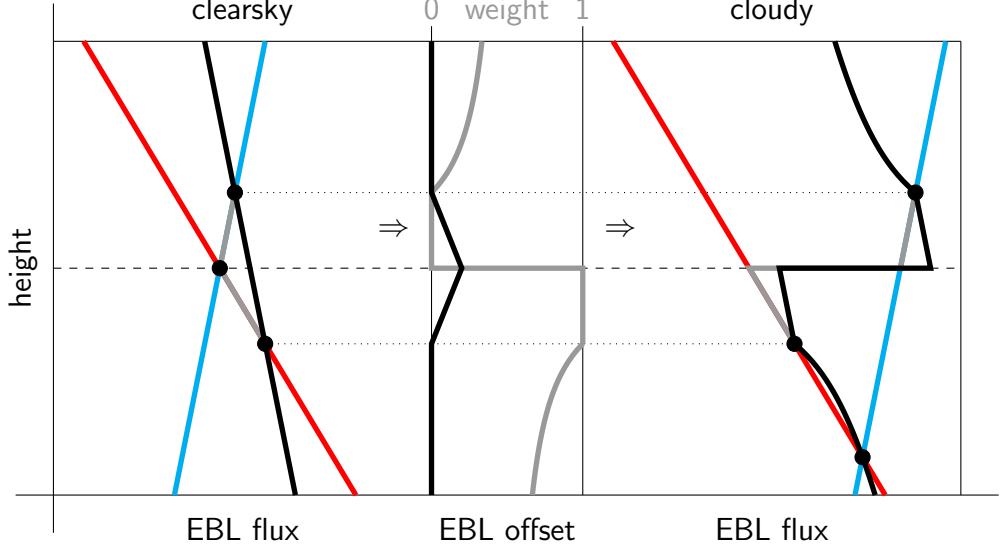
[16]This is the so-called bracketing hypothesis.

Figure 2.16: Oscillations due to bracketing in the vicinity of critical level, denoted by dashed horizontal line: blue – minimum EBL estimate; red – maximum EBL estimate; black – true clearsky EBL flux (left panel) or interpolated cloudy EBL flux (right panel). Central panel shows the bracketing offset (black) and truncated bracketing weights (grey; upper scale). Grey portions of EBL curves show the results obtained without bracketing offset, preventing overshoots but not oscillations.

these reasons, bracketing based on the *self-learning* algorithm was adopted in the ACRANEB2 scheme. The idea, illustrated on figure 2.16, is to calculate the true EBL flux and its minimum and maximum estimates in the absence of aerosols, clouds and surface reflection, and to diagnose bracketing weight and offset as:

$$\alpha^* = \frac{F_{\text{gases}}^{\text{EBL}} - F_{\text{gases}}^{\text{EBL,min}}}{F_{\text{gases}}^{\text{EBL,max}} - F_{\text{gases}}^{\text{EBL,min}}} \tag{2.41}$$

$$\alpha = \max(0, \min(\alpha^*, 1)) \tag{2.42}$$

$$\beta = F_{\text{gases}}^{\text{EBL}} - \left[(1 - \alpha)F_{\text{gases}}^{\text{EBL,min}} + \alpha F_{\text{gases}}^{\text{EBL,max}}\right] \tag{2.43}$$

Step (2.41) determines weight $\alpha^* \in (-\infty, +\infty)$. In order to prevent extrapolation, eventually leading to a numerical instability, the next step (2.42) truncates bracketing weight to interval $[0, 1]$. The last step (2.43) determines bracketing offset β in such way, that in the assumed idealized conditions equation (2.40) gives back the exact value $F_{\text{gases}}^{\text{EBL}}$.

Procedure (2.41)–(2.43) involves expensive quantity $F_{\text{gases}}^{\text{EBL}}$. Its calculation is simplified by the absence of any scattering and cloud geometry, but the cost remains *quadratic* in the number of layers L. This is because the true EBL flux across level $\tilde{l}$ is given by the double sum involving broadband transmissions between each pair of levels:

$$F_{\text{gases},\tilde{l}}^{\text{EBL}} = \sum_{m=1}^{l} \sum_{n=l+1}^{L} E_{mn}, \tag{2.44}$$
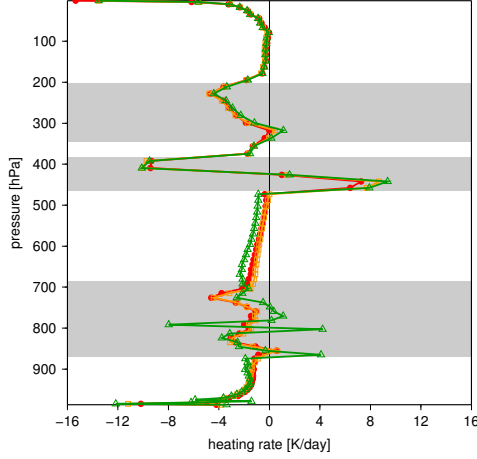
Figure 2.17: Longwave heating rates for the same case as on figure 2.13: red dots – the narrowband reference; yellow squares – the broadband scheme with random (H_2O, O_3) overlap; green triangles – the broadband scheme with random (H_2O, O_3) overlap and with unfiltered bracketing weights. Cloud layers are plotted in grey, maximum-random overlap between cloud layers is assumed. Reflective surface has emissivity $\epsilon_S = 0.966$.

Moreover, the broadband pair exchanges E_{kl} must take double temperature dependence of gaseous transmissions fully into account:

$$E_{kl} = \Delta\tau_{kl}\big|_{T_k}\sigma T_k^4 - \Delta\tau_{kl}\big|_{T_l}\sigma T_l^4 \qquad (2.45)$$

$$\Delta\tau_{kl} \equiv \tau(\tilde{k}, \tilde{l}-1) - \tau(\tilde{k}-1, \tilde{l}-1) - \tau(\tilde{k}, \tilde{l}) + \tau(\tilde{k}-1, \tilde{l}) \qquad k < l$$

For the success of the self-learning algorithm, it was necessary to remove spurious heating rate oscillations, appearing frequently in the vicinity of *critical levels*, where the minimum and maximum EBL estimates cross. One example of such oscillations is shown on figure 2.17, namely by the green curve between 700 and 900 hPa levels. Generating mechanism can be understood from figure (2.16). At the critical level, weight 2.41 is undefined. Near the critical level, the true EBL flux $F_{\text{gases}}^{\text{EBL}}$ usually lies *out of bracket* determined by its estimates $F_{\text{gases}}^{\text{EBL,min}}$ and $F_{\text{gases}}^{\text{EBL,max}}$. Here the truncation of bracketing weight to interval $[0, 1]$ takes place, producing non-zero offset β. At the critical level, truncated weight α jumps from 0 to 1. Applying it in cloudy case, where the critical level can be shifted or removed completely, leads to an abrupt jump of the interpolated EBL flux at original critical level. Corresponding heating rate, proportional to vertical derivative of the net flux, will then contain sharp peak, from each side accompanied by weaker peak in opposite direction.

Cure of the above mentioned problem lies in the proper filtering of bracketing weight α^*. Proposed treatment introduces filter with two tuning parameters $\hat{\alpha}$

and ΔF_{crit}:

$$\alpha^{**} = (1 - \hat{w})\alpha^* + \hat{w}\hat{\alpha} \tag{2.46}$$

$$\hat{w} = \frac{(\Delta F_{\text{crit}})^2}{(\Delta F_{\text{gases}}^{\text{EBL}})^2 + (\Delta F_{\text{crit}})^2} \tag{2.47}$$

$$\Delta F_{\text{gases}}^{\text{EBL}} = F_{\text{gases}}^{\text{EBL,max}} - F_{\text{gases}}^{\text{EBL,min}} \tag{2.48}$$

$$\alpha = \max(0, \min(\alpha^{**}, 1)) \tag{2.49}$$

$$0 \leq \hat{\alpha} \leq 1 \qquad \Delta F_{\text{crit}} > 0$$

Weight $\hat{w}$ is the function of EBL span $\Delta F_{\text{gases}}^{\text{EBL}}$. It was designed in such way that its complement $(1 - \hat{w})$ tends to zero faster than $\Delta F_{\text{gases}}^{\text{EBL}}$. This ensures that filtered bracketing weight α^{**} tends to value $\hat{\alpha}$ at the critical level. Strength of filter can be tuned by parameter ΔF_{crit}, which is the critical EBL span giving weight $\hat{w} = \frac{1}{2}$. Bracketing weight is finally truncated to interval $[0, 1]$, and bracketing offset β is determined as before by equation (2.43).

Optimal values of the tuning parameters $\hat{\alpha}$ and ΔF_{crit} were determined by fitting against the narrowband reference, using 480 atmospheric profiles extracted from the NWP model runs. Minimized quantity was the mean-square error of the net longwave fluxes over all layer interfaces. Fitting provided rather strong smoothing

$$\hat{\alpha} = 0.50 \qquad \Delta F_{\text{crit}} = 56\,\text{W m}^{-2}, \tag{2.50}$$

with the limit value $\hat{\alpha} = \frac{1}{2}$ appearing as very natural choice. Quality of the filter can be judged from yellow curve on figure (2.17). It removed not only oscillations of green curve inside low cloud layer, but also its cold bias between medium and low cloud layers.

There was one more issue with bracketing, illustrated on figure (2.18). With all non-random pair gaseous overlaps parameterized, the yellow true EBL flux delivered by broadband equations (2.44)–(2.45) is out of green-blue bracket in significant portion of profile (top left panel). Assuming random (H_2O, O_3) overlap removes this problem almost completely by shifting green minimum EBL estimate more to the right, without affecting much the yellow true EBL flux and its blue maximum estimate. This solution was therefore adopted by Geleyn et al. [2017], and it is still used in the operational configuration of model ALADIN/CHMI. Anyway, the proposed filtering procedure is so robust, that it gives reliable cloudy EBL flux even with non-random (H_2O, O_3) overlap included (top right panel), showing only small deterioration with respect to the case when this overlap is excluded (bottom right panel). Proximity of yellow curves to the red narrowband reference in cloudy case (right column) proves validity of bracketing hypothesis.

Finally, figure (2.19) demonstrates accuracy of bracketing in terms of heating rates, showing comparable error of configurations with parameterized non-random (H_2O, O_3) overlap (yellow), and with random (H_2O, O_3) overlap (green).[17] In the clearsky case (left), absolute error of both configurations remains below $0.2\,\text{K/day}$

---

[17]One should keep in mind that the longwave heating rate error is contributed by all three CTS, EWS and EBL components.
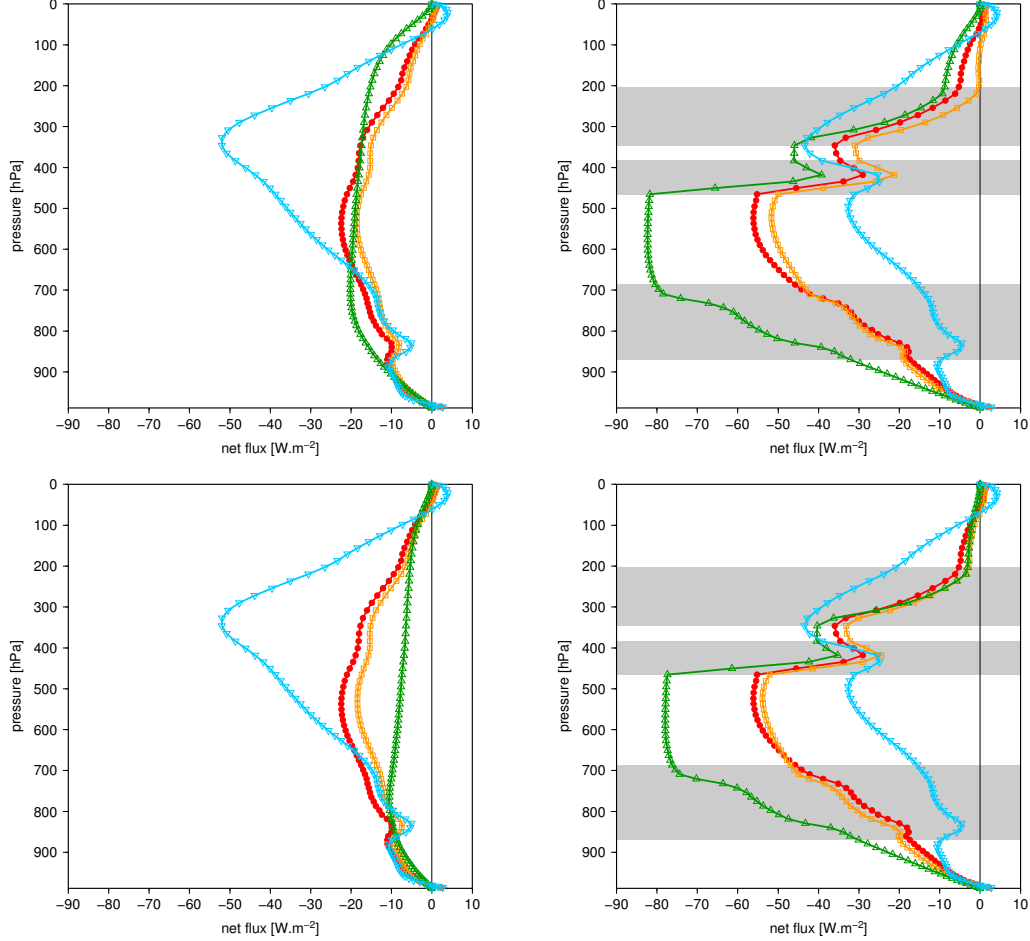
Figure 2.18: EBL fluxes for the same case as on figure 2.13: red dots – the narrowband reference; yellow squares – true EBL flux (left) or interpolated EBL flux (right) calculated by the broadband scheme; green triangles – minimum EBL estimate; blue inverse triangles – maximum EBL estimate. Cloud layers are plotted in grey, maximum-random overlap between cloud layers is assumed. **Top:** The broadband scheme with parameterized non-random pair gaseous overlaps. **Bottom:** The broadband scheme with random (H_2O, O_3) overlap. **Left:** Clearsky case with non-reflective surface *determining* the bracketing weights and offsets. **Right:** Cloudy case with reflective surface *applying* the bracketing weights and offsets. Surface emissivity is $\epsilon_S = 0.966$, corresponding to the longwave reflectivity 3.4%.
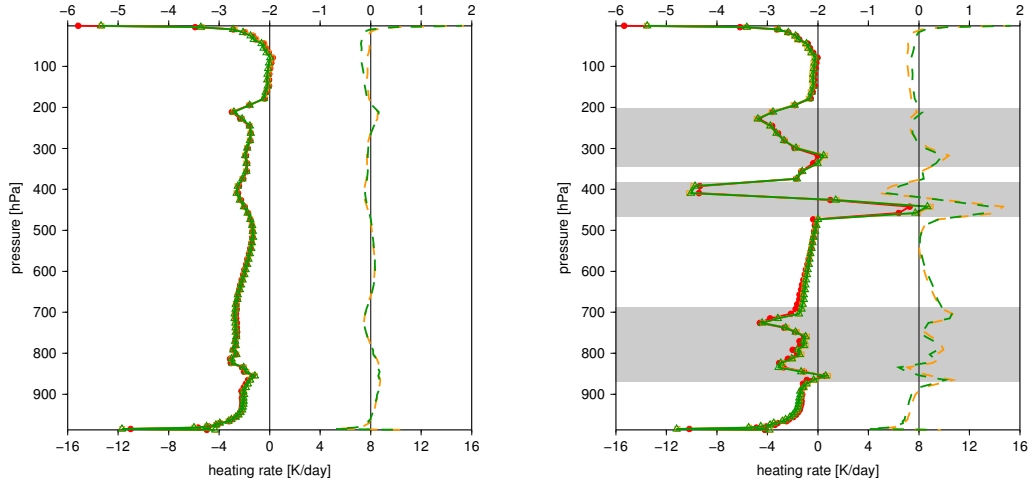
Figure 2.19: Longwave heating rates for the same case as on figure 2.13: red dots – the narrowband reference; yellow squares – the broadband scheme with parameterized non-random pair gaseous overlaps; green triangles – the broadband scheme with random (H_2O, O_3) overlap. Dashed lines denote deviation from the narrowband reference (upper scale). Cloud layers are plotted in grey, maximum-random overlap between cloud layers is assumed. Reflective surface has emissivity $\epsilon_S = 0.966$. **Left:** Clearsky case. **Right:** Cloudy case.

across the atmosphere, the only exceptions being at the top and bottom of the model domain, where it reaches 2 and $0.8\,\mathrm{K/day}$ respectively. In the cloudy case (right), absolute error at the bottom of the model domain increases to $1\,\mathrm{K/day}$, and inside medium cloud layer it reaches maximum value $1.8\,\mathrm{K/day}$. Outside clouds it remains below $0.5\,\mathrm{K/day}$. Parameterized non-random (H_2O, O_3) overlap is beneficial in the clearsky case, reducing error above $200\,\mathrm{hPa}$ level thanks to improved EWS flux. In the cloudy case, however, this advantage is lost due to poorer minimum EBL estimate, deteriorating bracketed EBL flux. Hybrid solution excluding non-random (H_2O, O_3) overlap only in EBL calculations was not implemented, since its anticipated gain in the stratosphere is only modest, surely smaller than uncertainty of the narrowband reference due to Curtis-Godson approximation.

The proposed self-learning algorithm makes the bracketing technique both adequately accurate and independent of vertical resolution. Disadvantage is its high computational cost, quadratic in the number of layers L. Nevertheless, slow evolution of bracketing weights and offsets enables their intermittent update, cutting the cost of longwave computations in the NWP environment *dramatically*. The idea is elaborated in section 2.7.

2.7 Selective intermittency

As was mentioned in the Introduction, there are conflicting requirements imposed on the radiative transfer schemes used in the NWP models. On the one hand, high accuracy alias realism of delivered radiative fluxes is desired. On the other hand, there are severe limitations on the computational cost of the scheme.

Growing computing resources are typically spent on increase of model resolution, but also on more advanced data assimilation techniques or ensemble forecasting. Even in deterministic framework, radiation scheme has to share the available resources with other physical parameterizations and with model dynamics. Simple illustration can be given here: Operational model ALADIN/CHMI currently has a computational domain of 529×421 points, with horizontal mesh size 4.7 km and time-step 180 s. It means that within one-hour integration, radiation scheme is called for more than 4 million model columns, each having 87 vertical levels. Yet, real time of one-hour integration must not exceed about one minute. Radiation consumes roughly 20% of that, i.e. 4 million calls of radiation scheme must be accomplished in about 12 seconds of real time. If the calls were performed sequentially, each would have to be ready in 3 microseconds![18]

There are several ways how to reduce computational cost of the radiative transfer parameterization in the NWP model. For an overview, the reader is kindly referred to the introduction of Schomburg et al. [2012]. The simplest strategy, still widely used despite its *serious* shortcomings, performs radiative calculations with reduced spatial and/or temporal resolutions. The use of reduced radiation grid implies smoothing of input fields, connected to the loss of high resolution information. Output radiative fluxes have to be interpolated back to full model resolution. Missing small scales in radiation outputs are then likely source of inconsistencies, putting in question the investments in high resolution forecast.[19] Even if predictability of small scales is limited, their model description should be *consistent*, in order to prevent false sources/sinks that can contaminate also larger scales. The inconsistency problem can be especially severe in the coastal areas, where there are large differences in surface albedo or temperature between land and sea. It can be mitigated by approximate radiation updates proposed by Hogan and Bozzo [2015]. Still, their cure does not address the error coming from inhomogeneities of the cloud field on scales resolved in the model but not in reduced radiation grid.

Reduced frequency of radiative calculations, approach orthogonal to reduced spatial resolution, is also not problem-free. The broadband fluxes calculated in full radiation time-step must be stored for use in subsequent model time-steps until the next radiation update. Period between two radiation updates is so-called intermittency window. It is typically 1 h, in ensemble forecasting sometimes even 3 h. Within intermittency window, the net longwave fluxes are assumed constant, while the net shortwave fluxes must be adjusted to evolving sun elevation. The simplest possibility is to rescale the shortwave fluxes by the ratio of actual to average[20] cosine of solar zenith angle μ_0, accounting solely for the change in solar income at the TOA. Manners et al. [2009] introduced a more elaborate approach, correcting the net surface flux also due to changing optical path of direct solar ray. Hogan and Hirahara [2016] further addressed the double occurrence of μ_0 in calculation of solar fluxes. Using different temporal averaging for each occurrence, they were able to significantly reduce the stratospheric temperature

---

[18]Integration is actually done on 16 vector processors of NEC SX-9 supercomputer, using OpenMP parallelization with 16 threads.

[19]Use of reduced radiation grid would be justified if the *small-scale* component of radiative heating/cooling was negligible. Given the spatial variability of the cloud field, combined with its strong radiative effect, this is very unlikely.

[20]The average value is calculated over the radiation time-step.

bias even for radiation time-step 3 h. Fundamental problem, common to all above described approaches with prolonged radiation time-step, is the 'frozen' radiative impact of clouds within intermittency window. Model cloud evolution on shorter time scales is thus ignored by radiation, leading to severe inconsistencies when the cloud scene changes rapidly. In the longwave spectrum, additional error arises from 'frozen' Planck factors, ignoring the temperature evolution within intermittency window. Because of the 'frozen' radiative response, the above described strategies will be referred to as *full intermittency*.

Computational cost of the old ACRANEB scheme was relatively low, enabling it to be called at every model grid-point and time-step. Developments described in sections 2.1–2.6 have made the ACRANEB2 scheme much more accurate, but also too expensive to be used with unreduced spatial *and* temporal resolutions. Full interaction with clouds was recognized as a necessity. Decision was made to use unreduced spatial grid, and to save computational costs by updating gaseous optical depths intermittently. This strategy, referred to as *selective intermittency*, can be afforded thanks to the broadband character of the ACRANEB2 scheme. For the schemes with finer spectral division, required memory storage would be prohibitive.

Key features of selective intermittency are the cloud optical properties updated at every model time-step, with subsequent solving of the delta-two-stream and adding system. Logic of this choice comes from the fact that while gaseous optical depths are the most costly component of radiative calculations, they evolve on the time scales of hours rather than minutes. This is because unlike clouds, gaseous composition of the atmosphere varies slowly, even in the presence of water phase changes. Illustration is given on figure 2.20, where the top left panel shows the point evolution of water columns during passage of the waving cold front.[21] While the hourly change of precipitable water vapour (red) does not exceed ∼20%, for the cloud liquid and ice water paths (dark blue and blue) it can reach 2–3 orders of magnitude. The top right panel shows that the most abrupt changes in the cloud condensates are related to the appearance of deep convective clouds.

The ACRANEB2 scheme applies selective intermittency in both shortwave and longwave spectral intervals. While in the shortwave case only modest computational savings are achieved (see chapter 10 of Mašek et al. [2016]), in the longwave case selective intermittency is *absolutely necessary* (see chapter 8 of Geleyn et al. [2017]), making the ACRANEB2 scheme affordable. For this reason, only the longwave treatment is examined here.

Gaseous optical depth of model layer depends on its composition, thermodynamic state and mass. Selective intermittency, 'freezing' the broadband gaseous optical depths within intermittency window, is justified by the following facts:

- Gaseous composition of the atmosphere evolves slowly. Even in frontal situations with changing air mass, its hourly update is sufficient.

- The pressure within one hour can change by several per mille, while for

---

[21]Evolution of water columns was extracted from experimental ALADIN run. Precipitable water vapour during early forecast is likely to be overestimated, since the values over $40 \, \mathrm{kg/m^2}$ are observed very rarely in mid-latitude atmospheric soundings (D. Rýva, personal communication, 2017).
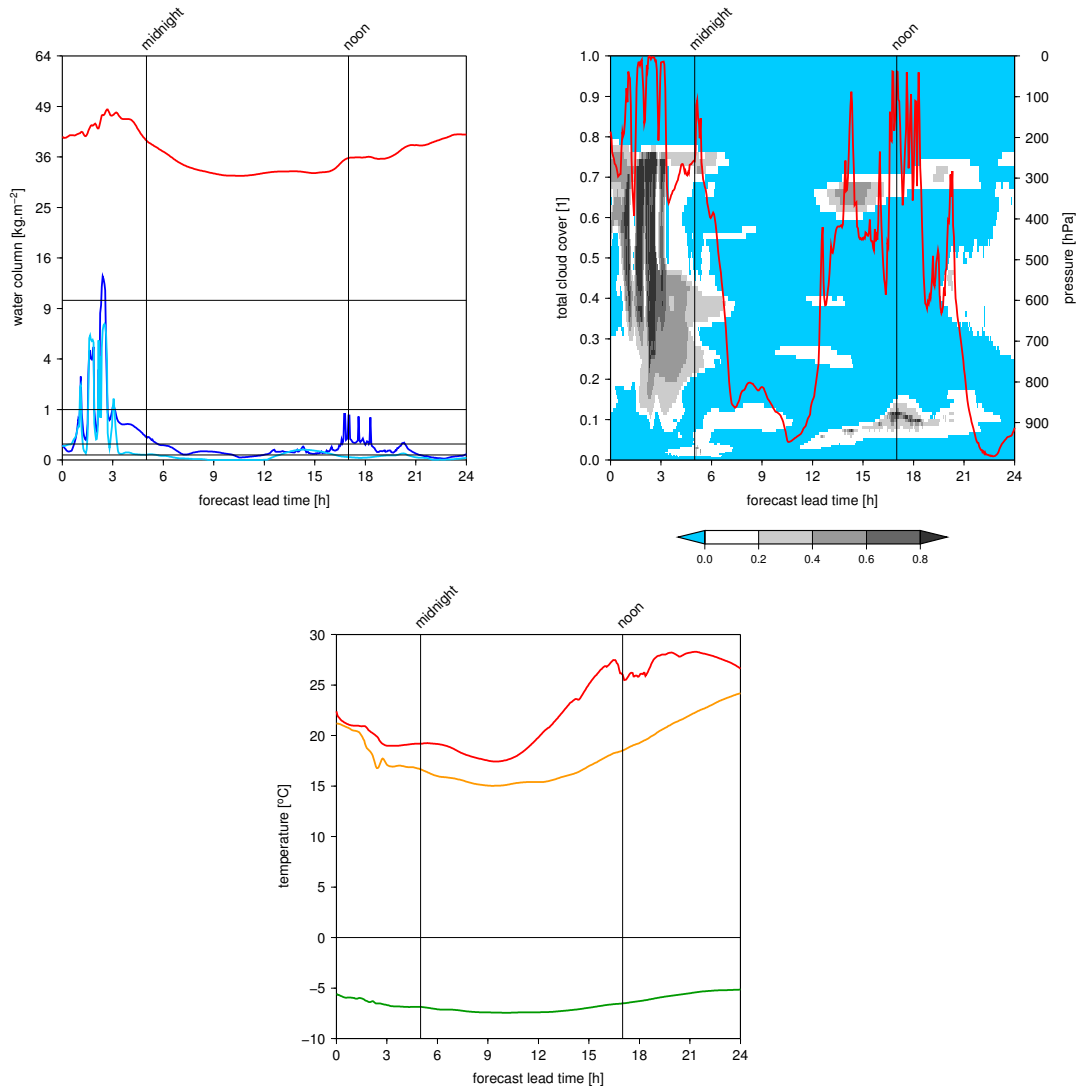
Figure 2.20: Evolution of water columns, cloud cover and temperature in Prague during passage of the waving cold front. Results are extracted from experimental ALADIN run starting on 01-Jul-2012 at 18:00 UTC. **Top left:** red – precipitable water vapour; dark blue – liquid water path; blue – ice water path. Thin horizontal lines denote values 0.01, 0.1, 1 and 10 kg/m^2. **Top right:** red – total cloud cover (left scale); colour filling – layer cloud fractions (right scale and colour palette). Clear sky is blue, overcast layers are dark grey. **Bottom:** red – surface temperature; yellow – mean atmospheric temperature below 850 hPa level; green – mean atmospheric temperature below 200 hPa level. Mean temperatures are mass-weighted.

thermodynamic temperature the change is limited to few per cent. Such small variations affect *monochromatic* gaseous transmissions only weakly and need not be considered. Much more important is the vertical variation across the troposphere and stratosphere, being 3 orders of magnitude for pressure, and reaching easily $100\,\mathrm{K}$ for temperature.

- In the longwave case, *broadband* gaseous transmissions depend also on the temperature of emitting body. Here again, the vertical variation of the temperature is much more substantial than its hourly evolution.

- The mass of model layers changes most quickly near the surface, where the hybrid eta-coordinate reduces to sigma-coordinate, and the layer mass becomes proportional to the surface pressure. Its relative change within one hour is thus at most several per mille and can be neglected.

From the above listed facts it follows that hourly temperature evolution can be ignored in the broadband layer gaseous transmissions, entering the *optical factors*. Longwave exchanges, however, contain also strongly temperature dependent *Planck factors*, and these should be updated at every model time-step. Selective intermittency enables to do so, together with inclusion of actual clouds in the optical factors.

Selective intermittency in the longwave case relies on one more fact, verified a posteriori:

- Evolution of the bracketing weights and offsets, needed for determination of the EBL flux, is also slow. It is sufficient to update them using three-hourly footing, *regardless* of the model time-step.

This last fact is crucial for a scalability of longwave computations with increasing model resolution. It makes the cost of single ACRANEB2 call *essentially linear* in the number of layers L, even though calculation of the bracketing weights and offsets remains quadratic in L. This is because the horizontal, vertical and temporal model resolutions are interconnected, being kept roughly proportional. Computational time of the longwave ACRANEB2 scheme in a single model column during 3 hour time period is given by

$$t_{\mathrm{rad}} = N \cdot (C_0 \cdot L) + 3C_1 \cdot L + C_2 \cdot L^2, \tag{2.51}$$

where $C_0 \cdot L$ is the cost of single radiation call without update of the gaseous transmissions, bracketing weights and offsets, N is the number of model time-steps within 3 hours, $C_1 \cdot L$ is the cost of single update of the gaseous transmissions, and $C_2 \cdot L^2$ is the cost of single update of the bracketing weights and offsets. Factor 3 in the second term is due to the fact that the longwave gaseous transmissions are updated hourly. Now, since there is $N \propto L$, the first term grows quadratically with L, i.e. in the same way as the last term, giving $t_{\mathrm{rad}} \propto L^2$. For the radiation scheme with the cost of single call truly quadratic in L, computational time $t_{\mathrm{rad}} \propto L^3$ would result. Keeping $t_{\mathrm{rad}} \propto L^2$ is the key achievement of the longwave ACRANEB2 developments, breaking the computational barrier of the absorptivity-emissivity approach. Moreover, the longwave scattering is included with no extra effort.

The longwave ACRANEB2 scheme uses two-level selective intermittency, tailored for usage with the NER decomposition and bracketing. Four sets of the broadband gaseous optical depths are updated hourly – those for calculation of the CTS, EWS, minimum and maximum EBL fluxes. The bracketing weights and offsets are updated three-hourly. Altogether, there are six 3D global arrays that have to be stored in the memory, so that they can be reused in subsequent partial radiative time-steps. In these time-steps, actual cloud optical properties are determined and used to recalculate the optical factors, while actual temperatures are used in Planck factors. Eight solvings of the delta-two-stream and adding system are required, as explained in section 6.7 of Geleyn et al. [2017].

In section 8 of Geleyn et al. [2017], cost and accuracy of the proposed intermittency strategy is evaluated in the NWP model, including the feedbacks between radiation and other fields. It demonstrates that compared to the non-intermittent run with $3\,\mathrm{min}$ time-step, use of $1\,\mathrm{h}/3\,\mathrm{h}$ selective intermittency cuts the cost of longwave computations by factor 20, while the error remains comparable to the full intermittency with $6\,\mathrm{min}$ window, which however cuts the cost only by factor 2.

In this thesis only the accuracy aspect of longwave intermittency is examined. The ACRANEB2 scheme was run in an offline mode, fed by atmospheric profiles extracted for single point from 24 hour integration of the NWP model ALADIN. This approach excludes feedbacks, on the other hand it enables to calculate also the narrowband reference, which would not be possible in the NWP model.[22] Evolution of selected quantities is shown on figure 2.20. Case of waving cold front was selected purposely, having abrupt changes in the cloud field, with cloud cover ranging from overcast to almost clear. Simulations assumed maximum-random cloud overlap. Surface emissivity was 0.966, model time-step was again $3\,\mathrm{min}$.

Figure 2.21 shows evolution of the longwave fluxes leaving the atmosphere. Non-intermittent ACRANEB2 run (red) is compared against the narrowband reference (black), in order to isolate error of the broadband approach. The downward flux at the surface is systematically underestimated, with absolute error remaining below $10\,\mathrm{W/m^2}$. Error of the upward flux at the TOA is better balanced, staying within $15\,\mathrm{W/m^2}$. Such accuracy is fine for the short range NWP, but as was mentioned in the Introduction, it would be insufficient for climate simulations. Underestimated downward flux at the surface can be attributed to the overestimated broadband gaseous transmissions, since the emission of more transparent atmosphere is weaker. This conclusion is supported also by the fact that in periods with considerable low cloud cover, underestimation of the downward flux at the surface is reduced. The upward flux at the TOA is not biased, here the lower gaseous emission is compensated by more surface emitted radiation transmitted to space.

Remaining curves on figure 2.21 compare two intermittent ACRANEB2 runs against the non-intermittent run, in order to evaluate error due to intermittency alone. Use of $1\,\mathrm{h}$ full intermittency (yellow) leads to enormous error in the upward flux at the TOA, especially between integration hours 3 and 4, where the deep convective cloud quickly fades out and the flux becomes underestimated

---

[22]Running the narrowband reference for 481 atmospheric profiles on a $3\,\mathrm{GHz}$ PC took about one hour.
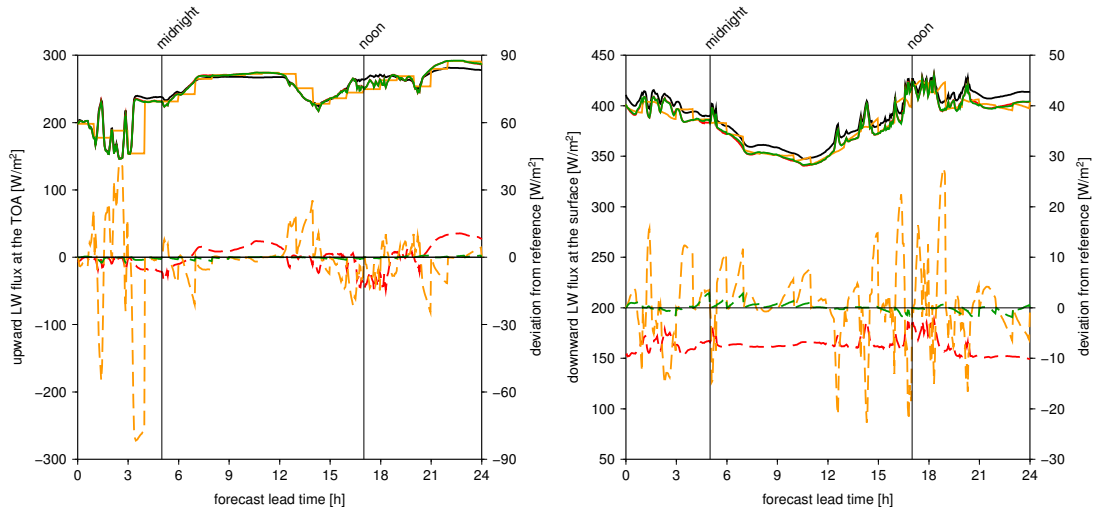
Figure 2.21: Evolution of the longwave fluxes leaving the atmosphere for the same case as on figure 2.20. Solid lines denote fluxes (left scale): black – the narrowband reference; red – the ACRANEB2 scheme with no intermittency; yellow – the ACRANEB2 scheme with 1h full intermittency; green – the ACRANEB2 scheme with 1h/3h selective intermittency. Dashed lines denote flux errors (right scale): red – the ACRANEB2 scheme with no intermittency against the narrowband reference; yellow – the ACRANEB2 scheme with 1h full intermittency against no intermittency; green – the ACRANEB2 scheme with 1h/3h selective intermittency against no intermittency. **Left:** Upward longwave flux at the TOA. **Right:** Downward longwave flux at the surface.
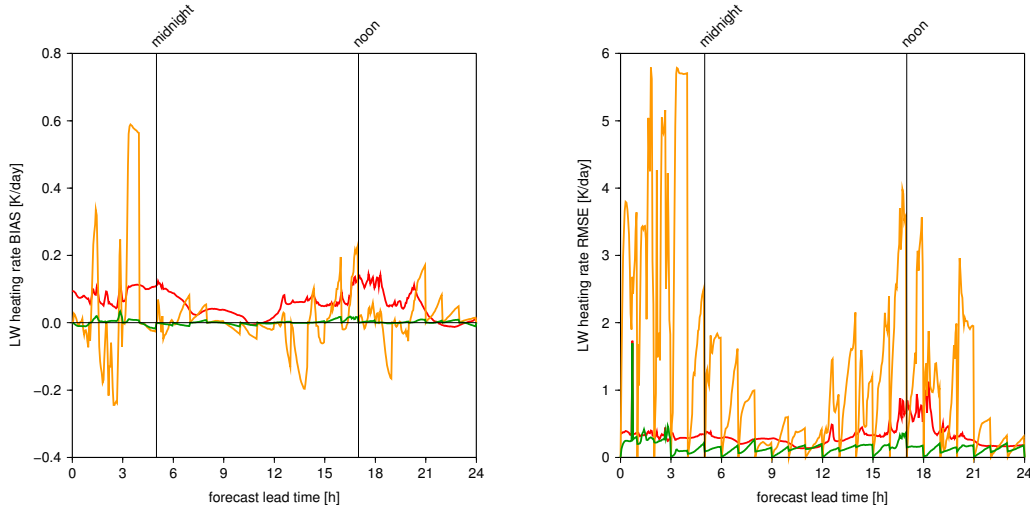
Figure 2.22: Evolution of the longwave heating rate scores for the same case as on figure 2.20, calculated over the model column: red – the ACRANEB2 scheme with no intermittency against the narrowband reference; yellow – the ACRANEB2 scheme with 1h full intermittency against no intermittency; green – the ACRANEB2 scheme with 1h/3h selective intermittency against no intermittency. **Left:** Mass-weighted longwave heating rate bias **Right:** Mass-weighted longwave heating rate RMSE.

by $80 \, \text{W/m}^2$. This is because at hour 3 the cold cloud top below $200 \, \text{hPa}$ level filled the gridbox, sending little longwave radiation to space. In subsequent hour the horizontal extent of cloud top reduced, letting more energetic longwave radiation emitted by warmer lower layers to escape. Full intermittency, 'freezing' the net longwave flux at the TOA,[23] cannot capture this evolution until the next radiative update at integration hour 4. Error of the downward flux at the surface is somewhat smaller, staying within $30 \, \text{W/m}^2$, but its evolution is also quite abrupt, especially in periods with quickly varying total cloud cover.[24] On the other hand, use of $1 \, \text{h}/3 \, \text{h}$ selective intermittency (green) introduces only small error in the upward and downward fluxes, staying within few W/m^2 from the non-intermittent ACRANEB2 run.

Figure 2.22 completes the picture by showing evolution of the longwave heating rate scores, calculated over the model column using mass weighting. It clearly confirms superiority of selective intermittency over the full one. It also shows that systematic underestimation of downward longwave flux at the surface, seen for non-intermittent ACRANEB2 run, results in the insufficient atmospheric cooling alias warm bias.

Global picture can be obtained by inspecting table 2.2, giving overall scores for the longwave fluxes leaving the atmosphere, as well as for the longwave heating rates of atmospheric layers. Two important observations can be made. First, selective intermittency is practically bias-free, for both fluxes and heating rates.

---

[23]And thus also longwave upward flux, since the longwave downward flux at the TOA is zero.

[24]Evolution of downward longwave flux at the surface is not piecewise constant, since it is related to 'frozen' net flux F_S by $F_S^{\downarrow} = F_S/\epsilon_S + \sigma T_S^4$, where the surface temperature T_S evolves (see bottom panel on figure 2.20).

longwave upward flux at the TOA [W/m²]				
scheme, intermittency	reference	BIAS	RMSE	SDEV
BB	NB	0.46	5.60	5.58
BB, full 1h	BB	−3.02	17.30	17.04
BB, selective 1h/3h	BB	−0.17	0.54	0.51
longwave downward flux at the surface [W/m²]				
scheme, intermittency	reference	BIAS	RMSE	SDEV
BB	NB	−7.48	7.65	1.58
BB, full 1h	BB	0.79	7.55	7.51
BB, selective 1h/3h	BB	0.05	0.82	0.82
longwave heating rate of atmospheric layers [K/day]				
scheme, intermittency	reference	BIAS	RMSE	SDEV
BB	NB	0.06	0.36	0.36
BB, full 1h	BB	0.02	1.92	1.92
BB, selective 1h/3h	BB	0.00	0.18	0.18

Table 2.2: Overall longwave scores during passage of the waving cold front in Prague. The period is from 01-Jul-2012 18:00 UTC to 02-July-2012 18:00 UTC, the model time-step was 180 s. NB denotes the narrowband reference, BB is the broadband scheme, eventually with 1h full intermittency or with 1h/3h selective intermittency. First line in each section is the error of the broadband approach, second and third lines are the errors of given intermittent strategies.

It therefore does not increase bias due to the broadband approach. Second, random error due to selective intermittency, represented by its standard deviation (SDEV), is at most half that of non-intermittent ACRANEB2 run. Random error due to full intermittency is one order of magnitude larger, exceeding random error due to the broadband approach several times.

When intermittency is used in the NWP model run, feedbacks between radiation and other fields will cause drift from the non-intermittent solution.[25] Error resulting from the intermittency strategy will thus be larger than listed in table 2.2. One can apply factor 2 as a very rough estimate, yielding the longwave heating rate SDEV due to selective intermittency 0.36 K/day, which is the same value as SDEV due to the broadband approach. If these two errors were uncorrelated, resulting SDEV of 1 h/3 h selective intermittency with respect to a hypothetical NWP run using the narrowband reference would be around 0.5 K/day, which is adequate result for cloudy scene. Overall systematic error would remain below 0.1 K/day.

Comparable errors coming from the stand-alone radiation scheme and from intermittency strategy are an important achievement of the longwave ACRANEB2 design, ensuring an optimal share of the computational resources. It can be put in contrast with the mainstream approach, where the very accurate results of the correlated k-distribution method are significantly deteriorated by the use of full intermittency, possibly combined with reduced radiation grid.

---

[25]The drift is small in the initial stage of integration and it grows in time. The least favourable situation is in global models, while in the limited area models the growth is restricted by lateral boundary coupling.

Conclusion

Described above in this thesis are the author's main contributions to the development of the ACRANEB2 radiation scheme. The goal of this development was to provide a sound alternative to the mainstream approach, eliminating its structural deficiency arising from the use of correlated k-distribution method, which is very accurate but too costly to be used at every model grid-point and time-step. The starting point was the old ACRANEB scheme, whose key choices – the broadband approach with single shortwave and single longwave spectral intervals, full cloud-radiation interaction, and NER decomposition with bracketing – remained unchanged. A significant effort was put into the improvement of the basic building blocks – gaseous transmissions and cloud optical properties. Several important effects not accounted for previously were identified and successfully parameterized, including the non-random spectral overlap between different gases and the double temperature dependence of the longwave gaseous transmissions. The band approach was extended to cloud treatment, where the optical saturation of shortwave cloud absorption was parameterized in a fully scattering environment. In the longwave spectrum, the accuracy of the bracketing technique was significantly increased by replacing the statistical fit with a self-learning algorithm. The higher computational cost of the improved gaseous transmissions was compensated for by their intermittent update, allowing the full cloud-radiation interaction to be retained. The memory requirements for the intermittent storage were kept reasonable due to the broad spectral division used. Selective intermittency was applied also to bracketing weights and offsets, ensuring the essentially linear scalability of longwave computations with respect to the number of vertical levels.

There were also additional developments not mentioned in this thesis. In the end, the only ACRANEB components that remained untouched were the solvers of the delta-two-stream and adding system, and the aerosol treatment. Many new ACRANEB2 components are based on some sort of fit. Their reliability and accuracy comes from two design principles. First, the functional shape of the fit is physically motivated whenever possible, ensuring the correct asymptotic behaviour or at least physically meaningfull values. Second, a small to moderate number of fitting parameters minimizes the risk of overfitting and enables the use of the non-linear least-squares method. The minimized cost function may be of arbitrary shape, since the fitting parameters do not have to enter into it in a linear way. This allows for the minimizing of error directly in the desired quantity.

With all the above mentioned improvements, the ACRANEB2 scheme with its selective intermittency has become competitive with the mainstream approach that combines the correlated k-distribution method with full intermittency. Of course, in a stand-alone mode the broadband approach is necessarily less accurate than the correlated k-distribution method, the accuracy of which is provided by its higher spectral resolution. On the other hand, in the NWP environment the error originating from parameterized, spectrally unresolved phenomena is counterbalanced by the full cloud-radiation interaction, made possible by selective intermittency. This results in a much better balance between errors coming from

the radiation scheme itself and from the intermittency strategy, than can be obtained by the mainstream approach.

The ACRANEB2 concept was explained in two peer-reviewed articles. The scheme became part of ALARO-1 version A, operational at CHMI beginning in January 2015. Further refinements were incorporated into ALARO-1 version B, which became operational in September 2016. At present, ALARO-1 with ACRANEB2 radiation is used by eight ALADIN countries (Belgium, Croatia, Czech Republic, Hungary, Poland, Slovakia, Slovenia and Turkey), further confirming the vitality of the concept.

The broadband approach definitely has its limits in terms of accuracy, some of which seem to have been reached during ACRANEB2 developments. The most important of these is related to the assumption of a spectrally flat surface albedo. In extreme cases, it can yield a heating rate error exceeding that coming from the broadband gaseous transmissions. Here probably the only cure is to opt for two or more shortwave intervals, which would be a sidestepping of the original ACRANEB concept. Another limitation is met in the stratosphere, where the two-parameter Curtis-Godson approximation does not perform well with the ozone. A solution within the band framework would be to use a more elaborated three-parameter scaling. Yet another limitation prevails in the mesosphere, arising from the broadband treatment of the Voight line shape applied a posteriori. The last two problems are not very acute in short range NWP, where the impact of the higher atmosphere on weather is weak.

It was also seen that improving the broadband scheme resembles the opening of Matryoshka, since more and more spectrally unresolved effects must be parameterized, increasing the complexity of the scheme. Fortunately, for reaching the desired accuracy it was sufficient to include primary effects such as non-random pair gaseous overlaps, and optical saturation of Rayleigh scattering and of shortwave cloud absorption, neglecting their cross-interactions. Some phenomena, such as the radiative effect of falling hydrometeors, are still ignored in the ACRANEB2 scheme and there is no urgent need to include them. This is because the main limitations now come from the quality of cloud inputs and from the climatological treatment of aerosols, i.e. from factors lying outside the radiation scheme.

The main challenge in the coming years is the effects of 3D radiation. These are unimportant for scales larger than 10 km, where the vertical transfer clearly dominates, but this is no longer true for scales below 1 km. For intermediate resolutions, which are the domain of contemporary NWP, some unresolved 3D effects can be parameterized. The problem starts at the moment when the 3D effects become resolved, and a 1D radiation scheme based on a plane-parallel approximation is not able to capture them. Addressing the problem on current massively parallel computing platforms is a tough challenge, since the implicitness of truly 3D solvers spoils scalability, while the slow convergence of explicit Monte Carlo simulations prevents their usage in operational NWP. Partial solutions, such as freezing the radiation grid at resolutions where the 3D effects can still be parameterized, create inconsistencies with the finest model scales. Sooner or later the problem will have to be addressed properly, since beyond a certain point the use of plane-parallel approximation produces errors comparable to those coming from the neglected fine scales.

Bibliography

A. Arking and K. Grossman. The influence of line shape and band structure on temperatures in planetary atmospheres. *J. Atmos. Sci.*, 29:937–949, 1972. doi: 10.1175/1520-0469(1972)029⟨0937:TIOLSA⟩2.0.CO;2.

K. Bignell, F. Saiedy, and P. A. Sheppard. On the atmospheric infrared continuum. *J. Opt. Soc. Am.*, 53:466–479, 1963. doi: 10.1364/JOSA.53.000466.

K. J. Bignell. The water-vapour infra-red continuum. *Q. J. R. Meteorol. Soc.*, 96:390–403, 1970. doi: 10.1002/qj.49709640904.

D. E. Burch. Continuum absorption by atmospheric H_2O. *Proc. SPIE*, 277:28–39, 1981. doi: 10.1117/12.931898.

S. A. Clough, F. X. Kneizys, and R. W. Davies. Line shape and the water vapor continuum. *Atmos. Res.*, 23:229–241, 1989. doi: 10.1016/0169-8095(89)90020-3.

A. R. Curtis. Discussion of "A statistical model for water-vapour absorption". *Q. J. R. Meteorol. Soc.*, 78:638–640, 1952. doi: 10.1002/qj.49707833820.

R. G. Ellingson and Y. Fouquart. The intercomparison of radiation codes in climate models: An overview. *J. Geophys. Res.*, 96:8925–8927, 1991. doi: 10.1029/90JD01618.

Y. Fouquart, B. Bonnel, and V. Ramaswamy. Intercomparing shortwave radiation codes for climate studies. *J. Geophys. Res.*, 96:8955–8968, 1991. doi: 10.1029/90JD00290.

Q. Fu and K. N. Liou. On the correlated k-distribution method for radiative transfer in nonhomogeneous atmospheres. *J. Atmos. Sci.*, 49:2139–2156, 1992. doi: 10.1175/1520-0469(1992)049⟨2139:OTCDMF⟩2.0.CO;2.

J.-F. Geleyn and A. Hollingsworth. An economical analytical method for the computation of the interaction between scattering and line absorption of radiation. *Contrib. Atmos. Phys.*, 52:1–16, 1979.

J.-F. Geleyn, J. Mašek, R. Brožková, P. Kuma, D. Degrauwe, G. Hello, and N. Pristov. Single interval longwave radiation scheme based on the net exchanged rate decomposition with bracketing. *Q. J. R. Meteorol. Soc.*, 143:1313–1335, 2017. doi: 10.1002/qj.3006.

W. L. Godson. The evaluation of infrared-radiative fluxes due to atmospheric water vapour. *Q. J. R. Meteorol. Soc.*, 79:367–379, 1953. doi: 10.1002/qj.49707934104.

R. M. Goody. A statistical model for water-vapour absorption. *Q. J. R. Meteorol. Soc.*, 78:165–169, 1952. doi: 10.1002/qj.49707833604.

J. E. Hansen. Exact and approximate solutions for multiple scattering by cloudy and hazy planetary atmospheres. *J. Atmos. Sci.*, 26:478–487, 1969. doi: 10.1175/1520-0469(1969)026⟨0478:EAASFM⟩2.0.CO;2.

Harshvardhan and M. D. King. Comparative accuracy of diffuse radiative properties computed using selected multiple scattering approximations. *J. Atmos. Sci.*, 50:247–259, 1993. doi: 10.1175/1520-0469(1993)050⟨0247:CAODRP⟩2.0. CO;2.

L. G. Henyey and J. L. Greenstein. Diffuse radiation in the galaxy. *Astrophys. J.*, 93:70–83, 1941.

R. J. Hogan. The full-spectrum correlated-k method for longwave atmospheric radiative transfer using an effective Planck function. *J. Atmos. Sci.*, 67:2086–2100, 2010. doi: 10.1175/2010JAS3202.1.

R. J. Hogan and A. Bozzo. Mitigating errors in surface temperature forecasts using approximate radiation updates. *J. Adv. Model. Earth Syst.*, 7:836–853, 2015. doi: 10.1002/2015MS000455.

R. J. Hogan and S. Hirahara. Effect of solar zenith angle specification in models on mean shortwave fluxes and stratospheric temperatures. *Geophys. Res. Lett.*, 43:482–488, 2016. doi: 10.1002/2015GL066868.

R. J. Hogan and A. J. Illingworth. Deriving cloud overlap statistics from radar. *Q. J. R. Meteorol. Soc.*, 126:2903–2909, 2000. doi: 10.1002/qj.49712656914.

Y. X. Hu and K. Stamnes. An accurate parameterization of the radiative properties of water clouds suitable for use in climate models. *J. Climate*, 6:728–742, 1993. doi: 10.1175/1520-0442(1993)006⟨0728:AAPOTR⟩2.0.CO;2.

M. J. Iacono, J. S. Delamere, E. J. Mlawer, M. W. Shephard, S. A. Clough, and W. D. Collins. Radiative forcing by long-lived greenhouse gases: Calculations with the AER radiative transfer models. *J. Geophys. Res.*, 113:8 pp, 2008. doi: 10.1029/2008JD009944.

J. H. Joseph, W. J. Wiscombe, and J. A. Weinman. The delta-Eddington approximation for radiative flux transfer. *J. Atmos. Sci.*, 33:2452–2459, 1976. doi: 10.1175/1520-0469(1976)033⟨2452:TDEAFR⟩2.0.CO;2.

J. R. Key, P. Yang, B. A. Baum, and S. L. Nasin. Parameterization of shortwave ice cloud optical properties for various particle habits. *J. Geophys. Res.*, 107: 10 pp, 2002. doi: 10.1029/2001JD000742.

M. D. King and Harshvardhan. Comparative accuracy of selected multiple scattering approximations. *J. Atmos. Sci.*, 43:784–801, 1986. doi: 10.1175/ 1520-0469(1986)043⟨0784:CAOSMS⟩2.0.CO;2.

A. A. Lacis and V. Oinas. A description of the correlated k distribution method for modeling nongray gaseous absorption, thermal emission, and multiple scattering in vertically inhomogeneous atmospheres. *J. Geophys. Res.*, 96:9027–9063, 1991. doi: 10.1029/90JD01945.

W. Malkmus. Random Lorentz band model with exponential-tailed S^{-1} line-intensity distribution function. *J. Opt. Soc. Am.*, 57:323–329, 1967. doi: 10. 1364/JOSA.57.000323.

J. Manners, J.-C. Thelen, J. Petch, P. Hill, and J. M. Edwards. Two fast radiative transfer methods to improve the temporal sampling of clouds in numerical weather prediction and climate models. *Q. J. R. Meteorol. Soc.*, 135:457–468, 2009. doi: 10.1002/qj.385.

J. Mašek, J.-F. Geleyn, R. Brožková, O. Giot, H. O. Achom, and P. Kuma. Single interval shortwave radiation scheme with parameterized optical saturation and spectral overlaps. *Q. J. R. Meteorol. Soc.*, 142:304–326, 2016. doi: 10.1002/qj. 2653.

P. Mauno, G. M. McFarquhar, P. Räisänen, M. Kahnert, M. S. Timlin, and T. Nousiainen. The influence of observed cirrus microphysical properties on shortwave radiation: A case study over Oklahoma. *J. Geophys. Res.*, 116:17 pp, 2011. doi: 10.1029/2011JD016058.

B. H. J. McKellar and M. A. Box. The scaling group of the radiative transfer equation. *J. Atmos. Sci.*, 38:1063–1068, 1981. doi: 10.1175/1520-0469(1981) 038⟨1063:TSGOTR⟩2.0.CO;2.

W. E. Meador and W. R. Weaver. Two-stream approximations to radiative transfer in planetary atmospheres: A unified description of existing methods and a new imporovement. *J. Atmos. Sci.*, 37:630–643, 1980. doi: 10.1175/1520-0469(1980)037⟨0630:TSATRT⟩2.0.CO;2.

M. I. Mishchenko, L. D. Travis, and A. A. Lacis. *Scattering, Absorption, and Emission of Light by Small Particles.* Cambridge University Press: Cambridge, UK, 2002. 466 pp, electronic release available at http://www.giss.nasa.gov/ cr-mim/books.html.

E. J. Mlawer, V. H. Payne, J.-L. Moncet, J. S. Delamere, M. J. Alvarado, and D. C. Tobin. Development and recent evaluation of the MT_CKD model of continuum absorption. *Phil. Trans. Roy. Soc. A*, 370:2520–2556, 2012. doi: 10.1098:rsta.2011.0295.

L. Oreopoulos, E. Mlawer, J. Delamere, T. Shippert, J. Cole, B. Fomin, M. Iacono, Z. Jin, J. Li, J. Manners, P. Räisänen, F. Rose, Y. Zhang, M. J. Wilson, and W. B. Rossow. The continual intercomparison of radiation codes: Results from phase I. *J. Geophys. Res.*, 117:19 pp, 2012. doi: 10.1029/2011JD016821.

D. T. Pawlak, E. E. Clothiaux, M. F. Modest, and J. N. S. Cole. Full-spectrum correlated-k distribution for shortwave atmospheric radiative transfer. *J. Atmos. Sci.*, 61:2588–2601, 2004. doi: 10.1175/JAS3285.1.

G. N. Plass. Models for spectral band absorption. *J. Opt. Soc. Am.*, 48:690–703, 1958. doi: 10.1364/JOSA.48.000690.

I. V. Ptashnik, R. A. McPheat, K. P. Shine, K. M. Smith, and R. G. Williams. Water vapor self-continuum absorption in near-infrared windows derived from laboratory measurements. *J. Geophys. Res.*, 116:16 pp, 2011a. doi: 10.1029/ 2011JD015603.

I. V. Ptashnik, K. P. Shine, and A. A. Vigasin. Water vapour self-continuum and water dimers: 1. Analysis of recent work. *J. Quant. Spectrosc. Radiat. Transfer*, 112:1286–1303, 2011b. doi: 10.1016/j.jqsrt.2011.01.012.

I. V. Ptashnik, R. A. McPheat, K. P. Shine, K. M. Smith, and R. G. Williams. Water vapor foreign-continuum absorption in near-infrared windows from laboratory measurements. *Phil. Trans. R. Soc. A*, 370:2557–2577, 2012. doi: 10.1098/rsta.2011.0218.

V. Ramanathan and P. Downey. A nonisothermal emissivity and absorptivity formulation for water vapor. *J. Geophys. Res.*, 91:8649–8666, 1986. doi: 10.1029/JD091iD08p08649.

B. Ritter and J.-F. Geleyn. A comprehensive radiation scheme for numerical weather prediction models with potential applications in climate simulations. *Mon. Weather Rev.*, 120:303–325, 1992. doi: 10.1175/1520-0493(1992)120⟨0303:ACRSFN⟩2.0.CO;2.

B. Rockel, E. Raschke, and B. Weyres. A parameterization of broad band radiative transfer properties of water, ice, and mixed clouds. *Contrib. Atmos. Phys.*, 64:1–12, 1991.

A. Schomburg, V. Venema, F. Ament, and C. Simmer. Application of an adaptive radiative transfer scheme in a mesoscale numerical weather prediction model. *Q. J. R. Meteorol. Soc.*, 138:91–102, 2012. doi: 10.1002/qj.890.

K. P. Shine, I. V. Ptashnik, and G. Rädel. The water vapour continuum: Brief history and recent developments. *Surv. Geophys.*, 33:535–555, 2012. doi: 10.1007/s10712-011-9170-y.

K. P. Shine, I. V. Ptashnik, and G. Rädel. The water vapour continuum in near-infrared windows – Current understanding and prospects for its inclusion in spectroscopic databases. *J. Mol. Spectrosc.*, 327:193–208, 2016. doi: 10.1016/j.jms.2016.04.011.

A. Slingo. A GCM parameterization for the shortwave radiative properties of water clouds. *J. Atmos. Sci.*, 46:1419–1427, 1989. doi: 10.1175/1520-0469(1989)046⟨1419:AGPFTS⟩2.0.CO;2.

K. Stamnes and R. A. Swanson. A new look at the discrete ordinate method for radiative transfer calculations in anisotropically scattering atmospheres. *J. Atmos. Sci.*, 38:387–399, 1981. doi: 10.1175/1520-0469(1981)038⟨0387:ANLATD⟩2.0.CO;2.

K. Stamnes, S.-C. Tsay, W. Wiscombe, and K. Jayaweera. Numerically stable algorithm for discrete-ordinate-method radiative transfer in multiple scattering and emitting layered media. *Appl. Opt.*, 27:2502–2509, 1988. doi: 10.1364/AO.27.002502.

G. L. Stephens. Radiation profiles in extended water clouds. I: Theory. *J. Atmos. Sci.*, 35:2111–2122, 1978a. doi: 10.1175/1520-0469(1978)035⟨2111:RPIEWC⟩2.0.CO;2.

G. L. Stephens. Radiation profiles in extended water clouds. II: Parameterization schemes. *J. Atmos. Sci.*, 35:2123–2132, 1978b. doi: 10.1175/1520-0469(1978)035⟨2123:RPIEWC⟩2.0.CO;2.

J. H. Van Vleck and V. F. Weisskopf. On the shape of collision-broadened lines. *Rev. Mod. Phys.*, 17:227–236, 1945. doi: 10.1103/RevModPhys.17.227.

J. W. Warner and R. G. Ellingson. A new narrowband radiation model for water vapor absorption. *J. Atmos. Sci.*, 57:1481–1496, 2000. doi: 10.1175/1520-0469(2000)057⟨1481:ANNRMF⟩2.0.CO;2.

W. J. Wiscombe. The delta-M method: Rapid yet accurate radiative flux calculations for strongly asymmetric phase functions. *J. Atmos. Sci.*, 34:1408–1422, 1977. doi: 10.1175/1520-0469(1977)034⟨1408:TDMRYA⟩2.0.CO;2.

P. Yang, H. Wei, H.-L. Huang, B. A. Baum, Y. X. Hu, G. W. Kattawar, M. I. Mishchenko, and Q. Fu. Scattering and absorption property database for nonspherical ice particles in the near-through far-infrared spectral region. *Appl. Opt.*, 44:5512–5523, 2005. doi: 10.1364/AO.44.005512.

W. G. Zdunkowski and G. J. Korb. Numerische Methoden zur Lösung der Strahlungsübertragungsgleichung. *Promet*, 15(2/3):26–39, 1985.

List of Figures

List of Tables

List of Abbreviations

ACRANEB	Actif Calcul de RAyonnement et NÉBulosité (radiative transfer scheme in model ALADIN)
ACRANEB2	ACRANEB version 2
ALADIN	Aire Limitée Adaptation dynamique Développement International (limited area NWP model, as well as consortium)
ALARO	ALadin to AROme (a set of multi-scale physical parameterizations, applicable across the so-called grey zone of moist deep convection)
AROME	Application of Research to Operations at MEsoscale (limited area model of Météo-France)
ARPEGE	Action de Recherche Petite Echelle Grande Echelle (global model of Météo-France)
BIAS	systematic error
CHMI	Czech HydroMeteorological Institute
CIRC	Continual Intercomparison of Radiation Codes
CTS	Cooling To Space
DNI	Direct Normal Irradiance
EBL	Exchange Between Layers
EWS	Exchange With Surface
FSCK	Full-Spectrum Correlated-k method
GCM	General Circulation Model
GHI	Global Horizontal Irradiance
ICRCCM	InterComparison of Radiation Codes in Climate Models
MT_CKD	Mlawer-Tobin-Clough-Kneizys-Davies (model of water vapour continuum)
NER	Net Exchanged Rate
NWP	Numerical Weather Prediction
SDEV	Standard DEViation
RMSE	Root-Mean-Square Error
RRTMG	Rapid Radiative Transfer Model, optimized for use in GCMs
TOA	Top Of the Atmosphere
WDCGG	World Data Centre for Greenhouse Gases

List of Symbols

Frequently used symbols are listed below. Other symbols (typically the fitting parameters) are used only in few places; they are explained directly in the text.

Terminological remark: In most cases, the term 'flux' denotes *flux density* or *irradiance* (in $\mathrm{W\,m^{-2}}$). Similarly, adjective 'spectral' is often omitted for brevity, being indicated only by subscript ν of referred quantities.

$\bar{X}$	angular *or* line average of X
$\langle X \rangle$	path average of X
X'	delta-scaled value of X
$a(T), b(p,T)$ ...	Malkmus coefficients
a_1	direct transmission
a_2	direct-diffuse transmission
a_3	direct-diffuse reflectivity (plane albedo)
a_4	diffuse transmission (global transmission)
a_5	diffuse reflectivity (spherical albedo)
a_g	gravity acceleration
a	absorptivity
$B_\nu(T)$	blackbody radiance (Planck function)
c_p	specific heat of air at constant pressure
c^abs	saturation factor $k^\mathrm{abs}/k_0^\mathrm{abs}$ for cloud absorption
c^scat	saturation factor $k^{\mathrm{scat}'}/k_0^{\mathrm{scat}'}$ for cloud scattering
c_ν^self	water vapour self continuum coefficient
c_ν^foreign	water vapour foreign continuum coefficient
$c_\nu^{e-\mathrm{type}}$	water vapour e-type continuum coefficient
d	mean line spacing
E_{kl}	net exchange between model layers k and l
e	partial pressure of water vapour
$F^\uparrow$	upward radiative flux (irradiance)
$F^\downarrow$	downward radiative flux (irradiance)
F	net radiative flux $F^\downarrow - F^\uparrow$
$F_\odot$	direct normal irradiance of incoming solar flux at the TOA
f	proportion of scattering via forward Dirac peak
g	asymmetry factor
$g(k)$	cumulative probability function of k-values
$I_\nu(\mathbf{n})$	spectral radiance in direction $\mathbf{n}$
$I_\nu(\mu)$	azimuthally integrated spectral radiance
k	value of mass absorption coefficient in k-distribution method
k_ν^abs	mass absorption coefficient
k_ν^cont	mass absorption coefficient of water vapour continuum
k_ν^scat	mass scattering coefficient
k_ν^ext	mass extinction coefficient $k_\nu^\mathrm{abs} + k_\nu^\mathrm{scat}$
L	number of atmospheric layers
$\mathbf{n}$	unit vector
n_l	cloud fraction at model layer l
$P(\cos\Theta)$	scattering phase function

$P(\mu, \mu')$ .... azimuthally averaged scattering phase function
p .... total pressure
q .... specific humidity *or* mixture composition
q_i .... specific mass of cloud ice
q_l .... specific mass of cloud liquid
$q_{l,l+1}$ .... fraction of gridbox where cloud layers l and $l+1$ overlap
R_d .... gas constant of dry air
R_v .... gas constant of water vapour
$\mathbf{r}$ .... radius vector
S .... direct solar flux across horizontal plane *or* line strength
T .... thermodynamic temperature
T_e .... thermodynamic temperature of emitting body
t .... time
U .... diffusivity factor
u .... absorber amount
w_ν .... spectral weights
z .... altitude

α .... bracketing weight *or* weight defining generalized cloud overlap
α_1 to α_4 .... coefficients of the delta-two-stream system
α_L .... Lorentzian line half-width
$\alpha_S(\mu_0)$ .... plane albedo of the Earth's surface
$\bar{\alpha}_S$ .... spherical albedo of the Earth's surface
β .... bracketing offset
$\beta(\mu_0)$ .... upscatter fraction for direct solar ray
$\bar{\beta}$ .... backscatter fraction
δ .... optical depth or thickness
δ'_0 .... unsaturated cloud optical depth (delta-scaled)
$\delta_0^{\mathrm{eff}'}$ .... effective unsaturated cloud optical depth (delta-scaled)
$\delta()$ .... Dirac delta function
$\delta(\mathbf{n}, \mathbf{n}')$ .... Dirac delta function on the sphere
ϵ_S .... emissivity of the Earth's surface
Θ .... scattering angle
θ .... zenith angle
θ_0 .... solar zenith angle
λ .... wavelength
μ .... cosine of zenith angle θ or of scattering angle Θ
μ_0 .... cosine of solar zenith angle θ_0
ν .... frequency
π .... Ludolf number
ϖ .... single scattering albedo $k^{\mathrm{scat}}/(k^{\mathrm{abs}} + k^{\mathrm{scat}})$
ρ .... density
ρ_i .... cloud ice water content
ρ_l .... cloud liquid water content
σ .... Stefan-Boltzmann constant
τ .... transmission
ϕ .... azimuth
Ω .... solid angle
ω .... angle with respect to normal

Attachments

A Underlying peer-reviewed articles

This thesis is complemented by two articles written by the author, giving a more complete view of the developed broadband radiation scheme. In the interest of concise writing, the thesis does not repeat all details elaborated in the articles, but refers to them whenever possible.

The articles are co-authored by colleagues taking part in the ACRANEB and ACRANEB2 developments. Being subject to copyright of the Royal Meteorological Society, articles are attached only to printed version of the thesis, while the publicly available electronic version contains only their abstracts:

ABSTRACT: Spectral integration is the most time consuming part of solar radiative transfer codes used in numerical weather prediction. Routinely used approaches usually incline to one of two extremes – expensive and very accurate correlated k-distribution method made affordable by doing radiative transfer calculations with reduced temporal and/or spatial resolution, or cheaper but less accurate broadband approach affordable at every grid-point and time-step. Both approaches have their pros and cons, but hybrid solutions do not seem very promising. The presented work improves accuracy of full spectrum broadband approach by parameterizing secondary saturation of gaseous absorption, optical saturation of Rayleigh scattering and of cloud absorption as well as non-random gas-cloud spectral overlap. In order to isolate the problem of spectral integration from other approximations, one builds a narrowband reference using the same delta-two stream framework as the broadband scheme. Using this reference reveals the surprising fact that saturation effect of cloud absorption for one single layer and for the whole solar spectrum can be parameterized in a rather compact way, with one simple formula for liquid clouds and one for ice clouds. One then introduces the concept of effective cloud optical depth, which extends the applicability of parameterized cloud optical saturation to multi-layer cases, accommodating also effects of gas-cloud spectral overlap in the near-infrared. A scheme with all the above parameterizations indeed pushes accuracy limits of broadband approach to the level where a single shortwave interval can be used. This opens the possibility to reduce costs by using selective intermittency, where slowly evolving gaseous transmissions are updated on the timescale of hours, while quickly varying cloud optical properties are recomputed at every model time-step. In a companion article it will be demonstrated that the above core strategy is applicable also to thermal radiative transfer, with perhaps even better cost effectiveness there.

ABSTRACT: The main obstacle to efficient calculation of longwave radiative transfer is the existence of multiple radiative sources, each with its own emission spectrum. The work presented here overcomes this problem by combining the full spectrum broadband approach with the net exchanged rate decomposition. The idea is worked out to suit the needs of numerical weather prediction, where the most costly contribution representing the sum of internal exchanges is interpolated between cheap minimum and maximum estimates, while exchange with the surface and dominant cooling to space contributions are calculated accurately. The broadband approach must address the additional problems related to spectral integration and many ideas developed previously for the solar spectrum are reused. Specific issues appear, the dependence of broadband gaseous transmissions on the temperature of the emitting body being the most important one. The thermal spectrum also brings some simplifications – aerosols, clouds and the Earth's surface can safely be treated as grey bodies. The optical saturation of gaseous absorption remains the main complication and non-random spectral overlaps between gases become much more significant than in the solar spectrum. The broadband character of the proposed scheme enables the use of an unreduced spatial resolution with an intermittent update of gaseous transmissions and interpolation weights, thus ensuring a full response of longwave radiation to rapidly varying cloudiness and temperature fields. This is in contrast to the mainstream strategy, where very accurate and expensive radiative transfer calculations are performed infrequently, often with reduced spatial resolution. The approach proposed here provides a much better balance between errors coming from the radiation scheme itself and from the intermittency strategy. The key achievement, ensuring a good scalability of the scheme, is a computational cost essentially linear in the number of layers, with straightforward inclusion of scattering as an additional bonus.